THE PLANETARY SCIENCE JOURNAL, 3:222 (36pp), 2022 September https://doi.org/10.3847/PSJ/ac8b72

Arecibo Planetary Radar Observations of Near-Earth Asteroids: 2017 December–2019 December

Anne K. Virkki[1,2], Sean E. Marshall[1], Flaviane C. F. Venditti[1], Luisa F. Zambrano-Marín[1], Dylan C. Hickson[1,3], Anna McGilvray[1], Patrick A. Taylor[4], Edgard G. Rivera-Valentín[4], Maxime Devogèle[1], Eframir Franco Díaz[1,13], Sriram S. Bhiravarasu[5,14], Betzaida Aponte Hernández[4], Carolina Rodriguez Sánchez-Vahamonde[5,15], Michael C. Nolan[6], Phil Perillat[7], Israel Cabrera[7], Elliot González[7], Daniel Padilla[7], Victor Negrón[7], Juan Marrero[7], Johbany Lebrón[7], Adrian Bagué[7], Francisco Jiménez[7], Andy López-Oquendo[8], Daniel Repp[9], Riley A. McGlasson[10], Brynn Presler-Marshall[11], Ellen S. Howell[6], Jean-Luc Margot[12], and Sanjana Prabhu Desai[12]

[1] Arecibo Observatory, University of Central Florida, HC-3 Box 53995, Arecibo, PR 00612, USA; anne.virkki@helsinki.fi
[2] University of Helsinki, Helsinki, FI-00014, Finland
[3] Center for Wave Phenomena, Colorado School of Mines, Golden, CO 80401, USA
[4] Lunar and Planetary Institute, Universities Space Research Association, Houston, TX 77058, USA
[5] Arecibo Observatory, Universities Space Research Association, HC-3 Box 53995, Arecibo, PR 00612, USA
[6] Lunar and Planetary Laboratory, University of Arizona, Tucson, AZ 85721, USA
[7] Arecibo Observatory, Yang Enterprises, Inc., Arecibo, PR 00612, USA
[8] Northern Arizona University, Flagstaff, AZ 86011, USA
[9] Western Washington University, Bellingham, WA 98225, USA
[10] Purdue University, West Lafayette, IN 47907, USA
[11] University of Central Florida, Orlando, FL 32816, USA
[12] Department of Earth, Planetary & Space Sciences, UCLA, Los Angeles, CA 90095, USA

Received 2021 August 6; revised 2022 August 10; accepted 2022 August 10; published 2022 September 22

Abstract

We successfully observed 191 near-Earth asteroids using the Arecibo Observatory's S-band planetary radar system from 2017 December through 2019 December. We present radar cross sections for 167 asteroids; circular-polarization ratios for 112 asteroids based on Doppler-echo-power spectra measurements; and radar albedos, constraints on size and spin periods, and surface-feature and shape evaluation for 37 selected asteroids using delay-Doppler radar images with a range resolution of 75 m or finer. Out of 33 asteroids with an estimated effective diameter of at least 200 m and sufficient image quality to give clues of the shape, at least 4 (∼12%) are binary asteroids, including 1 equal-mass binary asteroid, 2017 YE5, and at least 10 (∼30%) are contact-binary asteroids. For 5 out of 112 asteroids with reliable measurements in both circular polarizations, we measured circular-polarization ratios greater than 1.0, which could indicate that they are E-type asteroids, while the mean and the 1σ standard deviation were 0.37 ± 0.23. Further, we find a mean opposite-sense circular-polarization radar albedo of 0.21 ± 0.11 for 41 asteroids (0.19 ± 0.06 for 11 S-complex asteroids). We identified two asteroids, 2011 WN15 and (505657) 2014 SR339, as possible metal-rich objects based on their unusually high radar albedos, and discuss possible evidence of water ice in 2017 YE5.

Unified Astronomy Thesaurus concepts: Near-Earth objects (1092); Radar telescopes (1330); Planetary science (1255); Remote sensing (2191); Asteroids (72)

Supporting material: machine-readable tables

1. Introduction

Earth-based planetary radar observations are a unique, cost-effective tool for postdiscovery characterization of near-Earth asteroids (NEAs). Optical observations enable the discovery of the majority of asteroids and track them across the plane of sky over days or weeks in order to refine their orbital elements. Such observations also constrain the rotation periods of NEAs with photometric monitoring of brightness variations via lightcurves. Planetary radar observations go beyond this by providing ultraprecise measurements of the line-of-sight range (distance) and velocity, as well as the target's rotation period based on high-resolution delay and Doppler-frequency measurements (Yeomans et al. 1987; Ostro et al. 1991; Ostro 1993). Although adaptive optics is continuously improving, delay-Doppler radar images have long been arguably the best Earth-based NEA imaging tool capable of directly detecting shape features down to meter-size scale and of detecting possible satellites (Margot et al. 2002). Radar echoes are also unique in revealing geologic features below the surface due to the penetration depth of several wavelengths (depending on the absorptive properties of the near-surface) or tens of centimeters at the S band (Campbell et al. 2010).

The Arecibo Observatory hosted the world's most powerful and sensitive planetary radar system until its collapse on 2020 December 1. The system had up to 1 MW of transmitted power at the *S* band (2380 MHz, 12.6 cm) and a 305 m antenna. Up to 124 NEAs per year were observed using the Arecibo planetary

[13] Currently at Leibniz-Institute of Atmospheric Physics, Kühlungsborn, D-18225, Germany.
[14] Currently at Space Applications Centre (ISRO), Jodhpur Tekra, Ahmedabad 380015, India.
[15] Currently at Malin Space Science Systems, San Diego, CA 92121, USA.

radar system. The antenna gain decreased by ∼30% at S-band wavelengths due to Hurricane Maria, which crossed Puerto Rico on 2017 September 20 and distorted the shape of the primary reflector. Additionally, the site generators suffered long-lasting problems due to overuse during the three-month power outage after the hurricane. During the time period covered in this paper, from 2017 December through 2019 December, the S-band radar system was functioning with only one klystron (rather than the optimal two) in a transmitter coupled with two to three generators, allowing at maximum 450 kW of transmit power.

Despite many technical challenges during this time period, we conducted more asteroid radar observations in 2019 than in any previous year. Here, we present data products from radar observations conducted from 2017 December through 2019 December, including radar cross sections, radar albedos, circular-polarization ratios (SC/OC ratios), multiplicity and shape features (e.g., detections of satellites or contact-binary "necks"), and estimates of spin rate and size derived from the observed Doppler-echo-power spectra and delay-Doppler images. We measured Doppler spectra for 191 individual NEAs, of which 167 had a Doppler bandwidth at least four times the finest frequency resolution and an integrated signal-to-noise ratio (S/N) greater than five noise standard deviations. Additionally, we obtained high-resolution delay-Doppler radar images (range resolution of 75 m or finer) of 75 NEAs, from which we selected 37 objects for further analysis in this paper based on the quality of the imaging data. While the goal of this paper is to provide a brushstroke analysis of a large number of NEAs, we emphasize that several of the presented asteroids have sufficient data for more detailed follow-up publications.

Section 2 details the observational and analytical methods and lists the studied targets. Section 3 presents and discusses the derived radar parameters, along with other data products derivable from the Doppler-echo-power spectra. Section 4 presents detailed information on the 37 imaged NEAs.

2. Dual-polarization Radar Observations

Most observing experiments began by transmitting an unmodulated continuous wave (CW) to obtain Doppler-echo-power spectra. The reported radar observations were obtained in dual-polarization mode, where we transmitted a circularly polarized wave and received the echo simultaneously in the opposite-circular (OC) polarization and the same-circular (SC) polarization as transmitted. While the echo in the OC polarization is usually stronger due to quasi-specular reflections, measuring the signal power in each polarization can constrain near-surface properties because the echo power in the SC polarization generally arises from scattering by wavelength-scale structures on the surface or in the near-surface (e.g., Virkki & Muinonen 2016).

The echoes were recorded as complex voltages that were processed into absolute values of echo power within a specified frequency bandwidth. The processed measurements are typically displayed as the *z*-scores of the echo power per frequency bin (so that the average of the off-echo power is zero and the standard deviation is one) vignetted close to the expected Doppler frequency based on the ephemeris. Although the existing literature on planetary radar studies has traditionally used "standard deviation" to describe this method of scaling, the term *z*-score, or standard score, is more widely used in statistics. A Doppler-frequency offset (Δf) of the center of the radar echo from the expected Doppler frequency indicates a faster or slower radial velocity than expected based on the ephemeris, i.e., $\Delta f \approx 2v_r/\lambda$, where v_r is the assumed radial velocity of the target with respect to the observer and λ is the wavelength of the transmitted signal (here, 12.6 cm).

Here we considered a successful observation ("detection") as one with the integrated S/N more than five standard deviations above the noise. When the echo power was high enough, we conducted delay-Doppler ranging and imaging measurements. For delay-Doppler observations, a phase-modulated waveform was transmitted to resolve the target in range along the line of sight. We used binary phase code modulation with pseudorandom sequences, where the phase can take a value of 0° or 180°. The range resolution depends on the baud, which is the minimum time interval between phase changes. Coarse bauds of 4 μs (about 600 m range resolution) were used to obtain astrometric range measurements, while bauds as fine as 0.05 μs (7.5 m range resolution) were used to obtain high-resolution radar images. For more in-depth information on radar waveforms and signal processing, see Ostro (1993), and for the radar image data-taking system technical details, see Margot (2021).

Table 1 lists all detected targets, their observation dates and types (CW or imaging with the baud specified), absolute magnitudes (as reported in the Jet Propulsion Laboratory's Small-Body Database[16] in 2021 December), whether the object is a potentially hazardous asteroid (PHA) or known to be a binary asteroid, and the spectrophotometric taxonomy, if known. The binary nature of (66391) Moshup was originally reported in 2001 (Benner et al. 2001) and that of 2018 EB was revealed by Goldstone Solar System Radar observations (Brozovic et al. 2018), whereas 2016 AZ8 and 2017 YE5 were found to be binary asteroids by these Arecibo radar observations (Taylor et al. 2018; Virkki et al. 2019). We omit bistatic observations (radar echo received at the Green Bank Observatory) from this paper and only report monostatic observations. Radar astrometry was measured and reported for all objects in Table 1 and is available at https://ssd.jpl.nasa.gov/sb/radar.html. Radar astrometry has helped not only in providing precise range and radial-velocity information for hundreds of NEAs over the past decade but also to quantify the Yarkovsky drift for tens of NEAs (Greenberg et al. 2020; Giorgini et al. 2020).

The next Earth-close-approach years are mentioned for some NEAs in Section 4, but for a large fraction of the included NEAs, the presented radar observations were their first and no other close approaches will take place in the next few decades. This makes some of the observations presented here unique. Moreover, radar observations of some of the NEAs that have a close approach in the next few years—then not until several decades later—will have more limited radar observation opportunities due to lower transmission power, antenna size, and scheduling constraints of the existing radar facilities.

3. Echo-power Spectra

We present the CW measurement results and observing circumstances in Table 2 (in Appendix C). For the measurement results, we list the observed limb-to-limb Doppler bandwidth, the radar cross section in both circular polarizations and their uncertainties and noise-statistics-based total S/N, and the SC/OC ratio and its uncertainty. The images of the Doppler-echo-power spectra, such as those displayed in

[16] https://ssd.jpl.nasa.gov/tools/sbdb_lookup.html

Table 1
Summary of the Successfully Observed NEAs

Asteroid Number	Name or Designation	Observation Dates (UT)	Observation Types	Absolute Magnitude	PHA or Binary	Taxonomic Type
433	Eros	2019 Jan 26–31, Feb 8–16	CW, 4 μs, 8 μs	11.2		S[1]
1627	Ivar	2018 Jul 3–16	CW, 4 μs	13.2		S[1]
1981	Midas	2018 Mar 21–25	CW, 0.5 μs, 0.2 μs	15.2	P	V[1]
2061	Anza	2018 Aug 15–20	CW, 4 μs	16.6		Sq[2]
2100	Ra-Shalom	2019 Sep 6–9	CW, 4 μs, 1 μs, 0.5 μs	16.2		B[1],K[7]
3200	Phaethon	2017 Dec 15–18	CW, 4 μs, 2 μs, 1 μs, 0.5 μs	14.6	P	B[1]
3752	Camillo	2018 Feb 20–22	CW, 4 μs, 0.5 μs, 0.2 μs	15.3		Ld[1]
10145	1994 CK1	2019 Jul 17	CW, 4 μs, 0.5 μs	16.8		Q[1]
11500	Tomaiyowit	2019 Jun 21	CW, 4 μs	18.3	P	S[1]
12538	1998 OH	2019 May 14	CW	15.8	P	Sq[1]
13553	Masaakikoyama	2018 Jul 11, Aug 8–15	CW, 0.5 μs, 0.2 μs	16.4		U[1]
66146	1998 TU3	2019 Aug 5	CW, 4 μs	14.5		Q[1]
66391	Moshup	2018 May 25–Jun 1	CW, 0.5 μs, 0.2 μs	16.5	P, B	Q[3]
66391	Moshup	2019 May 29–Jun 4	CW, 4 μs, 0.5 μs, 0.3 μs, 0.2 μs	16.5	P, B	Q[3]
68347	2001 KB67	2018 May 25–Jun 1	CW, 4 μs, 0.5 μs, 0.05 μs	19.9	P	
68950	2002 QF15	2019 May 20–26, Jun 5	CW, 4 μs, 0.2 μs, 0.05 μs	16.4	P	S[1]
85236	1993 KH	2019 Nov 13	CW, 4 μs	18.6	P	Sq, Q[1]
88254	2001 FM129	2019 Mar 20	CW, 4 μs, 0.5 μs	17.9	P	Q[1]
90403	2003 YE45	2019 Jun 26–28, Jul 8–9	CW, 4 μs, 0.5 μs	17.6	P	Sq[1]
96590	1998 XB	2018 Jan 2	CW, 4 μs	16.2		Q[1]
96590	1998 XB	2018 Mar 29	CW, 4 μs	16.2		Q[1]
141593	2002 HK12	2019 Aug 10–17	CW, 4 μs, 0.2 μs	18.2	P	C, X[1]
144332	2004 DV24	2018 Sep 13–15	CW, 0.2 μs	16.5	P	
152931	2000 EA107	2019 May 4	CW, 4 μs	16.1		Q[1]
153814	2001 WN5	2019 Aug 21–25	CW, 4 μs, 0.5 μs	18.2	P	L[1]
162082	1998 HL1	2019 Oct 25–28	CW, 4 μs, 0.1 μs	19.1	P	
163899	2003 SD220	2018 Aug 25	CW	17.9	P	S, Sr[1]
216258	2006 WH1	2019 Dec 13–14	CW, 4 μs, 0.2 μs	20.2	P	
237805	2002 CF26	2019 Sep 6–7	CW, 4 μs, 0.5 μs	17.4		S[4]
264357	2000 AZ93	2019 Dec 17	CW, 4 μs, 0.05 μs	21.1	P	S[1]
306383	1993 VD	2018 Jan 23	CW	21.5	P	
311554	2006 BQ147	2018 Feb 21	CW	18.7		Q[4]
354030	2001 RB18	2019 Sep 27–28	CW, 4 μs, 0.5 μs, 0.2 μs	18.5		C[1]
398188	Agni	2018 Jul 23–26, Aug 3	CW, 0.2 μs	19.4	P	Sq[3]
418849	2008 WM64	2017 Dec 21–23	CW, 0.5 μs, 0.2 μs	20.6	P	Sa[5]
418849	2008 WM64	2018 Dec 23	CW, 0.2 μs	20.6	P	Sa[5]
418849	2008 WM64	2019 Dec 28	CW, 4 μs, 0.5 μs	20.6	P	Sa[5]
418900	2009 BE2	2019 Jun 23	CW, 4 μs	19.2		
420591	2012 HF31	2018 Aug 9–13	CW, 4 μs	19.3		
438017	2003 YO3	2018 Jan 9	CW, 4 μs, 0.5 μs	18.6		
439313	2012 VE82	2018 Jul 17	CW	19.5		
441987	2010 NY65	2018 Jun 19	CW, 1 μs, 0.2 μs	21.5	P	Sv[5]
441987	2010 NY65	2019 Jun 19	CW, 0.1 μs	21.5	P	Sv[5]
454094	2013 BZ45	2019 Aug 2–5	CW, 4 μs, 0.2 μs	21.9	P	
455176	1999 VF22	2019 Feb 19–21	CW, 4 μs, 0.2 μs	20.6	P	
465617	2009 EK1	2019 Sep 12	CW, 4 μs	21.4	P	
467309	1996 AW1	2018 Jun 17	CW, 4μs	19.9	P	
469737	2005 NW44	2018 Jun 21	CW, 4 μs, 0.5 μs	20.4		Xe[5]
481394	2006 SF6	2019 Nov 11–15	CW, 4 μs, 0.2 μs	19.9	P	S[4]
494999	2010 JU39	2019 Jun 27–28	CW, 4 μs, 0.2 μs, 0.05 μs	19.6	P	
505657	2014 SR339	2018 Feb 8–9	CW, 0.5 μs, 0.2 μs	18.5	P	B[4]
509352	2007 AG	2017 Dec 12–30	CW, 4 μs, 0.5 μs, 0.2 μs	20.1	P	
509935	2009 QL8	2017 Dec 29	CW, 4 μs	19.4	P	
522684	2016 JP	2019 Apr 16–22	CW, 0.5 μs, 0.2 μs	21.1	P	
523788	2015 FP118	2018 Aug 24–26, Sep 12–14	CW, 4 μs, 0.5 μs, 0.2 μs	19.4	P	Sq[4]
523934	1998 FF14	2019 Sep 23	CW, 4 μs, 1 μs	20.7	P	
524594	2003 NW1	2018 Dec 12–14	CW, 4 μs, 0.2 μs	18.7	P	
525364	2005 CL7	2019 Aug 9–10	CW, 4 μs, 0.5 μs	19.6		
525477	2005 FC3	2019 Mar 16	CW, 4 μs	19.3		Q[4]
528159	2008 HS3	2019 May 15–17	CW, 4 μs, 0.1 μs	21.7	P	Q[1]
531277	2012 MM11	2018 Dec 5	CW	20.3	P	
533541	2014 JU54	2018 Dec 18	CW, 4 μs	19.9		

Table 1
(Continued)

Asteroid Number	Name or Designation	Observation Dates (UT)	Observation Types	Absolute Magnitude	PHA or Binary	Taxonomic Type
537342	2015 KN120	2019 Sep 27	CW	20.4		
	1998 SD9	2018 Aug 29–30	CW, 4 μs, 0.5 μs, 0.2 μs	24.0		
	1999 FN19	2018 May 29	CW	22.5		Sq[1]
	2005 WD	2019 Nov 11	CW, 4 μs	21.9	P	
	2006 WE4	2018 Jan 19–23	CW, 4 μs, 0.5 μs	18.9		
	2009 FU23	2019 May 10–11	CW, 4 μs, 0.5 μs	20.1	P	
	2010 GT7	2018 Dec 20–21	CW, 4 μs, 0.2 μs	20.2	P	
	2010 JG	2019 Nov 11–12	CW, 4 μs, 0.2 μs	20.9	P	
	2011 HP	2019 May 29–30	CW, 4 μs, 0.05 μs	21.8		B[4]
	2011 WN15	2019 Dec 12–13	CW, 4 μs, 0.2 μs	19.6	P	X[4]
	2011 YS62	2019 Nov 13–14	CW, 4 μs, 0.2 μs	19.7		
	2012 MS4	2018 Dec 20–21	CW, 4 μs, 0.5 μs, 0.2 μs	18.7	P	
	2013 CW32	2019 Feb 1	CW, 4 μs, 0.1 μs, 0.2 μs	22.0		S[4]
	2013 UG1	2018 Oct 16	CW	22.5		
	2014 WG365	2018 May 25–27	CW, 4 μs	20.0	P	
	2015 DP155	2018 Jun 9–12	CW, 0.05 μs	21.5	P	Q[4]
	2015 EG	2019 Mar 6–7	CW, 4 μs, 0.5 μs	25.6		
	2015 JD1	2019 Nov 1–4	CW, 4 μs, 1 μs, 0.2 μs, 0.05 μs	20.6	P	L[5]
	2015 QM3	2018 Aug 29	CW, 4 μs, 0.5 μs, 0.2 μs	20.4		
	2016 AZ8	2019 Jan 4	CW, 4 μs, 0.2 μs	21.1	P, B	C[4]
	2016 GW221	2018 Apr 9	CW	24.7		
	2016 OF	2019 Jul 10	CW, 4 μs	23.1		
	2016 PD1	2019 Aug 23	CW, 4 μs	23.7		
	2016 TH94	2019 Oct 25	CW, 4 μs, 0.2 μs	24.7		
	2017 QL33	2017 Dec 18–22	CW, 4 μs	21.2	P	
	2017 SL16	2019 Sep 23	CW	25.8		
	2017 VR12	2018 Mar 6–7	CW, 0.5 μs, 0.05 μs	20.6	P	V[6]
	2017 XT61	2018 Jan 3	CW	23.2		
	2017 YE5	2018 Jun 23–26	CW, 4 μs, 0.05 μs	19.2	P, B	
	2018 AJ	2018 Jan 22	CW, 4 μs, 0.5 μs, 0.05 μs	24.5		
	2018 BH3	2018 Jan 26	CW	25.4		
	2018 BM5	2018 Jan 26	CW, 4 μs, 0.5 μs	27.3		
	2018 BT1	2018 Jan 20	CW, 4 μs	22.9		
	2018 DH1	2018 Mar 23	CW	21.1	P	
	2018 DT	2018 Feb 26, Mar 7	CW	27.1		Q[6]
	2018 EB	2018 Oct 5–7	CW, 0.1 μs, 0.2 μs	21.8	P, B	
	2018 EJ4	2018 Jun 5	CW, 4 μs, 0.5 μs, 0.2 μs	21.4	P	C[4]
	2018 FB	2018 Mar 23	CW	24.1		
	2018 FH1	2018 Mar 23	CW, 4 μs	26.6		
	2018 LK	2018 Jun 11	CW, 4 μs	21.7	P	
	2018 LQ2	2018 Aug 21–22, Sep 7	CW, 4 μs	24.9		X, K[2,4]
	2018 MB7	2018 Jul 5	CW, 4 μs, 0.05μs	23.8		
	2018 MD7	2018 Aug 1	CW	22.7		
	2018 NB	2018 Jul 31–Aug 1	CW, 4 μs	19.3		Sq[4]
	2018 NE1	2018 Jul 21	CW, 4 μs	23.4		
	2018 NM	2018 Jul 20	CW	26.4		
	2018 NV	2018 Jul 12	CW	22.8		
	2018 PL10	2018 Aug 20	CW	22.1		
	2018 QU1	2018 Sep 7	CW, 4 μs	22.8		Q[4]
	2018 RB6	2018 Sep 13	CW	25.8		
	2018 RC4	2018 Sep 14	CW	25.9		
	2018 RQ2	2018 Sep 14	CW, 4 μs, 0.5 μs	23.0		
	2018 TG6	2018 Dec 10	CW	27.1		K[2]
	2018 TR4	2018 Oct 12	CW, 4 μs, 0.05 μs	25.0		
	2018 TZ2	2018 Oct 16	CW, 4 μs	24.7		
	2018 VX8	2019 May 11	CW, 4 μs, 0.05 μs	22.5		
	2018 XC4	2018 Dec 18	CW, 4 μs	26.2		
	2018 XG5	2019 May 2–8	CW, 4 μs	20.2	P	Sq[4]
	2018 XJ1	2018 Dec 18	CW, 4 μs	26.4		
	2018 XN	2019 Jan 14	CW, 4 μs	23.9		
	2018 XS4	2018 Dec 18	CW, 4 μs	25.2		
	2019 AK3	2019 Jan 10	CW	27.0		Sq[2]

Table 1
(Continued)

Asteroid Number	Name or Designation	Observation Dates (UT)	Observation Types	Absolute Magnitude	PHA or Binary	Taxonomic Type
	2019 AP11	2019 Jan 27–28	CW, 4 μs	25.2		
	2019 AR2	2019 Jan 10	CW	24.4		
	2019 AV2	2019 Jan 25–26	CW, 4 μs	21.1	P	
	2019 AW7	2019 Jan 10	CW, 4 μs	22.2		
	2019 AX5	2019 Jan 10	CW, 4 μs	26.0		
	2019 BG3	2019 Jan 28	CW, 4 μs	26.1		
	2019 BJ1	2019 Jan 29	CW, 4 μs	24.9		
	2019 CD5	2019 Mar 16–22	CW, 4 μs, 0.5 μs, 0.05 μs	22.0	P	Q[4]
	2019 CL2	2019 Mar 25	CW, 4 μs	23.3		
	2019 CN2	2019 Feb 9	CW	28.4		
	2019 CT1	2019 Feb 9	CW, 4 μs	21.9	P	
	2019 DN	2019 Mar 7–8	CW, 4 μs, 0.05 μs	22.4		Sq[4]
	2019 EN	2019 Apr 4	CW, 4 μs	21.2	P	
	2019 FN2	2019 Apr 21	CW, 4 μs, 0.05 μs	23.7		
	2019 FU	2019 Apr 8	CW, 4 μs, 0.5 μs, 0.05 μs	23.2		
	2019 GJ4	2019 Apr 9	CW, 4 μs	26.0		
	2019 GL4	2019 Apr 9–12	CW, 4 μs	23.1		
	2019 GM4	2019 Apr 19	CW, 4 μs	23.6		
	2019 GN4	2019 Apr 9–12	CW	24.7		
	2019 GO4	2019 Apr 12	CW, 4 μs	25.2		
	2019 GT1	2019 May 9	CW, 4 μs	24.9		
	2019 GT3	2019 Sep 5	CW, 4 μs, 0.5 μs	21.0	P	S[4]
	2019 JE	2019 May 8	CW	26.2		
	2019 JG1	2019 May 15	CW, 4 μs	26.6		
	2019 JJ3	2019 May 9	CW	27.5		
	2019 JL3	2019 May 17	CW	25.0		
	2019 JN2	2019 May 14	CW, 4 μs	25.7		
	2019 JU5	2019 May 16	CW, 4 μs	24.0		
	2019 KA4	2019 Jun 4	CW, 4 μs	26.0		
	2019 KD3	2019 Jul 14	CW	23.1		
	2019 KG2	2019 May 30	CW, 4 μs, 0.5 μs	25.9		
	2019 KV	2019 May 29	CW	26.2		
	2019 KZ3	2019 Jun 5	CW, 4 μs	24.2		
	2019 LU	2019 Jun 18	CW, 4 μs, 0.5 μs	25.1		
	2019 LV1	2019 Jun 26	CW, 4 μs	25.6		
	2019 MF1	2019 Jul 8–10	CW, 4 μs	21.8	P	
	2019 MT	2019 Jun 28–29	CW, 4 μs	24.7		
	2019 NE2	2019 Jul 9	CW, 4 μs	21.1	P	
	2019 NN3	2019 Jul 8	CW, 4 μs	24.7		
	2019 NX1	2019 Jul 8	CW	27.7		
	2019 OD	2019 Jul 25	CW	23.5		
	2019 OK	2019 Jul 25	CW, 4 μs	23.3		
	2019 PZ2	2019 Aug 17	CW, 4 μs, 0.5 μs	19.8		
	2019 QY1	2019 Nov 12	CW	20.8	P	
	2019 QZ3	2019 Sep 7	CW, 4 μs, 0.05 μs	24.7		
	2019 RA	2019 Sep 6	CW, 4 μs	25.5		
	2019 RC	2019 Sep 17	CW, 4 μs, 0.05 μs	21.8	P	
	2019 RX1	2019 Sep 9	CW, 4 μs	25.5		
	2019 SD8	2019 Oct 1	CW, 4 μs	27.3		
	2019 SE8	2019 Oct 1	CW	26.9		
	2019 SH3	2019 Sep 28	CW, 4 μs	25.6		
	2019 SL7	2019 Oct 10	CW, 4 μs, 0.05 μs	25.7		
	2019 SP	2019 Sep 28	CW, 4 μs	24.4		
	2019 SU3	2019 Sep 30	CW, 4 μs	27.2		Xe[2]
	2019 SW5	2019 Sep 28	CW, 4 μs	25.1		
	2019 SX3	2019 Oct 1	CW, 4μs	25.4		
	2019 TM	2019 Oct 8	CW, 4 μs	25.0		
	2019 UF5	2019 Oct 25	CW	25.6		
	2019 UG12	2019 Nov 1	CW	26.4		
	2019 UL8	2019 Nov 2	CW	26.3		
	2019 UN12	2019 Nov 11–12	CW	22.0		
	2019 UO	2019 Dec 26	CW, 4 μs, 0.5 μs	20.2	P	

Table 1
(Continued)

Asteroid Number	Name or Designation	Observation Dates (UT)	Observation Types	Absolute Magnitude	PHA or Binary	Taxonomic Type
	2019 UT7	2019 Oct 28	CW, 4 μs	26.8		
	2019 WO2	2019 Dec 7	CW, 4 μs	25.0		
	2019 WR3	2019 Dec 5–8	CW, 4 μs	22.9		
	2019 WT3	2019 Dec 8	CW, 4 μs	24.7		
	2019 XF	2019 Dec 17	CW	23.3		
	2019 XO3	2019 Dec 19	CW, 4 μs	26.0		
	2019 XQ3	2019 Dec 19	CW, 4 μs	20.7	P	
	2019 XR1	2019 Dec 8	CW, 4 μs	26.1		
	2019 XW	2019 Dec 8	CW, 4 μs	23.9		
	2019 YX1	2019 Dec 26	CW, 4 μs, 0.2 μs	24.4		

Note. Columns 1 and 2 show the asteroid number and name or provisional designation, column 3 lists the dates of the observations in UT, column 4 lists the types of radar observations conducted for each target with CW for continuous-wave Doppler-echo-power spectra and the baud length for delay-Doppler imaging, column 5 lists the absolute magnitude, column 6 lists whether the asteroid is a PHA (P) or a binary system (B), and column 7 lists the spectrophotometric taxonomy, if known.
References. [1]Binzel et al. (2019), [2]https://manos.lowell.edu/, [3]Popescu et al. (2019), [4]http://smass.mit.edu/catalog.php, [5]Perna et al. (2018), [6]Devogèle et al. (2019).

(This table is available in machine-readable form.)

Figure 1 (the top row), for 35 other NEAs for which we present further analysis in Section 4 are displayed in Appendix A, Figure 6. The echo-power spectrum images for all asteroids reported here are available through https://www.lpi.usra.edu/resources/asteroids/ and http://www.naic.edu/~pradar/, and the data will be available through the Small Bodies Node of the Planetary Data System.

The Doppler-echo-power spectra obtained by CW measurements provide a first-order gauge to the physical properties of the target by displaying echo-power z-scores per frequency bin. The observed limb-to-limb Doppler bandwidth (or Doppler broadening) arises from the target's limbs moving at opposite velocities relative to the target's center of mass projected along the line of sight. The Doppler bandwidth is a function of the transmitted wavelength, the target's projected diameter (D) at the time of observation, rotation period (P), and the subradar latitude (δ; degrees from the target's equator) at the time of observation:

$$B = \frac{4\pi D\cos(\delta)}{\lambda P}. \quad (1)$$

The subradar latitude is usually unknown for a single measurement. In these cases, we assume a close-to-spherical target illuminated at the spin equator, which constrains the upper limit of the period, because a target viewed closer to either pole can rotate with a shorter period and produce the same observed bandwidth.

The finest Doppler-frequency resolution ($f_{\rm res}$) depends on the scan receive duration ($t_{\rm scan}$): $f_{\rm res} = 1/t_{\rm scan}$. The scan time is limited by the light round-trip time (RTT) to the target and the time to switch from transmitting to receiving (typically 8 s, but often decreased to 6 s for targets with RTT less than 11 s): $t_{\rm scan} = {\rm RTT} - t_{\rm switch}$. RTT is approximately $(1000\,{\rm s}) \times d/(1\,{\rm au})$, where d is the distance of the target from the observer. For example, a target at a distance of 0.060 au would have an RTT of about 60 s.

The Doppler bandwidth is determined by eye from the integrated spectrum using "unsmoothed" cumulative echo power (standard deviations of thermal noise), as illustrated in Figure 1 (bottom panels). "Smoothing" refers to convolving frequency bins with a kernel (here, Gaussian) of a certain width, which improves the plot's clarity but can cause overestimation of the Doppler bandwidth. While the examples here show high-S/N targets, the determination of the bandwidth limits for low-S/N targets (z-score $\lessapprox 6$) can be as challenging visually as it is numerically. Also, for targets with a low-to-medium S/N and a wide Doppler bandwidth, the S/N is divided into more frequency bins, which can cause the limbs to blend into the noise and thus increase uncertainty in determining the limits. We estimate the bandwidth uncertainty at $4f_{\rm res}$ and omitted from Table 2 all targets with $B < 4f_{\rm res}$ because the Doppler bandwidth was not robustly resolved, which could impact the radar cross-section determination. NEAs that were detected but not well resolved in frequency are listed in Table 3 in Appendix C.

The S/N (for either polarization channel) is the ratio of the cross section to its statistical uncertainty (including thermal noise and self-noise but not systematic uncertainties), ideally,

$$S/N = \frac{\sum_{\rm signal} z_i}{\sqrt{B/f_{\rm res} + \left(\sum_{\rm signal} z_i^2\right)/(s^2 N_{\rm looks})}}, \quad (2)$$

where the sums are taken over the range of frequency bins with a signal. z_i is the z-score for bin i of the CW spectrum, $s = \pi/(4-\pi)$ comes from fading statistics of a radar signal (Ulaby et al. 1982), and $N_{\rm looks}$ is the number of looks (independent samples). The first term under the square root is from thermal noise (one standard deviation of noise from each frequency bin), and the second term is from self-noise. These two terms are added in quadrature to give the total statistical noise. Ideally, with many looks, the noise distribution is Gaussian.

z_i is effectively the S/N in a single frequency bin. It is related to the parameters of the system and the target by

$$z_i = \frac{\sigma_i P_{\rm tx} G_A^2 \lambda^2 \sqrt{N_{\rm looks}}}{(4\pi)^3 d^4 k_B T_{\rm sys} f_{\rm res}} \quad (3)$$

where σ_i is the reflectivity of the surface area that falls under each frequency bin (a partial radar cross section), $P_{\rm tx}$ is the transmitted power, G_A is the antenna gain (assuming the same

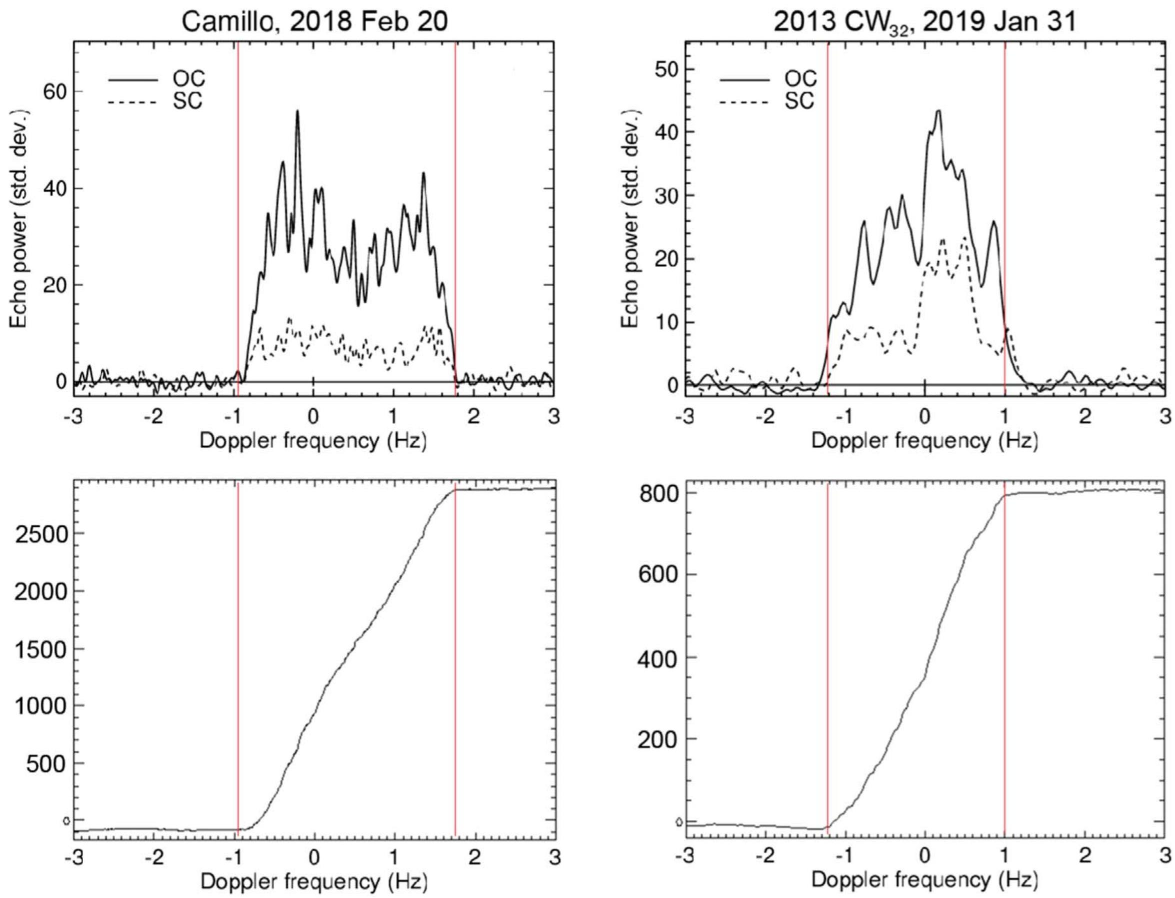

Figure 1. Example of Doppler-bandwidth determination from the Doppler-echo-power spectra for (3753) Camillo and 2013 CW32. The panels on the top show the echo-power standard deviations per frequency bin with "smoothing" (see the text for definition), and the panels on the bottom show the cumulative echo power (standard deviations, as a "function" of frequency) for the same asteroids without smoothing. All Doppler bandwidths were determined by eye using plots such as the panels on the bottom. The outlying "tails" in the Doppler spectrum in the top-right panel are likely due to smoothing. This illustrates why the bandwidths are determined using unsmoothed spectra.

telescope is being used for both transmission and reception) or, equivalently, $4\pi/\lambda^2$ times the effective aperture of the antenna, d is the target's distance from the observer, k_B is the Boltzmann constant, and $T_{\rm sys}$ is the receiver's system temperature (Ostro 1993). The radar cross sections, $\sigma_{\rm OC}$ and $\sigma_{\rm SC}$ listed in Table 2, were derived by integrating z_i through the selected Doppler bandwidth in a specific polarization (OC or SC) and solving for σ. The radar cross section is a measure of the target's total radar reflectivity: If the target were an ideal spherical reflector, the radar cross section would be equal to its projected area in the OC polarization and zero in the SC polarization.

These equations explain why radar observations are to some extent biased toward detecting slowly rotating asteroids more easily due to their narrower Doppler bandwidth. If the pointing to the target is not centered in the telescope beam due to large errors in the ephemeris or the telescope platform's incorrect height or tilt, the received echo power and, consequently, the S/N and the radar cross sections will get underestimated.

During the time of these observations, the antenna gain of the Arecibo main dish was about 71.8 dB at the S band, which corresponds to an effective aperture area of about 19,300 m^2 or 7 K Jy^{-1}, compared to $\sim$10 K Jy^{-1} before Hurricane Maria. The antenna gain G_A as a function of zenith angle and azimuth is shown in Appendix B, Figure 7. The average transmitted power per observation varied from 250 kW to 450 kW (except for 90 kW for 2019 YX1).

The uncertainty of the radar cross sections due to systematic errors is estimated to be 25%. This includes the uncertainty of the Doppler-bandwidth determination, antenna gain, fluctuations in $T_{\rm sys}$ and the transmitter power, and pointing issues (e.g., heat expansion of the platform support cables affecting the height of the platform and also the tilt caused by moving the Gregorian dome to large zenith angles can result in pointing errors and signal degradation). This is particularly relevant for comparing measurements from different years as opposed to measurements on consecutive days, for which some of these properties can vary and some can be assumed equal. In some cases, even one day's scan-to-scan radar cross sections can have fluctuations of 25% due to orientation-dependent variation in the projected area (e.g., elongation) or scattering properties (e.g., a heterogeneous surface).

In addition, because the radar cross section is the integrated echo power across the Doppler bandwidth measured from limb to limb as described above, the Doppler bandwidth's uncertainty can also play a role in the radar cross section's uncertainty. For high-S/N targets, the error from the bandwidth determination is negligible, whereas for low-S/N targets it could be significant and thus should be taken into account when interpreting the results.

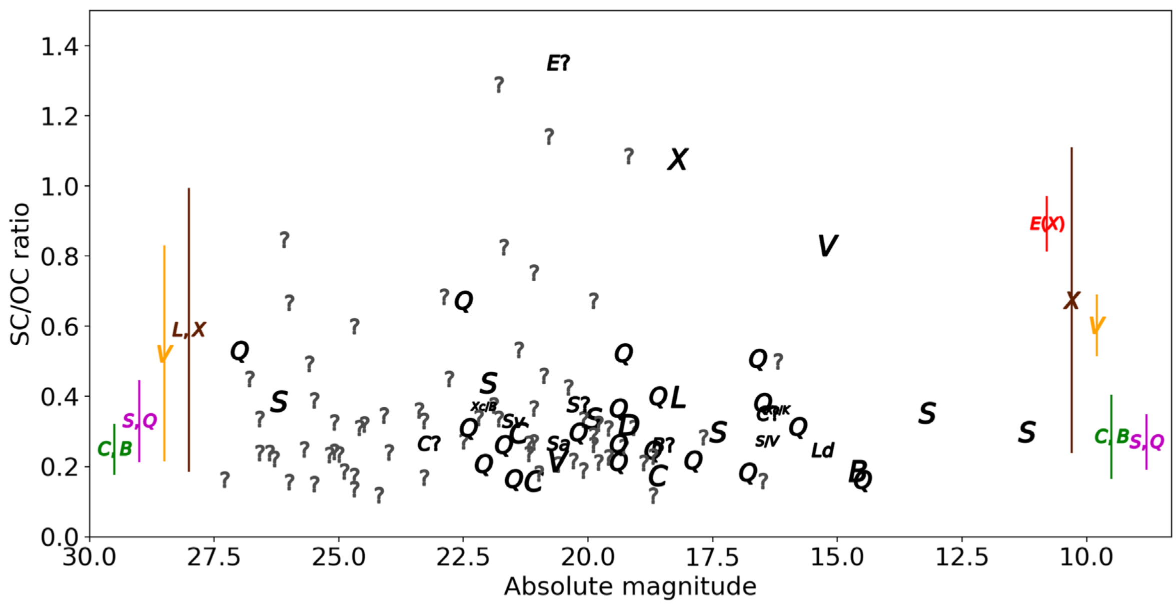

Figure 2. Average SC/OC ratios and absolute magnitudes of 112 NEAs with the taxonomic type indicated when known or a question mark when unknown or questionable. NEAs with unreliable SC polarization measurements ($S/N_{SC} \leqslant 3.0$) were omitted. The colored vertical bars on the left-hand side designate the means and 1σ standard deviations of the SC/OC ratios reported in this paper (Table 2), and the vertical bars on the right-hand side designate those reported in Benner et al. (2008) for the taxonomic types with at least five objects.

The receiver T_{sys} and signal power leakage due to cable faults can affect each polarization by a different amount. Optimally, the system temperature of the S-band radar system could be as low as 24 K; however, one receiver channel suffered from a gradually degrading low-noise amplifier (LNA) starting in April 2019, which we attempted to account for in the data processing, but it could have caused unexpected system temperature issues to specific observations (see Appendix B, Figure 7). The LNA was used for the OC polarization channel until 2019 November 27, after which it was changed to the SC polarization channel in order to improve the reliability of measurements in the OC polarization. The gradual failure could have caused undermeasured σ_{OC} of some observations in the weeks before the change. However, identifying which NEAs were affected and by how much could be done based on consistency with other observations, as will be described in more detail in Section 4 for specific NEAs, or in some cases the statistical probability of the observed SC/OC ratio. The SC polarization channel was deemed unreliable after the change, which affected all observations presented here that took place after 2019 November 27.

(433) Eros, (2100) Ra-Shalom, (66391) Moshup, and (68950) 2002 QF15 have previously published radar observations, which we can use for comparison to evaluate the consistency between the measurements from different years. For Eros, we measured a range of σ_{OC} from 25 km^2 to 49 km^2, which is consistent with the measurements of Jurgens & Goldstein (1976) (3.5 cm and 12.6 cm wavelengths at Goldstone) and Campbell et al. (1976) (70 cm wavelength at Arecibo). Magri et al. (2001) yielded $\sigma_{OC} = (75 \pm 20)$ km^2 (12.6 cm wavelength at Arecibo), which is greater than what we measured and covered several orientations; however, due to the axis ratio of 3 and a concave shape, the observation geometry could play some role in the discrepancy. All the SC/OC ratios were consistent. For Ra-Shalom, we measured radar cross sections from (0.75 ± 0.20) km^2 to (1.15 ± 0.30) km^2, whereas Shepard et al. (2008b) summarized Arecibo S-band observations yielding a consistent $\sigma_{OC} = (1.16 \pm 0.29)$ km^2 in 2000 and 29% larger (1.48 ± 0.37) km^2 in 2003. Systematic issues cannot be fully ruled out as the observations were conducted during the weeks before the OC polarization channel's LNA failure; however, the measurements are consistent within the uncertainty limits and the rotation phase plays a part as well for a slowly rotating asteroid ($P = (19.792 \pm 0.004)$ hr) with a lightcurve amplitude of 0.5 mag (Warner & Stephens 2020a). Other examples are discussed in Section 4.

The radar cross section in the SC polarization divided by that in the OC polarization gives the SC/OC ratio:

$$\mu_C = \frac{\sigma_{SC}}{\sigma_{OC}}. \tag{4}$$

The SC/OC ratio has less uncertainty than the radar cross sections because some of the systematic measurement errors affecting both polarization channels similarly cancel out in the division; thus, the SC/OC ratio is often known more precisely than the cross sections themselves. The unreliable SC radar cross sections and SC/OC ratios (the SC S/N less than 3.0) and those due to the LNA failure in 2019 November are marked with N/A in Table 2. Unusually high SC/OC ratios in 2019 November, before the LNA was changed from the OC to the SC channel, are included but should be considered with caution.

The observed SC/OC ratios of certain spectrophotometric complexes can have significantly different mean values and variance. For example, E-type asteroids consistently have an SC/OC ratio of order of unity, and V-type asteroids have mean values of SC/OC ratio between 0.5 and 0.8 (Benner et al. 2008; Howell et al. 2020; Aponte-Hernández et al. 2020). Other types, dominated by the S and C complexes, consistently have SC/OC ratios between 0.1 and 0.6 but are indistinguishable from each other.

Figure 2 illustrates the distribution of the observed SC/OC ratios listed in Table 2 versus the absolute magnitudes, using average values for the NEAs observed on multiple days and the taxonomic type as the marker (Sq type is denoted here as Q).

The mean values and standard deviations of the SC/OC ratios for the S + Q classes and C + B classes—both of which include at least five NEAs—are 0.32 ± 0.12 and 0.22 ± 0.05, respectively. Other types (V, X complex, and L/Ld) have at most three representative objects, and in some of those cases, the spectral classification is uncertain as we discuss in the next section, so although they are displayed in the image, the statistical significance is low. Our global mean and standard deviation for the 112 NEAs is 0.37 ± 0.23. The means for the S and Q classes individually are statistically equal, and all means are consistent with those reported by Benner et al. (2008). A more thorough analysis of these distributions and classifying objects that are not unambiguously identified spectroscopically requires further work that is beyond the scope of this paper.

The SC/OC ratio has traditionally been considered as a zeroth-order gauge of the surface and near-subsurface roughness of the target (Ostro 1993). For example, Nolan et al. (2013) predicted a relatively smooth surface for (101955) Bennu at centimeter-to-meter scales. However, the spacecraft imaging by OSIRIS-REx revealed a visibly rugged surface at this size scale (Lauretta et al. 2019). Based on numerical modeling (Virkki & Muinonen 2016; Virkki & Bhiravarasu 2019), the SC/OC ratio should not necessarily be interpreted as a linear measure of the surface roughness without further constraints. Virkki & Muinonen (2016) suggested that as the wavelength-scale roughness increases, both the SC and OC radar albedos increase in a nonlinear way that results in a ceiling value for the SC/OC ratio that depends on the electric properties of the near-surface. Consequently, specific taxonomic types can have different ceiling SC/OC ratio values even when the wavelength-scale surface roughness is comparable. Because the ceiling values can be different, the SC/OC ratio values between two different taxonomic types are not necessarily comparable in terms of surface roughness. Furthermore, a range of SC/OC ratios is often observed for single objects as will be detailed in Section 4. If measurement errors can be ruled out, the most likely physical properties to cause them are related to the surface roughness, i.e., heterogeneous particle size–frequency distributions and surface structures. Although there are indications that composition can play a role in the extent of the range of the SC/OC ratios, we refrain here from detailed interpretations that are pending better evidence of the extent of contribution by different factors.

4. Delay-Doppler Radar Imaging

In this section, we present in more detail the 37 NEAs for which we obtained high-S/N delay-Doppler images with more than five pixels in the delay dimension and more than three pixels in the Doppler dimension. While the scope of this paper is to provide a brushstroke analysis of a large number of NEAs, several of the NEAs discussed here have enough data for further analysis. Furthermore, unresolved echoes (i.e., all echo is contained in a single pixel at the finest available resolution) and images with a very low S/N have been omitted here. Thirty-six of the best delay-Doppler images of the 37 selected NEAs are displayed in Figures 3 and 4 with short descriptions of each object in the following subsections. The Doppler-echo-power spectra for these objects are displayed in Appendix A, Figure 6, excluding (3752) Camillo and 2013 CW32 that were used as examples in Figure 1. Moreover, radar analysis of (3200) Phaethon is available in Taylor et al. (2019a); a full radar analysis and a shape model of (1981) Midas are available in McGlasson et al. (2022), and a radar analysis of 2019 OK is available in Zambrano-Marin et al. (2022). Some observations were led by other teams, so a full radar analysis is in preparation, and those NEAs were therefore omitted from this section, including (433) Eros (e.g., Hinkle et al. 2019, 2022), (163899) 2003 SD220 (e.g., Rivera-Valentín et al. 2019), and 2018 EB (e.g., Brozovic et al. 2018).

Table 4 (in Appendix C) provides a summary of details on the 37 selected NEAs in terms of the system setup as well as results, including the apparent range resolution (in the vertical dimension) with the samples per baud (SPB; defines how many times each delay (range) bin was sampled) noted in parentheses, and the observed maximum visible range and frequency extents. While the (uncorrelated) range resolution is simply baud $\times\, c/2$ (where c is the speed of light), the apparent range resolution depends on the baud and the SPB so that

$$\text{App. range res.} = \frac{c}{2} \times \frac{\text{baud}}{\text{SPB}}. \quad (5)$$

Although sampling several times within a baud can make the range resolution finer and slightly improve the S/N by reducing noise, it causes noise correlation between adjacent rows, as described in detail by Magri et al. (2007). These correlations can appear as vertical artifacts in the images.

Similar to the Doppler-echo-power spectra, the images are processed to display in units of standard deviations above the noise baseline (i.e., linear z-scores). The displayed delay-Doppler images in Figures 3 and 4 have been enhanced in contrast such that z-scores <0 map to black while white represents values higher than the 95th percentile. The apparent S/N can be varied in the processing by varying the frequency resolution (up to the finest resolution): More frequency bins (finer frequency resolution) can reveal more features and topographic detail, whereas fewer frequency bins (coarser frequency resolution) can provide a better S/N per pixel. Similarly, the range dimension can be decimated in some cases by a factor of 2 or 4 to increase the S/N per pixel. We have not used the finest resolutions in all the panels in Figures 3 and 4 but looked for a visually pleasing appearance for each. The selected resolutions are listed in the image captions.

For simplicity, we define contact binaries as all objects for which we observed a possible bifurcated shape, i.e., two lobes of equal or unequal size with a narrower neck connecting them. All nonbifurcated spheroids (elongated or not) and top-shaped asteroids are referred to as rounded. Table 4 (Appendix C) can be used to evaluate which NEAs have enough radar data available for more detailed shape modeling. However, not every object in the list might be suitable for successful modeling because orientation coverage (which we evaluate here only for a few objects) and the availability of lightcurves also play a role.

In the presented images, the limb-to-limb breadth can be difficult to distinguish in some cases. Typically, we consider pixels with z-scores <3 as noise but evaluate also the z-scores of the pixels close to the trailing edge of the apparent echo to determine if they should be included in the visible range extent or not. In the ideal case of a noiseless radar image of a rounded diffusely scattering object, the visible extent in range is equal to the radius of the sphere and in frequency equal to the Doppler bandwidth as described in Section 3. In practice, the echo from the trailing edge of the illuminated hemisphere is often dominated by noise, which can cause the radius to be underestimated.

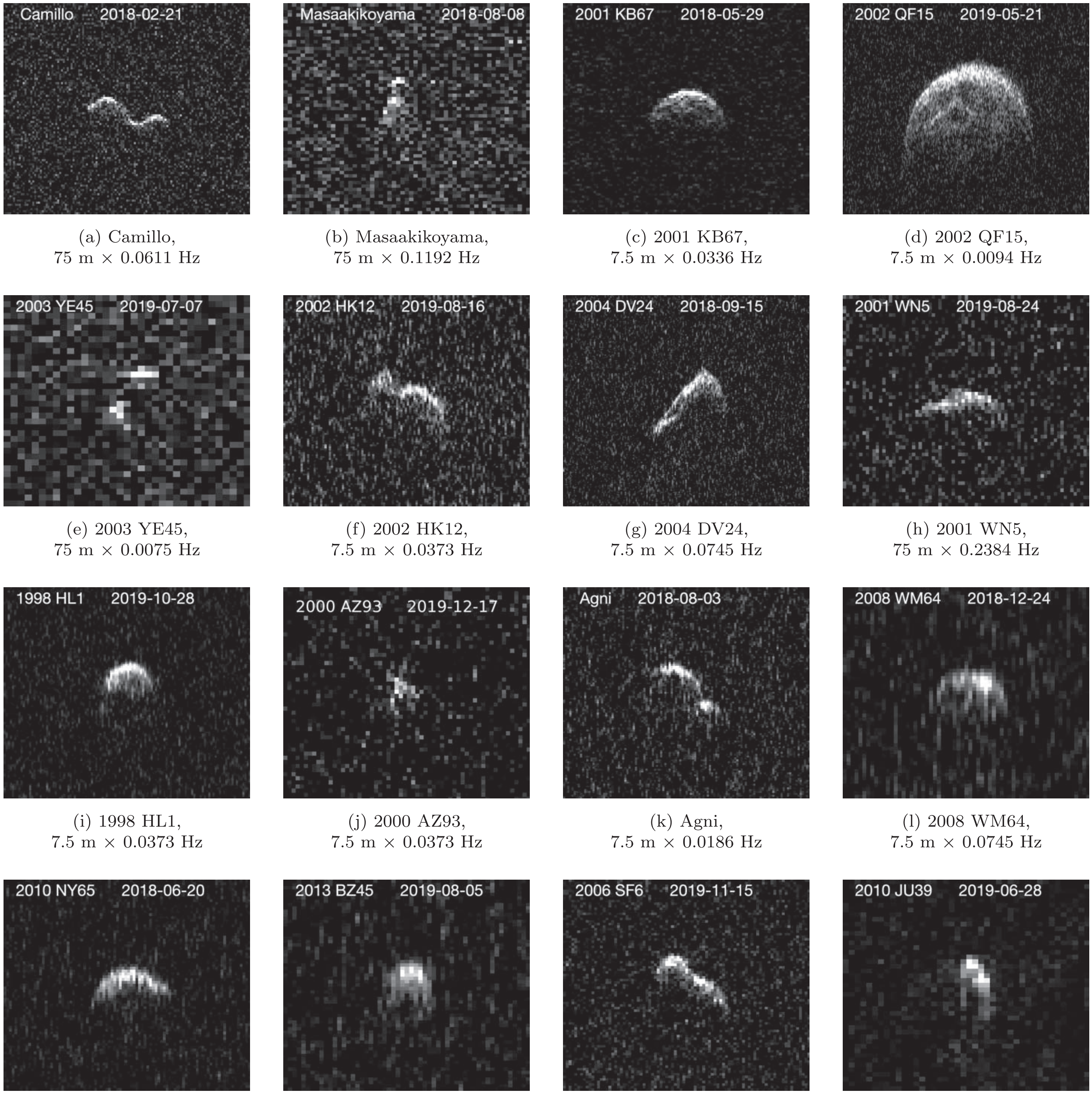

(a) Camillo, 75 m × 0.0611 Hz

(b) Masaakikoyama, 75 m × 0.1192 Hz

(c) 2001 KB67, 7.5 m × 0.0336 Hz

(d) 2002 QF15, 7.5 m × 0.0094 Hz

(e) 2003 YE45, 75 m × 0.0075 Hz

(f) 2002 HK12, 7.5 m × 0.0373 Hz

(g) 2004 DV24, 7.5 m × 0.0745 Hz

(h) 2001 WN5, 75 m × 0.2384 Hz

(i) 1998 HL1, 7.5 m × 0.0373 Hz

(j) 2000 AZ93, 7.5 m × 0.0373 Hz

(k) Agni, 7.5 m × 0.0186 Hz

(l) 2008 WM64, 7.5 m × 0.0745 Hz

(m) 2010 NY65, 7.5 m × 0.0373 Hz

(n) 2013 BZ45, 7.5 m × 0.0373 Hz

(o) 2006 SF6, 7.5 m × 0.0372 Hz

(p) 2010 JU39, 7.5 m × 0.0186 Hz

Figure 3. The delay-Doppler images with the vertical × horizontal resolution. The range (delay) increases from top to bottom, and the Doppler frequency increases from left to right, i.e., the right-hand side is approaching, while the left-hand side is receding. Pixel values are in units of standard deviations above the noise baseline (i.e., linear z-scores). The color map is clipped such that z-scores <0 map to black while white represents values higher than the 95th percentile. The images are available in FITS format through Figshare (Virkki et al. 2022).

For elongated targets and contact binaries, the visible range can be close to the full long-axis dimension depending on the target's orientation. Elongated asteroids can be recognized by an asymmetric echo; see for example the images of (505657) 2014 SR339 or 2017 VR12 in Figure 4, panels (a) and (p), respectively. We heavily utilize visual case-by-case estimation of which pixels should be included as echo and which ones as noise and how to extrapolate the full size from what is visible in the images. We urge caution from the reader in using these dimensions. A more precise but also much more time-consuming method would be shape modeling, which is not in the scope of this paper but is strongly recommended if more precision is required for a specific purpose.

Thermal modeling using, e.g., WISE observations (Mainzer et al. 2011) is another method for estimating diameters. In this paper, we prioritize size estimation using radar observations but

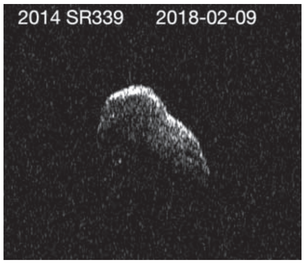

a) 2014 SR339,
7.5 m × 0.0373 Hz

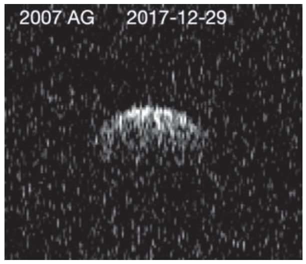

(b) 2007 AG,
7.5 m × 0.0741 Hz

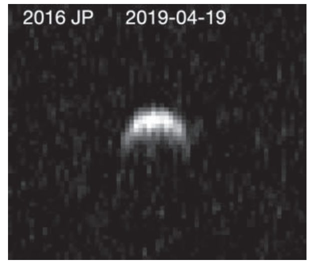

(c) 2016 JP,
7.5 m × 0.0745 Hz

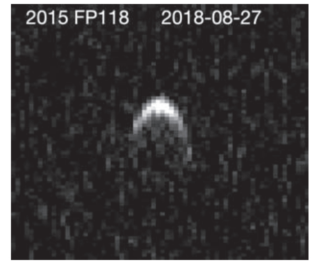

(d) 2015 FP118,
7.5 m × 0.1490 Hz

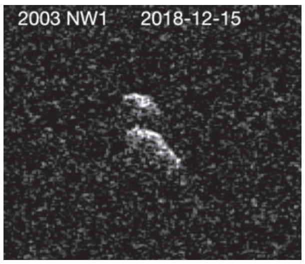

(e) 2003 NW1,
7.5 m × 0.0068 Hz

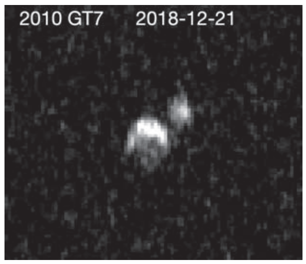

(f) 2010 GT7,
7.5 m × 0.0931 Hz

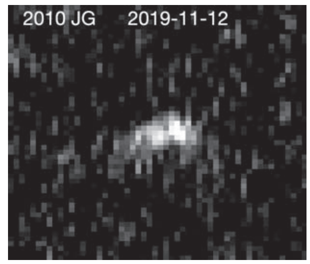

(g) 2010 JG,
7.5 m × 0.0745 Hz

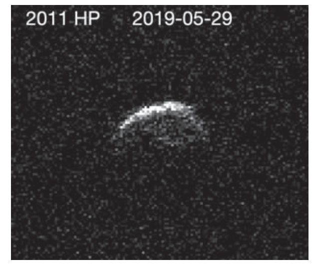

(h) 2011 HP,
7.5 m × 0.0373 Hz

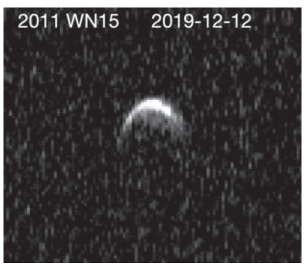

(i) 2011 WN15,
7.5 m × 0.1490 Hz

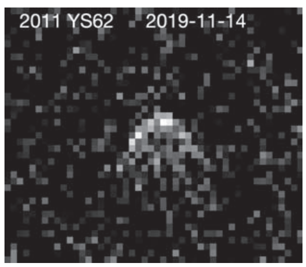

(j) 2011 YS62,
30 m × 0.0745 Hz

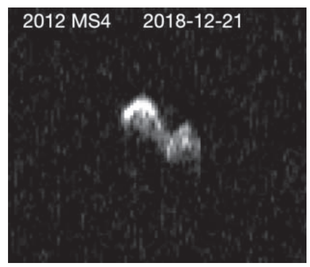

(k) 2012 MS4,
7.5 m × 0.0093 Hz

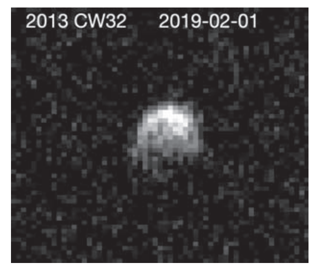

(l) 2013 CW32,
7.5 m × 0.1490 Hz

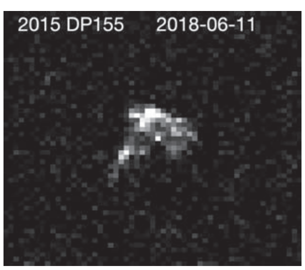

(m) 2015 DP155,
7.5 m × 0.0745 Hz

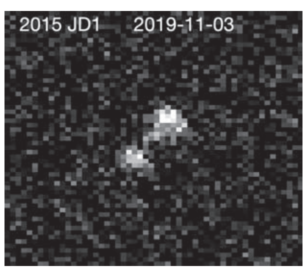

(n) 2015 JD1,
7.5 m × 0.0745 Hz

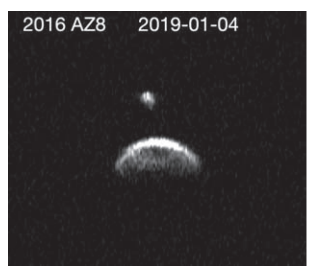

(o) 2016 AZ8,
7.5 m × 0.0373 Hz

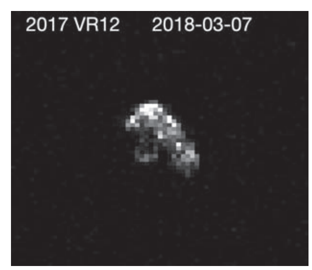

(p) 2017 VR12,
7.5 m × 0.2506 Hz

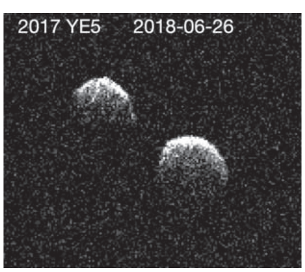

(q) 2017 YE5,
7.5 m × 0.0204 Hz

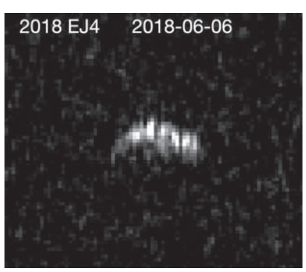

(r) 2018 EJ4,
7.5 m × 0.0373 Hz

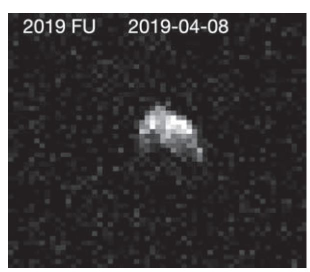

(s) 2019 FU,
7.5 m × 0.596 Hz

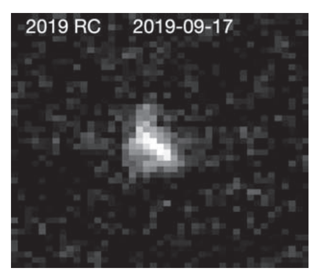

(t) 2019 RC,
7.5 m × 0.0186 Hz

Figure 4. As Figure 3.

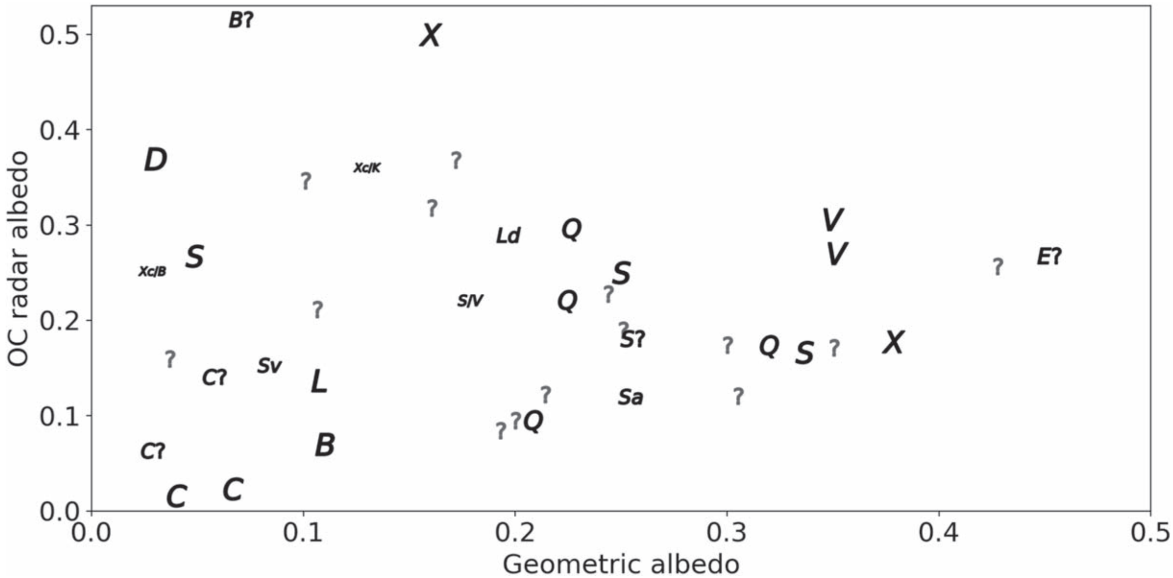

Figure 5. The distribution of OC radar albedos and optical geometric albedos of 41 NEAs: 37 as presented in Section 4 in addition to the radar and geometric albedos as published for (433) Eros (Magri et al. 2001), (1981) Midas (McGlasson et al. 2022), (2100) Ra-Shalom (Shepard et al. 2008b), and (3200) Phaethon (Taylor et al. 2019a). The taxonomic type is indicated when known or using a question mark when unknown or questionable. The mean OC radar albedos for S + Q- and C-type NEAs with 1σ standard deviations is 0.19 ± 0.06 (11 NEAs) and 0.06 ± 0.05 (4 NEAs), respectively, while the global average for 41 NEAs was 0.21 ± 0.11. The number of NEAs that are V types, X complex, or L/Ld types is too low to provide statistical significance. The relative uncertainty for the radar albedo of Midas is estimated at ~40% using a shape model (McGlasson et al. 2022); therefore, the radar albedos of the other less-constrained cases are estimated to be at least 50%.

compare the estimates to those obtained using thermal modeling (when available).

We constrained the radar albedo in the OC polarization for the imaged targets when possible. The target's radar albedo is a measure of the radar reflectivity per unit area:

$$\hat{\sigma}_{\rm OC} = \frac{\sigma_{\rm OC}}{A_{\rm proj}}, \tag{6}$$

where $A_{\rm proj}$ is the projected area of the target at the time of the observation. For contact-binary and binary asteroids, we estimate $A_{\rm proj}$ as the sum of the projected areas of the two components assuming they are spherical. Note that in most cases, obtaining a better estimate of the radar albedos—and especially its possible variation—will require shape modeling. The radar albedo depends on the near-surface electric permittivity of the target, which itself depends on the near-surface mineralogy, density, and the volume fraction of metals (Shepard et al. 2008c, 2015; Hickson et al. 2020). Using the S-band radar, all millimeter-scale and smaller vacuum inclusions can be considered as microporosity that decreases the effective electric permittivity of the material. In addition to the near-surface density, volume scattering in water ice is known to enhance the radar albedos in both polarizations, thus also enhancing the SC/OC ratios, as the radar observations of the icy Galilean moons (Ostro et al. 1992) and the permanently shadowed polar craters of Mercury (Harmon et al. 2001) have shown. Also, the size–frequency distribution and morphology of the wavelength-scale regolith could play a role as demonstrated by Virkki & Bhiravarasu (2019).

We estimated the geometric albedos using the following equation (Harris & Harris 1997):

$$p_V = 10^{[6.2472 - 2\log_{10}D - 0.4H]}, \tag{7}$$

based on the absolute magnitude (H) as listed in Table 1 and our diameter estimates. This allows us to analyze the geometric and radar albedos in parallel to the SC/OC ratios. For instance, X-type asteroids can be classified using the geometric albedo so that $p_V < 0.1$ for P-type asteroids or $0.1 < p_V < 0.3$ for M-type asteroids, and $p_V > 0.3$ for E-type asteroids (e.g., Clark et al. 2004; Thomas et al. 2011). We illustrate the $\hat{\sigma}_{\rm OC} - p_V$ distribution in Figure 5 and summarize the $\hat{\sigma}_{\rm OC}$ means and standard deviations in Section 5.

If lightcurve data were not available, rotation periods were constrained based on diameter estimates and the limb-to-limb bandwidth (using Equation (1) as described in Section 3) and feature tracking, when possible. If a feature is observed moving through the subradar point as the asteroid rotates, one can keep track of how fast the feature moves through the illuminated hemisphere, or how often the feature appears at the same point if the asteroid rotates more than once during the imaging track. If a bump on the surface of a rounded asteroid or a lobe of a contact binary at a distance d_r from the center of mass is observed to move at a radial velocity v_r, we can estimate the rotation period using the equation

$$P = \frac{2\pi d_r}{v_r \sin(\phi)}. \tag{8}$$

The projection angle ϕ is the angle between the line of sight and the line from the feature to the center of mass. Because the projection effects can cause challenges in estimating d_r and ϕ, this approach works the best when $\phi \approx 90°$ (i.e., the tracked feature is approximately at the same range as the center of mass).

Radar campaigns that last multiple days and cover a large range of sky motion are necessary for constraints on the spin-axis orientation. These assumptions require case-by-case analysis. We deliberately omit other more elaborate and precise ways to derive the physical properties of asteroids using radar observations and leave them to follow-up papers that comprehensively present further analysis on fewer targets and focus on more specific methods or properties. For example, we obtained delay-Doppler images in the SC polarization for all NEAs presented here, but we consider the analysis outside the scope of this paper.

4.1. (3752) Camillo (1985 PA)

The first radar images of Camillo obtained in 2018 February 20–22 (Figure 3, panel (a)) revealed a contact-binary structure with two lobes, each more than 1 km across, connected with a neck that is at least 300 m thick. Using the published rotation period of 37.846 hr (Pravec et al. 1998) and the observed Doppler-bandwidth range from 0.9 Hz to 2.7 Hz with Equation (1), we can constrain the long axis to at least 3.7 km and the intermediate axis to at least 1.2 km. This suggests an axis ratio of about 3, but with an unknown factor from the sky motion's and spin-axis orientation's effect on the subradar latitude. The lightcurve amplitude reported by Pravec et al. (1998) is 1.1 mag, which is consistent with an axis ratio of 2.8 or greater depending on the shape of the lobes. The rotation-phase progression in the images during the three days is consistent with the long rotation period. Assuming that the first observation on February 21 corresponds to a rotation phase of 0° and that Camillo was displaying its maximum bandwidth ($B = 2.7$ Hz), the second day's observations ~24 hr later would correspond to a rotation phase of 0.63 (228°, $B = 2.2$ Hz), and the last day's observations ~48 hr later would correspond to a phase difference of 0.25 (90°, $B = 0.9$ Hz) compared to the first. Although the sky motion of about 6°–7° per day causes a small change in the subradar latitude, the bandwidth variation and the delay-Doppler images are consistent with phase 0 being a maximum, 0.25 being a minimum, and 0.63 being in between the 0.5 maximum and 0.75 minimum. The CW observation on February 22 suffered a technical issue that tripled the observed bandwidth. However, the recorded echo power should not have been affected and the radar cross section of the day seems reasonable. Assuming two spherical lobes with a diameter of 1.8 km each, and using the maximum radar cross section of (1.55 ± 0.39) km^2, we estimate a radar albedo of 0.3 ± 0.1. The SC/OC ratio is consistently about 0.25 ± 0.02 through all three days. Camillo was found to be a rare Ld-type asteroid by spectrometry (Binzel et al. 2019). Although comparing the radar-scattering properties with other L/Ld-type asteroids is not statistically meaningful, our measurements suggest that the radar-scattering properties are most comparable to those of S-complex asteroids. The CW spectrum of Camillo was observed also on 2013 February 13–16; on February 13, the SC/OC ratio was only 0.13, possibly due to system temperature issues.[17] This radar apparition of Camillo at 0.142 au was its closest approach to Earth until 2055 at 0.09 au.

4.2. (13553) Masaakikoyama (1992 JE)

Masaakikoyama is a slow rotator with a rotation period from 38 to 97 hr and demonstrates signs of tumbling as reported in the literature (Pravec et al. 2005; Petrova et al. 2019; Warner & Stephens 2019; Gorshanov et al. 2020). Two days of radar imaging during its distant flyby of Earth at 0.200 au at a resolution of 75 m revealed an elongated object with ~825 m visible extent (Figure 3, panel (b)). These images hint at a contact-binary structure, most visibly in the images obtained on 2018 August 8. Using Equation (1), an effective diameter of at least 1 km would be consistent with the observed Doppler bandwidths of up to 0.8 Hz on August 8, assuming that the rotation period of 38 hr (Pravec et al. 2005) is correct. Similarly, an effective diameter of at least 1.67 km or 2.80 km would be required, if the period of (58 ± 3) hr suggested by Warner & Stephens (2019) or, respectively, (97.2 ± 0.3) hr suggested by Gorshanov et al. (2020) was correct. The latter is more consistent with the diameter estimate of (2.91 ± 1.19) km reported by Masiero et al. (2020) based on thermal modeling, which makes it our preferred option. Gorshanov et al. (2020) report also a lightcurve amplitude of 0.9 mag, which suggests an axis ratio of ~2.3. This high ratio is consistent with the possible contact-binary nature of Masaakikoyama as demonstrated by the radar images. The SC/OC ratio is consistently 0.34–0.36 through all three days of CW measurements. The OC radar albedo is challenging to estimate because of the uncertainty of the shape and size, but based on radar cross sections up to (0.93 ± 0.23) km^2, if the effective diameter were 1 km, the radar albedo would have to be more than 1.0, which effectively rules out this option. The second diameter estimate of ~1.67 km would be consistent with a more reasonable but still high OC radar albedo of 0.42, which would require a metal-rich composition (Shepard et al. 2015), and a geometric albedo of 0.17. The third, most likely diameter option of 2.9 km would limit the OC radar albedo to an average 0.14 and the geometric albedo to a low 0.06. Binzel et al. (2019) classify the spectral type as U (for unusual), but the spectra published online at http://smass.mit.edu/catalog.php appear closer to C-complex spectra than S-complex spectra. The radar albedo and the geometric albedo using the diameter option of 2.9 km would also be consistent with the other C-complex NEAs, as summarized in Section 5. Masaakikoyama will not pass within 0.2 au of Earth again until 2099 at 0.193 au.

4.3. (66391) Moshup (1999 KW4)

Goldstone Solar System Radar and Arecibo Radar observations in 2001 May during Moshup's 0.032-au flyby of Earth revealed it to be a binary asteroid (Benner et al. 2001; Ostro et al. 2006; Scheeres et al. 2006), which led to it becoming one of the best-characterized near-Earth binary asteroid systems. The 1.5 km primary asteroid Moshup and its 0.5 km satellite Squannit made a more distant flyby at 0.078 au in 2018, followed by a close flyby of Earth in 2019 at 0.035 au, which was similar to the 2001 encounter. The observed radar-scattering properties were similar to those over the past years: The SC/OC ratio varied from 0.34 to 0.56 with the average at 0.38, which is consistent with 0.45 ± 0.11 observed in 2001 (Ostro et al. 2006; Benner et al. 2008), but in the higher end of the typical SC/OC-ratio extent for Q-type NEAs such as Moshup (Popescu et al. 2019). The measured radar cross sections varied from 0.09 to 0.26 km^2 (inclusive of post-Maria gain uncertainties), which is comparable to the ~0.16 km^2 measured in 2002. This range constrains the OC radar albedo to 0.05–0.13, which is below the average for S- and Q-type NEAs but consistent with other metal-poor rocky bodies. The radar apparition in 2019 (the fifth in total) provided finer-range-resolution (7.5 m) radar images comparable to those obtained in 2001. These observations were part of the International

[17] www.naic.edu/~phil/tsys/tsysmon/y2013R12R7.pdf

Asteroid Warning Network observation campaign of the Moshup–Squannit system in 2019. The best obtained radar images were published by Reddy et al. (2022) as part of the discussion on the campaign and therefore are excluded from this paper. The next close approach within 0.1 au of Earth will take place in 2036 at 0.016 au and will be its closest flyby since its discovery.

4.4. (68347) 2001 KB67

Seven Arecibo radar tracks of 2001 KB67 revealed a rounded, featureless object with a visible range extent of at least 100 m (Figure 3, panel (c)). The maximum Doppler bandwidth of 1.1 Hz is consistent with a rotation period of 6.354–6.357 hr reported by Warner (2018) and Loera-Gonzalez et al. (2019) when the diameter is 250 m, or more if the subradar latitude is greater than zero. The decrease of the Doppler bandwidth from 1.1–1.2 Hz on May 28 to 0.7–0.8 Hz on June 1 implies higher subradar latitudes on the later days. No significant variations in the Doppler bandwidth and the visible extent were observed during the longest imaging track on 2018 May 29 that covered approximately one-quarter of a rotation, which suggests little elongation. The lightcurve amplitude of 0.19 mag (Warner 2018) suggests an axis ratio up to 1.2, which is consistent with the observed day-to-day variations in the radar cross sections and the Doppler bandwidths in the CW measurements. There is no published spectral information for 2001 KB67, but the SC/OC ratio range of 0.21–0.35 is comparable to S- and C-complex asteroids (Benner et al. 2008; Aponte-Hernández et al. 2020). With the assumed rotation period above, all measured SC/OC ratios were observed at different rotation phases in addition to the subradar latitude changing due to the sky motion. No systematic issues were identified, so the SC/OC ratio variation could indicate heterogeneous surface properties (i.e., variations in the particle size–frequency distribution, the near-surface density, or the composition as was briefly discussed in Section 3). Using the lower limit of the diameter above, the OC radar albedo is constrained up to 0.12 based on the average radar cross section of 6000 m^2, and the geometric albedo is up to 0.31 based on $H = 19.9$, which strongly favors the S-complex over a C-complex classification. The next close approach of 2001 KB67 to Earth comparable to the 2018 flyby at 0.024 au will be in 2051 at 0.022 au.

4.5. (68950) 2002 QF15

2002 QF15 has been observed at Arecibo in 2003, 2006, and 2016; however, the close approach at 0.088 au in 2019 was the closest yet. Several days of radar observations of 2002 QF15 showed a visible range extent up to 700 m, which is more consistent with the diameter estimate of (1.65 ± 0.555) km by Masiero et al. (2017), which was based on thermal modeling, than the diameter estimate of 2 km reported by Shepard et al. (2008a), which was based on visible extents of 0.8–1 km observed at Arecibo in 2003 and 2006. The radar images showed an undulating surface with hills or ridges and possibly large craters with protruding crater rims (two dark oval regions framed by thin lighter curves as displayed in Figure 3, panel (d)). Assuming a Doppler broadening of 1.0 Hz and $D = 1.65$ km, Equation (1) constrains the upper limit of the rotation period to 46 hr, which is consistent with the most recent period of 45.24 hr estimated from lightcurves by Warner & Stephens (2019a). However, some data showed Doppler broadening as wide as 1.3 Hz, which would either require the long axis to be >2.1 km or limit the period to 35.2 hr. Slow movement of features in the images is consistent with the period of several hours but cannot provide more precision with only a visual inspection. Given the observed variation in the visible extent and the Doppler broadening, an axis ratio up to 1.4 is possible, but shape modeling would be required to confirm the exact value. The measured SC/OC ratios of 0.26–0.31 were consistent, which indicates a homogeneous composition in particle size frequency and near-surface density despite the visible features, and they are comparable to the average SC/OC ratios for S-type NEAs such as 2002 QF15 (Binzel et al. 2019). Using $D = 1.65$ km, $H = 16.4$, and an average radar cross section of 0.472 km^2, the geometric albedo is 0.18 and the OC radar albedo is 0.22. The next flyby at less than 0.2 au takes place in 2028, whereas the closest approach in the next century will be in 2044 at 0.05 au.

4.6. (90403) 2003 YE45

The observations of 2003 YE45 in 2019 were the second time this asteroid was observed using radar. The images reveal a contact-binary structure of two lobes of comparable size (Figure 3, panel (e)). No neck is distinctly visible, but a neck cannot be ruled out. The images were very coarse due to the more distant flyby at 0.135 au in 2019 than in 2008, but based on the finer-resolution radar images obtained on 2008 July 6[18] during the 0.043 au flyby, each lobe is about 480–570 m across, suggesting a long axis of approximately 1 km. The slowly rotating asteroid has an estimated rotation period up to 500 hr based on lightcurves (Warner & Stephens 2019b) and a diameter estimate of 572 m based on observations by the NEOWISE team (Mainzer et al. 2016). This value is close to our estimated size of one lobe, which suggests that NEOWISE may have observed the asteroid when the lobes were aligned close to parallel to the line of sight. The slow change of orientation in the radar images is consistent with a long rotation period. The SC/OC ratio of this Sq-type asteroid (Binzel et al. 2019) is measured to be 0.27–0.34, which is comparable to other S-complex NEAs. The OC radar albedo is estimated to be up to 0.17 based on the maximum observed radar cross section of (32,600 ± 8500) m^2 and an effective diameter of ∼500 m because the long axis was aligned close to parallel to the line of sight; however, the shape and orientation of the asteroid could cause significant uncertainty. In 2008, when the long axis was aligned more orthogonally to the line of sight, the radar cross section was measured at (67,000 ± 17,000) m^2 (consistent with a radar albedo of 0.17 when effective diameter is 700 m). For the geometric albedo, the NEOWISE team's estimate was 0.493 ± 0.256 (Mainzer et al. 2016); however, using $D = 700$ m and $H = 17.7$ would set the geometric albedo at 0.30. The SC/OC ratios on the two consecutive days (2008 July 6–7) were inconsistent and thus will not be compared to the observations of 2019. The next close approach to Earth by 2003 YE45 will come in 2056 at 0.050 au, similar in distance to the 2008 flyby.

4.7. (141593) 2002 HK12

This was the second radar apparition of 2002 HK12, following the first one in 2002. We obtained six days of

[18] https://www.lpi.usra.edu/resources/asteroids/asteroid/?asteroid_id=2003YE45

imaging data at a range resolution of 7.5 m on 2019 August 11–17, during which the closest approach took place on August 16 at 0.063 au. The images (Figure 3, panel (f)) revealed a contact binary with a body-to-head size ratio of about 1.5 and a long axis up to about 700 m, which is close to the previous size estimates from 620 to 800 m (Wolters et al. 2005; Delbo et al. 2011). We observed the leading edge of the smaller lobe approaching at a rate of about 1.8 m/minute on 2019 August 11 at about 17:00 UT, when the lobes were seen momentarily at an equal range. This lobe movement rate and the maximum Doppler bandwidth up to 1.5 Hz are consistent with the rotation period of 12.691 hr reported by Wolters et al. (2005). Assuming this period and an equatorial subradar latitude, a Doppler bandwidth of 1.5 Hz suggests a long axis of ∼690 m. Non-principal-axis rotation cannot be resolved without full shape modeling. Spectroscopy indicates that 2002 HK12 is a C- or X-type asteroid (Binzel et al. 2019), but an unusually high SC/OC ratio up to 1.25 indicates that it could be, in fact, an E-type asteroid (in the modern taxonomic systems, E types are included into the broader X complex). The value is consistently high through seven days of observations and comparable to the SC/OC ratio of 1.09 ± 0.06 observed in 2002 (Benner et al. 2008), so systematic issues can be ruled out. The OC radar albedo is estimated using the maximum observed radar cross section, $\sigma_{\rm OC} = 34{,}100\ \rm m^2$, and two spherical lobes 275 m and 412 m across (or an effective diameter of 495 m), which suggests an OC radar albedo of 0.18. The geometric albedo is 0.38, which is significantly greater than previously reported estimates of 0.17–0.24 that were based on effective diameter estimates from 620 to 800 m (Delbo et al. 2011; Wolters et al. 2005) and thus more consistent with the average geometric albedos for E-type asteroids (Clark et al. 2004; Thomas et al. 2011). Due to the interesting spectral properties and a wealth of radar data, 2002 HK12 is a particularly compelling NEA for further analysis. The next comparable close approaches to Earth will come in 2036 at 0.067 au and in 2053 at 0.061 au.

4.8. (144332) 2004 DV24

The radar observations of 2004 DV24 revealed an elongated body with both angular and concave features (Figure 3, panel (g)). The Doppler broadening and the feature movement rate are consistent with a rotation period of (8.71 ± 0.01) hr (Reshetnyk et al. 2019). Using this period and the maximum observed Doppler broadening of 5.0 Hz in Equation (1), we can constrain the lower limit of the diameter to about 1.44 km. The observed visible range extents of 680–720 m are consistent with this diameter limit. Variation of the visible extents during each track and the radar cross sections from day to day is consistent with the reported lightcurve amplitude of 0.75 mag (Reshetnyk et al. 2019), which indicates an axis ratio close to 2.0. In some images we saw strong quasi-specular reflections indicating fine-grained, densely packed regolith coincident with the boundary of a large concavity, which could potentially be an impact crater. The CW echo-power spectra show daily a sharp spike that could be related to this feature (see an example in Figure 6, Appendix A). The SC/OC ratios range from 0.12 to 0.20, decreasing from 0.20 on 2019 August 17 by 0.04 per day through the following two days. No systematic issues were identified, so the range of values could indicate diversity in the regolith size–frequency distribution. Using the maximum $\sigma_{\rm OC} = (0.199 \pm 0.05)\ \rm km^2$, $H = 16.5$, and $D = 1.44$ km, we estimate the upper limit of the OC radar albedo at 0.12 and the geometric albedo at 0.21; however, the nonspheroidal shape of 2004 DV24 could cause misestimation of the albedos. This asteroid is another good candidate for further analysis. The next close approach comparable to the 2018 flyby at 0.056 au will take place in 2091 at 0.053 au, though more distant flybys at ∼0.1 au occur in 2035 and 2074.

4.9. (153814) 2001 WN5

The second radar apparition of 2001 WN5, following the first one in 2010, provided the first high-resolution (75 m) radar images (Figure 3, panel (h)). The size estimate based on the radar images, up to about 1 km along the longest axis, is consistent with the estimate of (932 ± 11) m reported by the NEOWISE team (Mainzer et al. 2011, 2016). The radar images show a concavity in the leading edge on 2019 August 24. There is little variation in the radar cross sections and Doppler broadening day to day, so the asteroid is likely relatively rounded with an axis ratio of up to 1.2 based on the Doppler-bandwidth variation. The imaging data had a very low S/N per scan, so feature tracking was not possible and the visible range extent on 2019 August 21 could be underestimated. The radar cross sections were consistent with $\sim 0.1\ \rm km^2$ measured in 2010 (Taylor et al. 2021) considering the 25% measurement uncertainty. The observed Doppler bandwidth of 6.6–8.0 Hz suggests a rotation period of up to 4.4 hr (assuming an equatorial view), consistent with a lightcurve estimate of 4.25 hr (Skiff et al. 2019; Warner & Stephens 2020a). The SC/OC ratio of this possibly L-type asteroid (Binzel et al. 2019) is 0.40 ± 0.07, which is consistent with the 0.40 ± 0.05 measured in 2010 (Taylor et al. 2021). The OC radar albedo is estimated at 0.16 when $D = 932$ m and $\sigma_{\rm OC} \approx 0.11\ \rm km^2$. The NEOWISE team estimates the geometric albedo at (0.097 ± 0.016) (Mainzer et al. 2016). Compared to the 0.098 au flyby in 2019, the next close approach will take place in 2028 at only 0.001 7 au, within the orbit of the Moon, making 2001 WN5 an excellent target for multiwavelength observations, especially in preparation for the extremely close flyby of (99942) Apophis in 2029.

4.10. (162082) 1998 HL1

The first radar apparition of 1998 HL1 revealed a rounded object with a visible extent up to 180 m (Figure 3, panel (i)). Bright speckles of quasi-specular reflections in some scans near the leading edge could indicate flat facets, although noise spikes cannot be fully ruled out either, and subtle concavities indicate valleys or craters. The diameter and the rotation period estimates based on photo and polarimetric analyses are 326 m and 14.43 hr (Kiselev et al. 2019), respectively, with the geometric albedo estimated at 0.35. Other sources report rotation periods from 3.02 hr (Carreño et al. 2020) to 11.78 hr (Warner & Stephens 2020a) (with uncertainties less than 0.01 hr). The latter estimate was based on a lightcurve that was flagged as ambiguous but consistent with the (11.60 ± 0.01) hr period found by Franco et al. (2020). Feature tracking was challenging but we could observe a concave feature receding at a rate of up to 2–3 m per minute on 2019 October 26 at 03:57–04:55 UT, which would be consistent with a period in the range of 6–10 hr when using $d_r = 180$ m and Equation (8). The maximum Doppler bandwidth of 1.1 Hz from the CW observations constrains the upper limit of the rotation period to 9 hr using 360 m (Equation (1)), which would be consistent with the feature movement rate. A period of 14.43 hr would require a lower limit of the diameter at 570 m to produce the observed Doppler bandwidth, which is inconsistent with the visible extent. Assuming the period of 11.78 hr, as estimated by Warner & Stephens (2020a), would constrain the lower limit of the diameter to about 450 m, which is more consistent with the visible extent than 570 m and is also consistent with the feature-tracking rate if we increase d_r accordingly to 225 m. Spectrometric information for 1998 HL1 is not available, but according to Kiselev et al. (2019), the photometric and polarimetric information aligns with other S-complex asteroids, and the SC/OC ratio of 0.29–0.34 is in the common range for S-complex NEAs as well. The OC radar albedo based on $\sigma_{\rm OC} = (15000 \pm 4000)$ m^2 and a diameter of (450 ± 50) m is estimated at 0.10 ± 0.05 and the geometric albedo at 0.20 ± 0.05. Both albedo estimates are consistent with the S-complex classification. The next comparable close approach will take place in 2051 at a distance of 0.047 au, only 0.003 au farther than that in 2019.

4.11. (264357) 2000 AZ93

The delay-Doppler radar images of 2000 AZ93 show a visible extent of about 50 meters (Figure 3, panel (j)); however, the S/N of the images is very low, so the illuminated hemisphere probably was not fully visible. This also constrains the evaluation of the shape, which appears rounded, possibly angular, but not bifurcated. The NEOWISE team's thermal-modeling-based diameter estimates varied from (113 ± 29) m with a geometric albedo of 0.55 ± 0.18 (Mainzer et al. 2012) to (439 ± 106) m with an albedo of 0.037 ± 0.024 (Mainzer et al. 2016). Using the measured OC radar cross section of 10,000 m^2, the OC radar albedo would have to be 1.0 if the diameter were 113 m, which would only be possible for a metallic object. A diameter of 439 m would be consistent with an OC radar albedo of 0.07. Binzel et al. (2019) reported that the spectral classification of 2000 AZ93 falls in the S complex (S, Sq, or Q), for which typical geometric albedos are on average 0.27 (Thomas et al. 2011), and radar albedos tend to fall in the range 0.1–0.3 based on the other NEAs included in this paper (Figure 5 and Section 5). Using the radar-albedo range above would constrain the diameter from about 200 m to 350 m, whereas using the average geometric albedo would suggest a diameter close to 150 m, which is more consistent with $D \approx 200$ m than 350 m, so we estimate the OC radar albedo at 0.32 ± 0.10 and the geometric albedo at 0.16 ± 0.05. The Doppler broadening was estimated at 0.3 Hz, which indicates a spin period up to 16 hr when using $D \approx 200$ m and Equation (1). No lightcurve data are available. Also, no reliable measurement of the SC/OC ratio was obtained due to the LNA problem in 2019 December (as described in Section 3 and illustrated in Figure 7). The next close flyby of Earth will be in 2031 at 0.041 au; in fact, 2000 AZ93 makes close approaches within ∼0.05 au of Earth every 20 yr, i.e., 2011, 2031, 2051, and so on for centuries.

4.12. (398188) Agni (2010 LE15)

Agni was observed for three nonconsecutive days during its second radar apparition. The first, in 2014 August, had provided only one day of images. The radar images revealed a contact binary with two lobes of different sizes: at least 300 m and 150 m across (Figure 3, panel (k)). The NEOWISE team's effective diameter estimate was (462 ± 6) m (Mainzer et al. 2011). A rotation period of 21.99 hr (Warner 2015) is consistent with the observed Doppler broadening up to 0.6 Hz, but only if the long axis is at least 477 m, which indicates that the lobes are elongated or larger than the visible range extent suggests. The slow change of orientation during the imaging is consistent with a rotation period of tens of hours. An effective diameter of ∼370 m that assumes two rounded lobes, one 330 m (the body) and the other 165 m across (the head), would require a greater geometric albedo (0.22) than the 0.137 ± 0.024 suggested by Mainzer et al. (2011). The OC radar albedo based on the maximum radar cross section of 23,700 m^2 and $D = 462$ m is 0.14, or 0.22 if we assume $D = 370$ m. The SC/OC ratio of this Sq-type asteroid (Popescu et al. 2019) was measured to be 0.13–0.28 depending on the day. The highest SC/OC ratio was observed on July 26, when Agni was oriented with the head in front of the body and the lowest SC/OC ratio was observed on 2019 August 3, when the body was oriented closer than the head as shown in Figure 3, panel (k). The SC/OC ratio was measured at 0.23 on 2014 August 1, when the head was oriented closer than the body, which is consistent with the observations in 2019. This could indicate that the head is covered with more wavelength-scale regolith than the body. The next close approach to Earth within 0.1 au will take place in 2055 at 0.029 au, less than half its 2018 distance.

4.13. (418849) 2008 WM64

2008 WM64 has had several radar apparitions from 2012 to 2019: once in 2012 and annually in 2015–2019. Here, we focus on 2017 December 21–23 and 2018 December 24. In 2019, systematic issues likely played a major part, so those observations were not included in the analysis. The radar images revealed a flat, possibly concave surface geometry on one side and more rounded on the other side with a visible range extent varying from 90 m to 150 m. Figure 3, panel (l), shows the rounded side. The feature progression rate in the radar images on 2018 December 24 and over the three days in 2017 is consistent with a rotation period of 2.4055 hr (Warner et al. 2009). Using this period and the maximum Doppler broadening of 2.4 Hz observed in the images with Equation (1), we can estimate the long axis at 210 m and an axis ratio up to 1.5, which is consistent with the observed visible range extents and the radar cross-section variation. The relatively short period and a wide time span of the observations improve this asteroid's prospects as a good shape-modeling target. The most reliable measurements were done in 2017: We measured SC/OC ratios 0.25–0.28 over three days covering all orientations, and based on $H = 20.6$ and $D = 230$ m, we estimate a geometric albedo of ∼0.20. Both values are consistent with its Sa-type spectrum (Perna et al. 2018). The SC/OC ratio of 0.47 measured on 2018 December 24 was inconsistent with the other measurements for no self-evident reason and would require further investigation, such as shape modeling, to explain. It could be related to a regolith size–frequency distribution anomaly at the subradar point during a short track, and a narrower Doppler bandwidth also suggests a subradar point at a different latitude from the other measurements. Based on an average radar cross section of 3200 m^2 and an effective diameter estimate of 200 m, we estimate the OC radar albedo at ∼0.10. This asteroid will not make another close approach to Earth within 0.1 au until 2124 at 0.069 au.

4.14. (441987) 2010 NY65

2010 NY65 was observed annually from the Arecibo Observatory in 2014–2020, with the closest approaches in 2018 and 2019. The 2018 and 2019 apparitions were the fifth and sixth radar apparitions. The visible range extents of 75–120 m are consistent with the thermal observations that estimated a diameter of (228 ± 12) m with a low geometric albedo of 0.071 ± 0.014 (Mainzer et al. 2011). The shape appears generally rounded but exhibits a small bump, which is visible, for example, on the approaching side in Figure 3, panel (m). The maximum observed CW Doppler bandwidth of 1.0 Hz constrains the period up to 6 hr when $D = 228$ m, and tracking the progression rate of the bump provides an independent consistency check of the rotation period. We observed the leading edge of the bump approaching at the fastest three pixels (22.5 m) per eight to nine scans (transmit–receive cycles of 68 s), which suggests (using Equation (8)) a period of (5.1 ± 0.3) hr and is thus consistent with the lightcurve-based periods that have been reported in the range from 4.59 hr to 5.59 hr (Warner & Stephens 2019). Assuming a ∼5 hr period, a 90° phase difference should be seen in images 1.25 hr apart. Using the images obtained through 1.5 hr on 2018 June 20, we find the Doppler broadening varying by no more than 10%, which is consistent with the little variation observed in the radar cross sections day to day. This indicates little elongation. The SC/OC ratio of this Sv-type asteroid (Perna et al. 2018) was measured at 0.27–0.40, comparable to that of other S-complex NEAs. Further modeling could explain how this SC/OC-ratio variation relates to the observed bump. Moreover, the uniquely large number of consecutive years of radar observations makes 2010 NY65 an exceptionally suitable object for various further studies on the physical and dynamical characterization of individual NEAs. The OC radar albedo is estimated at 0.15 based on an average OC radar cross section of 6400 m^2, which is consistent with the previous years' observations. This asteroid will not make close approaches within 0.1 au of Earth again until 2179.

4.15. (454094) 2013 BZ45

The second radar apparition of 2013 BZ45 in 2019 August showed a rounded object 130–180 m across (Figure 3, panel (n)). This size range is consistent with the NEOWISE team's estimate of (167 ± 53) m across with $p_V = 0.110 \pm 0.087$ (Masiero et al. 2017). The Doppler bandwidth remains at (0.5 ± 0.1) Hz based on the CW observations and imaging from 2018 August 2 to 5. Feature tracking was not possible due to the low S/N, but the rotation period based on the Doppler bandwidth and a diameter of 167 m is 11.6 hr or less depending on the subradar latitude. There was a negligible difference compared to the first radar apparition in 2015 January 27–February 3 in terms of observed shape, size, and bandwidth, which ensures that several geometries were observed and that a rotation period of several hours is credible. The sky motion of 11° over the three days rules out the lightcurve-based estimate of 0.483 1 hr by Pravec et al.,[19] which would require the subradar latitude to remain at about 87° through the three days. It was noted that this estimate was based on a fragmentary lightcurve and could be incorrect. The observed SC/OC ratio range was 0.34–0.43. The OC radar albedo is estimated at 0.22 using the average of the measured radar cross sections, 4810 m^2, which is comparable to that measured in 2015. Spectroscopic information is not available for 2013 BZ45, but the geometric albedo is more comparable to the average for C-complex NEAs than that of S-complex NEAs. The radar-scattering properties cannot distinguish between the S and C complexes but can rule out a metal-rich X complex that could have a low geometric albedo, and the SC/OC ratio effectively rules out V- and E-type classification. The next close approaches within 0.1 au of Earth will occur in 2060 and 2061 at 0.067 and 0.071 au, respectively.

4.16. (481394) 2006 SF6

The delay-Doppler images of 2006 SF6 revealed a possible contact binary with approximately a 1:2 head-to-body size ratio, with the head at least 120 m and an elongated body at least 225 m across with a thick neck connecting the lobes (Figure 3, panel (o)). The maximum visible range extent was observed to be 315 m on 2019 November 13. The change in orientation observed in the radar images during the tracks helped independently confirm the rotation period of ∼11.5 hr reported by Warner & Stephens (2019, 2020a) based on lightcurves. On the first two days, November 11–12, the head was approaching and the body receding, whereas on the later days we observed the body approaching and the head receding, as expected based on the 11.517 hr period. The longest track on 2019 November 12 covered up to 60° of subradar longitudes. Unfortunately, the S/N of the images was quite low that day, but November 13–14 had better S/N with subradar longitude coverage greater than 50°. Through the five days, the coverage of subradar longitudes reached approximately 140°, which improves the shape-modeling prospects. Using the rotation period of 11.517 hr and the maximum CW Doppler broadening of 0.9 Hz, we can use Equation (1) to derive a lower limit of 370 m for the long axis. Using 150 m as the intermediate axis, the 1.0 mag lightcurve amplitude (Warner & Stephens 2019, 2020a) would be consistent with a long-to-intermediate-axis ratio of ∼2.5 and an effective diameter of approximately 240 m. The range of SC/OC ratios from 0.22 to 0.44 is not unexpected for an S-type asteroid.[20] The SC/OC ratio decreased gradually from 0.44 to 0.22 over five days, possibly due to the orientation and/or heterogeneous surface properties as the orientation phase also progressed gradually during the radar tracks. Systematic issues cannot be fully ruled out, as the OC polarization channel's LNA was exhibiting problems at the time (Figure 7), which would have caused overmeasurement of the SC/OC ratio. We measured elevated SC/OC ratios for three other NEAs observed on November 11–12 (2010 JG, 2019 QY1, and 2019 UN12), whereas 2011 YS62 observed on November 13–14 had a more common SC/OC ratio of ∼0.2 measured on both days. The OC radar albedo is estimated at 0.17 based on an effective diameter of 240 m and the maximum radar cross section, $\sigma_{\mathrm{OC}} = 7530$ m^2, and the geometric albedo is 0.34, which is slightly above the average for S-type asteroids (Thomas et al. 2011). The next comparable close approach to Earth by 2006 SF6 will take place in 2044 at a more distant 0.040 au.

4.17. (494999) 2010 JU39

Three radar tracks of 2010 JU39 revealed an object with an irregular shape and a visible range extent up to 135 m

[19] http://www.asu.cas.cz/~ppravec/newres.htm

[20] http://smass.mit.edu/catalog.php

(Figure 3, panel (p)). The Doppler broadening of 0.15 Hz suggests an upper limit on the spin period of 50 hr for an object that is 270 m across. This is consistent with the lightcurve-based estimate of 30.2 hr (Warner & Stephens 2019a). If we assume the spin period to be 30.2 hr, the lower limit of the long axis is 164 m using the maximum Doppler bandwidth of 0.15 Hz and Equation (1). The radar cross sections vary from 5000 m^2 to 14,500 m^2, and, assuming $P = 30.2$ hr, they were measured at rotation phases with a $\sim 90°$ difference, which suggests that the long-to-short axis ratio could be as much as 3. In contrast, the ratio of the maximum-to-minimum Doppler bandwidths suggests a long-to-intermediate axis ratio of 1.4. Both ratios are subject to projection effects caused by the changing subradar latitude and the irregular shape. The lightcurve magnitude of 0.45 reported by Warner & Stephens (2019a) is more consistent with the Doppler-bandwidth-based estimate but is also subject to projection effects. A vertical shadow through the asteroid hints at a contact-binary nature, but the narrow Doppler bandwidth limits the detail in the frequency dimension. For an absolute magnitude of 19.6 and an effective diameter of 270 m, the geometric albedo is 0.35 and the OC radar albedo is 0.17 when the radar cross section is assumed as an average of 10,000 m^2. The SC/OC ratio is 0.23–0.42, where some variation due to the orientation is possible. The spectral type is not known for 2010 JU39, and the radar-scattering properties rule out neither S- nor C-complex classification, but the relatively high geometric albedo suggests S-complex rather than C-complex classification. The next close approach to Earth takes place in 2034 at a closer distance of 0.048 au.

4.18. (505657) 2014 SR339

One day of radar observations of 2014 SR339 revealed an elongated object with a shallow ($\sim$30–40 m deep) but distinct concavity (Figure 4, panel (a)). We observed 2014 SR339 rotating a little over 45° during a 1.3 hr imaging track, which is consistent with the rotation period of 8.71 hr reported by Franco et al. (2018). The visible extent of the intermediate axis is about 400 m and that of the long axis is about 990 m. Using the maximum observed Doppler bandwidth of 4.2 Hz and the rotation period of 8.71 hr suggests a long axis of at least 1300 m. Furthermore, Franco et al. (2018) reported a lightcurve amplitude of 0.75, which suggests an axis ratio of about 2. The NEOWISE team suggested a diameter of (971 ± 367) m, which would be consistent with an ellipsoid with a long axis of $\sim$1380 m and an intermediate axis of $\sim$690 m, and a geometric albedo of 0.068 ± 0.074 based on thermal modeling (Nugent et al. 2015). The low geometric albedo and the observed SC/OC ratio of 0.26 ± 0.01 are both consistent with the B-type taxonomy indicated by spectroscopy (see footnote 20). The OC radar albedo is estimated at 0.5 ± 0.2 assuming an effective diameter of 1.0 km and the measured $\sigma_{\rm OC} = (0.41 \pm 0.10)$ km^2. This radar albedo suggests a dense, possibly metal-rich near-surface (Shepard et al. 2008c) and is much greater than radar albedos observed for other B-type asteroids, e.g., for (101955) Bennu at 0.12 (Nolan et al. 2013) and for (3200) Phaethon at 0.06 (Taylor et al. 2019a). However, it is comparable to the radar albedo observed for (2100) Ra-Shalom at 0.36 ± 0.10 (Shepard et al. 2008b), for which B-type spectra have been observed (Binzel et al. 2019) as well as Xc-, C-, and K-type spectra (Shepard et al. 2008b). There were no systematic issues that could have caused overestimation of the cross section, and the complex shape could play only a limited role in the projected area, as the inferred dimensions are consistent with thermal modeling and lightcurves. Therefore, these observations suggest that asteroids with B-type spectra can have more diverse surface characteristics than what has been observed for asteroids such as Bennu and Phaethon. The next close approach to Earth by 2014 SR339 comparable to that in 2018 will be in 2058 at 0.042 au.

4.19. (509352) 2007 AG

The radar imaging of 2007 AG over five days showed a rounded object with a visible range extent of 170–190 m, which suggests a diameter of at least 400 m (Figure 4, panel (b)). The Doppler bandwidth increased from 2.5 Hz on 2017 December 22 to 5.0 Hz on 2018 January 3, indicating the subradar latitude transitioning toward equatorial latitudes on the later dates. Assuming a diameter of 400 m and a spherical object, the Doppler broadening suggests a rotation period of up to 2.2 hr on 2018 January 3 when the subradar latitude was likely closest to the equator. The radar cross section decreased gradually during the first hour of imaging on December 26, 28, and 29 by about 30%, and from 53,800 m^2 on December 12 to 37,500 m^2 on January 3, which indicates an axis ratio of at least 1.4. No lightcurve data were available to check for consistency. Using $D = 400$ m and an average radar cross section of $\sim$44,000 m^2 places the OC radar-albedo estimate at about 0.35, which is a relatively high value compared to the average for other NEAs presented here (see Section 5) and could indicate high near-surface density. The SC/OC ratio extends from 0.22 ± 0.04 to 0.42 ± 0.02, which is a common range observed for S- and C-complex NEAs. The first observation day's SC/OC-ratio measurement was the least consistent and the least reliable one of the six days; excluding it constrains the range to $\sim$0.3–0.4. The remaining SC/OC-ratio variation is possibly due to a heterogeneous surface, because the system temperature was stable through the observation days, and the possible pointing/focusing issues at the beginning of the tracks were reduced during the data processing. Furthermore, we observed the reflectivity of the leading edge increasing for about 15–20 minutes, repeating every 45–48 minutes on December 26, 28, and 29, which is consistent with the interpretation of a heterogeneous surface and adds further independent constraints to the spin rate. The periodical reflectivity and SC/OC-ratio variations could be caused by a larger flat region that enhances locally the quasi-specular reflection, or a local anomaly in the regolith composition. Confirming whether the values vary as a function of the rotation phase and what role they played in the observed radar cross sections would require further analysis that is not in the scope of this paper. The geometric albedo is 0.1 when $H = 20.1$. The visual and radar-scattering properties are thus comparable to those of (2100) Ra-Shalom (B, K, or Xc type) (Shepard et al. 2008b). The next comparable close approach to Earth by 2007 AG occurs in 2048 at a similar distance of 0.061 au.

4.20. (522684) 2016 JP

2016 JP has passed Earth at less than 0.4 au every year since 2011, during which the closest approach took place on 2018 April 20. Unfortunately, the Arecibo telescope was undergoing maintenance at that time, but the second-closest approach at 0.049 au in 2019 April provided us with six days of radar observations. The diameter based on the visible range extents is 120–200 m and the shape is rounded with no distinct features (Figure 4, panel (c)). The Doppler broadening of 1.0–1.2 Hz (variation observed during one track as well as day to day) suggests a spin period of up to 5 hr. This is consistent with a lightcurve-based spin period of 3.290 5 hr by Pravec et al. (see footnote 19) and a nonzero subradar latitude; it effectively rules out the 37.4 hr period suggested by Warner (2018). Using the 3.290 5 hr rotation period solution, a Doppler broadening of 1.2 Hz, and Equation (1), we find a lower bound on the maximum pole-on breadth of 140 m. The variation in the Doppler broadening depends on the orientation phase, indicating an axis ratio up to 1.2. No clear change in the Doppler broadening that would be indicative of a significantly changing subradar latitude was observed over several days; this was expected because the orbit of 2016 JP is exceptionally similar to that of Earth. The SC/OC ratio is relatively high: a seven-day average is 0.78, which is closest to the average SC/OC ratio for V-type asteroids, although the E-class cannot be ruled out (Benner et al. 2008). Using the maximum radar cross section of $(3800 \pm 1000)\ \mathrm{m}^2$ and $D = 160$ m, we estimate the OC radar albedo at 0.19 and the geometric albedo at 0.25 ($H = 21.1$), which is low compared to the average geometric albedos for V- and E-type asteroids estimated by Thomas et al. (2011), who found an average of 0.42 for V-type asteroids. Although an S-complex asteroid with an unusually high SC/OC ratio could be a possible explanation, it is also possible that the geometric albedo is underestimated due to a misestimated absolute magnitude, because the possible opposition effect has not been constrained well due to the lack of photometric observations below a phase angle of 30° since this NEA was discovered. 2016 JP will not approach within 0.1 au of Earth during the next century.

4.21. (523788) 2015 FP118

The radar observations of 2015 FP118 revealed a rounded asteroid with few features visible during the several imaging tracks lasting more than 1.3 hr (Figure 4, panel (d)). Feature tracking was not possible, but if we calculate the diameter based on the maximum Doppler bandwidth ($B = 2.8$ Hz) from the CW observations and $P = 3.092$ h (Warner & Stephens 2019), the diameter is at least 310 m. Using $P = 6.21$ hr, which was suggested as another option by Pravec et al. (see footnote 19), would require the diameter to be at least 630 m. The visible range extent is consistently less than 100 m, indicating a diameter of about 200 m, but such a small diameter would require the asteroid to have a very high geometric albedo of 0.76 (when $H = 19.4$) and an OC radar albedo of 0.41 (when the average $\sigma_{\mathrm{OC}} = 13{,}000\ \mathrm{m}^2$). Moreover, the S/N of the images was relatively low, so part of the illuminated hemisphere could have remained invisible simply due to the noise, and the visible extents are more likely underestimated, so 200 m is very likely an underestimation. In contrast, $D \approx 310$ m would indicate $p_V \approx 0.32$ and $\hat{\sigma}_{\mathrm{OC}} \approx 0.17$, which are more common values for an Sq-type asteroid (see footnote 20). A diameter of about 630 m would require very low albedos that would be more consistent with C-complex asteroids and is thus likely an overestimation, so the lower limit of 310 m is our preferred option. The axis ratio is up to 1.3 based on the range of Doppler bandwidths measured from 2.1 Hz to 2.8 Hz. The SC/OC ratio extends from 0.17 ± 0.03 to 0.40 ± 0.09 depending on the day, which could indicate heterogeneous surface properties, but would require further analysis to confirm. Apart from the last observation day, 2018 September 14, which can be considered the most unreliable one based on the S/N in both polarization senses (Table 4), the SC/OC ratio remained from ∼0.2 to ∼0.3. This is consistent with an Sq-type classification. The next close approach to Earth by 2015 FP118 is at 0.055 au in 2052, which will be more distant than the 2018 apparition at 0.031 au.

4.22. (524594) 2003 NW1

Three days of radar imaging revealed 2003 NW1 to be a contact binary with each lobe approximately 300–400 m across (Figure 4, panel (e)). The narrow Doppler bandwidth of 0.2–0.3 Hz indicates a very long rotation period, up to about 100 hr, but the subradar latitude could be at a high angle based on the delay-Doppler images on 2018 December 13–14, where the two lobes are located at a nearly equal range (60 m separation) while clearly overlapping in the frequency dimension. The Doppler bandwidth remains narrow from December 12 through December 15 (with a sky motion of less than 8° per day), further supporting a slow rotation rate. The range difference between the leading edges of the lobes is about 400–450 m on December 12 and 180 m on December 15. On both days, the lobes are oriented nearly parallel to the line of sight with the difference that on December 12 (based on imaging starting at 23:38 UT), the farther lobe is mostly shadowed by the closer lobe, whereas on December 15 (imaging starting at 00:07 UT) both lobes are visible. On December 12, we observed the range of the closer lobe increasing at a rate of about 1 pixel (7.5 m) per three transmit–receive cycles (7.4 minutes) while the farther lobe was relatively stationary. Therefore, estimating the period using Equation (8), the radar observations are consistent with the period estimate of (37.7 ± 0.5) hr derived using lightcurves (Warner & Stephens 2019c). We observed a hint of a neck on December 14, effectively ruling out a binary nature. Assuming a single-lobe diameter of 350 m and a radar cross section of $22{,}200\ \mathrm{m}^2$ (from the only reliable CW measurement obtained on December 12 when the lobes were oriented close to parallel to the line of sight), the OC radar albedo is estimated at $\sim 0.23 \pm 0.06$. The geometric albedo is 0.24 when $H = 18.7$ and the effective diameter is 490 m. Both albedos could be incorrectly estimated due to the complexity of the asteroid's shape and orientation; therefore, we welcome shape modeling for this NEA in the future. The measured SC/OC ratio of 0.12 ± 0.02 is relatively low and effectively rules out E and V classes. This asteroid will not approach within 0.1 au of Earth again until 2184 when it makes a close flyby at 0.019 au.

4.23. 2010 GT7

One day of radar imaging revealed 2010 GT7 to be a contact binary with the head and body approximately 100 m and 220 m across based on the visible extent of each lobe, respectively (Figure 4, panel (f)). This suggests a slightly larger effective diameter of ∼240 m than the NEOWISE team's estimate of (216 ± 5) m (Mainzer et al. 2011) but does not rule it out given the uncertainties. The neck between the lobes is very faint but visible when changing the contrast of the image (available in FITS format through Figshare; Virkki et al. 2022). No lightcurve-based spin rate is available. The narrow Doppler bandwidth constrains the rotation period up to 18 hr assuming an equatorial subradar latitude. During the 47 minute radar-imaging track on 2018 December 21, the smaller lobe moved one pixel (about 7.5 m) farther in the range dimension every 7.2 minutes while the larger lobe was not observed to move, which would suggest a full rotation in about 16 hr when the distance between the lobes is assumed 160 m (using Equation (8)). Moreover, we obtained CW measurements on two consecutive days, which hint that the smaller lobe moved from the receding side on the first day to the approaching side on the second day, which is consistent with a rotation rate of about 15–18 hr. The observed SC/OC ratios of 0.33–0.44 are within a common range for S-complex NEAs. The difference between the SC/OC ratios could indicate a heterogeneous surface because they are obtained at different orientation phases. Confirming the cause of the SC/OC ratio variations would require modeling work that is not within the scope of this paper. Assuming an effective diameter of 240 m, the maximum $\sigma_{OC} = 8200$ m^2, and $H = 20.2$, the OC radar albedo and the geometric albedo are estimated to be ∼0.18 and ∼0.26, respectively. These values are consistent with a possible S-complex classification. This asteroid will not make a comparable close approach to Earth within 0.1 au until 2195 at 0.07 au.

4.24. 2010 JG

The radar images of 2010 JG showed a rounded object approximately 200 m in diameter, but any features are difficult to distinguish due to a low S/N (Figure 4, panel (g)), which causes uncertainty in both the size and the shape estimates. This diameter estimate is consistent with that reported by the NEOWISE team: (192 ± 3) m (Mainzer et al. 2011), which supports the credibility of the radar imaging results. Rotation periods have not been reported based on lightcurves, but the Doppler bandwidth of 1.5 Hz (from the CW measurements) suggests an upper limit of about 4 hr assuming a 200 m sphere and an equatorial subradar latitude. The S/N is low, making analysis based on individual scans challenging, but the echo does not appear fully symmetric, which hints at a possible elongation or surface features. The geometric albedo is 0.21 ± 0.09 (Mainzer et al. 2011). The average OC radar cross section was (2440 ± 620) m^2, which suggests a low radar albedo: ∼0.08 (assuming a diameter of 200 m), and the average SC/OC ratio was ∼0.4. However, because the observations were conducted on 2019 November 11–12, when the LNA used for the OC polarization channel began to show signs of failing, the OC radar cross sections could be underestimated and the SC/OC ratios overestimated. The next comparable close approach to Earth by 2010 JG will occur in 2080 at 0.054 au.

4.25. 2011 HP

Two days of radar observations of 2011 HP in 2019 showed a rounded object with a visible extent up to 150 m (Figure 4, panel (h)). The maximum Doppler bandwidth was comparable on both days: 1.7 Hz on May 29 and 1.6 Hz on May 30. With equatorial subradar latitude and assuming a diameter of 300 m (Equation (1)), the Doppler broadening constrains the rotation period to an upper limit of 4.7 hr. This is consistent with the lightcurve-based rotation period of 3.94 hr (Warner & Stephens 2019a; Skiff et al. 2019) if the subradar latitude is ∼22° on May 29 and ∼29° on May 30. The leading edge oscillates on timescales much less than the period as the asteroid rotates, which indicates surface features of 20–25 m size scale. The maximum-to-minimum Doppler-bandwidth ratio was 1.2 (1.6 Hz/1.3 Hz) during the 2.4 hr radar imaging track on May 30, and the ratio of the radar cross sections was ∼1.5. The rotation-phase difference between the 6–7 minute CW measurements, which yielded radar cross sections (14, 400 ± 3600) m^2 and (21, 100 ± 5300) m^2, was in the range from 70° to 80°, i.e., close to the expected maximum difference between the cross sections. The 0.4 mag amplitude of the lightcurves reported by Warner & Stephens (2019a) is consistent with our axis-ratio estimate of up to 1.5. The time between the minimum and maximum Doppler bandwidths, about 59 minutes or presumably one-quarter of a full spin, provides another independent confirmation for the spin rate. Assuming a 300 m effective diameter, $\sigma_{OC} = (17{,}800 \pm 3400)$ m^2 indicates a higher-than-average OC radar albedo of 0.25 ± 0.05, while H = 21.8 (Warner & Stephens 2019a) indicates a very low geometric albedo of ∼0.04. The spectrometric observations suggest a B-type classification (see footnote 20), which is consistent with the very low geometric albedo. However, the radar albedo is in the higher end compared to other B-type NEAs, although not unparalleled (see, e.g., the section on (505657) 2014 SR339 above). Hicks et al. (2011) suggested Xc type, which would be a better fit for the relatively high radar albedo but low geometric albedo. The SC/OC ratio is measured at 0.37 ± 0.03, which is also in the higher end compared to other B-type asteroids. The next comparable close approach to Earth will occur in 2138 at 0.039 au.

4.26. 2011 WN15

The radar images obtained during this second radar apparition of 2011 WN15 at a distance of 0.058 au revealed a rounded, featureless object with a diameter of 300–400 m (Figure 4, panel (i)) and indications of being a rare metal-rich NEA. The Doppler bandwidth of 3.1 Hz and an effective diameter estimate of 350 m suggests a rotation period up to 3.1 hr or less if the subradar latitude is not equatorial (based on Equation (1)). This is closer to the 2.965 6 hr period derived from lightcurves by Pravec et al. than the 1.948 hr period suggested by Warner (2016). However, the observations during the first radar apparition in 2015 December 4–6, when the object passed Earth at a distance of 0.083 au, yielded a Doppler bandwidth of 4.1 Hz, which would place the upper limit of the rotation period at 2.4 hr assuming the same effective diameter. The Doppler bandwidths measured in 2019, from 3.1 Hz to 3.7 Hz, were less than those measured in 2015 (the Doppler bandwidth increased from 3.9 Hz to 4.8 Hz), which suggests a larger subradar latitude in 2019. Both in 2015 and 2019, the cross-section differences per day were significant: In 2015, the cross sections systematically decreased over the four days of observations from more than 60,000 m^2 to 42,000 m^2 while the Doppler bandwidths increased. By contrast, in 2019 σ_{OC} increased from 51,000 m^2 to nearly 82,000 m^2 in one day. This could be caused by elongation or heterogeneous surface density distribution, but shape modeling would be required to confirm. Systematic issues with the OC polarization channel can be ruled out because the observation took place after the failing LNA was moved to the SC channel and the functional LNA to the OC channel. The radar albedo is estimated to be in the range of 0.4–0.6, depending on which cross section and diameter estimate is used. The high radar albedo in addition to the prominent specular reflection at the leading edge suggests a high near-surface density and possibly a notable abundance of metals for this X-type asteroid (see footnote 20). For comparison, a radar albedo of 0.58 ± 0.15 was observed for the M-type asteroid 1986 DA by Ostro et al. (1991). The geometric albedo is 0.16 when using the same size estimate, $D = 350$ m, and H = 19.6. We did not obtain reliable measurements with the SC polarization in 2019 due to the LNA problem, but in 2015, the SC/OC ratio was measured to be 0.34 ± 0.02. This does not rule out the possible metallic nature of this NEA when comparing it to the SC/OC ratios of metallic MBAs (Shepard et al. 2015). Due to the small number of metallic NEAs, statistical comparisons with other NEAs are not robust, and comparing to the SC/OC ratios of MBAs could possibly be questionable as well because as Benner et al. (2008) showed, the SC/OC ratios of NEAs and MBAs differ in many taxonomic classes. The next comparable close approach to Earth by 2011 WN15 will occur in 2066 at 0.048 au; the close approach at 0.2 au in 2023 will not provide a very good radar-observation opportunity, but other observations are encouraged.

4.27. 2011 YS62

This was the second radar apparition of 2011 YS62; the first was in 2015, but at the time only coarse-resolution images were obtained. The radar images in 2019 November revealed a rounded object with a visible range extent of at least 300 m (Figure 4, panel (j)); however, the images had a very low S/N that could lead to misestimation of the size and shape. Warner (2016) estimated a rotation period of 17.53 hr using lightcurves. Using Equation (1) with the 17.53 hr period and the Doppler bandwidth of 1.2 Hz constrains the lower limit of the diameter to 760 m. This would constrain the upper limit of the radar albedo to 0.16, when $\sigma_{\mathrm{OC}} \approx 72{,}500\ \mathrm{m}^2$, and the upper limit of the geometric albedo to only 0.04 when H = 19.7. Although the LNA issue could have caused an undermeasurement of the radar cross section, and consequently the radar albedo, a geometric albedo this low most likely suggests a C-complex asteroid with a diameter that cannot be much larger than estimated here. The SC/OC ratios of 0.20–0.23 are within the common range for both S- and C-complex NEAs and do not appear elevated, which increases the credibility of the OC cross section measurement. In 2074, 2011 YS62 will make its next comparable close approach to Earth at 0.108 au.

4.28. 2012 MS4

Two days of radar imaging revealed 2012 MS4 to be a contact binary with both the head and body at least 250 m across, connected by a thinner neck (Figure 4, panel (k)). The Doppler bandwidth is only 0.32 Hz along the long axis covering both lobes. On the first day, the lobes were oriented nearly parallel to the line of sight showing at least 430 m of visible range extent, which suggests a long axis of at least 450 m, possibly up to 500 m. On December 21, the lobes were oriented broadside, both clearly visible. With a 450 m long axis, the 0.3 Hz Doppler bandwidth on the second day would be equivalent to a rotation period of 42 hr or less depending on the subradar latitude. A rotation period of tens of hours is consistent with the observed change in orientation within 1 hr of imaging data, during which the range difference between the leading edges of the lobes decreased from (112.5 ± 7.5) m to only (90.0 ± 7.5) m. Using Equation (8) with some reasonable estimates, e.g., $d_r = 130$ m, $v_r = 22.5$ m/hr, and $\phi = 60°$ would be consistent with $P = 42$ hr. The radar cross sections and the SC/OC ratio from the CW measurements were considered unreliable on 2018 December 20 due to pointing issues. On the following day, we measured $\sigma_{\mathrm{OC}} = (27{,}600 \pm 7000)\ \mathrm{m}^2$ and an SC/OC ratio of 0.23 ± 0.03. The closer lobe appears to return a more specular echo than the farther one, suggesting a possibly inhomogeneous surface. If we assume an effective diameter of 370 m (two spherical lobes 260 m across), the OC radar albedo is 0.26 and the geometric albedo is 0.43 (when H = 18.7), which would be consistent with an S- or Q-type classification. This asteroid will not make a comparable close approach to Earth until 2110 at a closer 0.057 au.

4.29. 2013 CW32

The radar images revealed 2013 CW32 to be a rounded object 220–260 m across (Figure 4, panel (l)). The echo is not fully symmetric and has features that suggest either varying topography, heterogeneous surface properties, or both. Published lightcurve-based period estimates are not available, but based on the Doppler broadening of 2.2 Hz and a diameter estimate of 240 m, the rotation period is 3 hr or less. 2013 CW32 was found to be an S-type asteroid (see footnote 20) with the SC/OC ratio of 0.44 in the higher end of the values common for S-type NEAs. The OC radar albedo is 0.23–0.31, and the geometric albedo is 0.05 assuming that $D = 240$ m and $H = 22.0$, which is very low compared to other S-type asteroids (Thomas et al. 2011). The Doppler spectrum also shows a peculiar echo enhancement from 0 Hz to 0.6 Hz (Figure 1), which is especially prominent in the SC polarization and could play a role in the relatively high SC/OC ratio for an S-type asteroid. The Doppler spectrum is averaged over only 7 minutes, so the enhancement could be caused by a specific surface feature, such as a crater with an accumulation of wavelength-scale scatterers, but confirming the cause of the scattering anomaly would require further modeling work. There is no clear source in the delay-Doppler images that could be unambiguously identified to cause it. Unfortunately, we obtained radar data for 2013 CW32 only on one day, and its next comparable close approach to Earth (at less than 0.1 au) does not take place until in 2056 at 0.039 au.

4.30. 2015 DP155

2015 DP155 was observed on four days in 2018 June. Its shape is angular (Figure 4, panel (m)), extending up to 200 m, while the volume-equivalent diameter of a preliminary shape model is 140 m according to Repp et al. (2020). The asteroid appears covered with large boulders based on the multiple visible speckles. The radar observations are consistent with a lightcurve-based rotation period of (3.097 ± 0.005) hr (Warner 2018) through Doppler broadening up to 1.5 Hz and the feature progression rate in the images. Almost one full rotation was covered on June 10–12 and just over half of a full rotation on June 9. The SC/OC ratio varied from 0.11 to 0.29 between the observation days so that 0.29 appeared only once on June 10, whereas on the other three days the SC/OC ratio remained in a more narrow range of 0.11–0.14. Values as low as these were unexpected given how visibly rough the surface appears in Figure 4, panel (m), which was obtained on one of the days with a low SC/OC-ratio measurement. All the CW observations were done at different rotation phases, so the variation could indicate a heterogeneous regolith size–frequency distribution as no systematic issues were noted. The CW measurements had a short duration, so there was little orientational averaging in each measurement. The OC radar albedo is estimated in the range of 0.26–0.30, the precise value requiring further shape derivation due to the asteroid's complex morphology. The geometric albedo based on $H = 21.6$ and diameter of 140–150 m is 0.20–0.23, which is consistent with the asteroid's Q-type taxonomy (see footnote 20). More detailed radar-observation analysis and shape modeling of 2015 DP155 is a work in progress and results will be forthcoming. This asteroid will make a comparable close approach to Earth in 2080 at a distance of 0.024 au.

4.31. 2015 JD1

The radar images of 2015 JD1 revealed a contact binary with the head about 60 m and the body about 110 m across, or approximately 200 m along the long axis (Figure 4, panel (n)). The 1 Hz Doppler broadening and the feature progression rate, as estimated based on the relative motion of the head with respect to the body in the 0.2 μs delay-Doppler images on 2019 November 2, are consistent with the 5.21 hr rotation period reported by Warner & Stephens (2020a) and Pravec et al (see footnote 19). if the subradar latitude is about 55° (the elongated body can also cause some of the variations). We measured SC/OC ratios from 1.12 to 1.55, which were consistently high over three days and some of the highest ever measured for NEAs. The LNA issue that we discussed in Section 3 could have played a part in all the SC-polarization measurements for 2015 JD1, but because of the consistency of the results, we believe it was not a major source of error. A comparison to another asteroid, 2019 UL8, which was observed on one of the same days with a common SC/OC ratio of 0.22 (see Table 2), supports the credibility of the results. The high SC/OC ratio of 2015 JD1 indicates that it is most likely an E-type asteroid (Benner et al. 2008). The new NIR-spectroscopy observations by López-Oquendo et al. (2022) are consistent with an E-type classification but also reveal rotational spectral variation with hints of B-, L-, and X-type spectra. Further, this paper presents more detailed results of the radar observations. Perna et al. (2018) reported an L-type spectrum, although the spectrum lacked the subtle features characteristic of L-type asteroids. L-type spectra are hard to distinguish from other similar types and need to be confirmed by optical polarimetric observations (Devogèle et al. 2018). Furthermore, as we report above for (153814) 2001 WN5, which is assumed to be an L-type asteroid, the radar-scattering properties were found to be comparable to S-complex asteroids with an SC/OC ratio of 0.40 ± 0.07 and the OC radar albedo estimated at 0.17. López-Oquendo et al. (2022) report also a high geometric albedo of 0.35 ± 0.12 for 2015 JD1 based on an effective diameter of 150 m, consistent with E-type asteroids. Using the maximum $\sigma_{OC} = 4740$ m^2 and an effective diameter of 150 m, we estimate the OC radar albedo to be up to 0.27. The next comparable close approach to Earth by 2015 JD1 will be in 2058 at 0.034 au.

4.32. 2016 AZ8

As preliminarily reported by Virkki et al. (2019), 2016 AZ8 is a binary asteroid system that has a rounded primary with a diameter of at least 400 m based on a visible extent of 200 m and a secondary that is at least 110 m across based on a visible extent of 50–60 m (Figure 4, panel (o)). This diameter estimate is inconsistent with, and effectively rules out, the NEOWISE team's diameter estimate of (215 ± 52) m (Masiero et al. 2017). The system separation along the line of sight was 380–440 m and during the 34 minute track, the separation narrowed by 30–38 m and the Doppler shift of the secondary increased by 0.15 Hz; however, the narrowing could have been an observational bias caused by elongation of the primary. If we assume an equatorial view and diameter estimates of 400–480 m and 110–150 m, the rotation periods of the primary and secondary would be constrained to below 5.8–7.3 hr and 16–22 hr, respectively, based on the maximum Doppler bandwidths of 1.9 Hz and 0.19 Hz observed in the delay-Doppler images and Equation (1). Pravec et al. reported a period estimate of 3.9 hr, which would require a subradar latitude of at least $\sim 48°$ for a 400 m or larger primary. Warner & Stephens (2019b) reported a primary period of 16.897 hr and a secondary period of 13.548 hr. The primary's period of 16.897 hr would require its diameter to be at least 1150 m to be consistent with the observed Doppler broadening, and the secondary to be at least 93 m across (or 140 m if the subradar latitude were 48°). The subradar latitude was likely decreasing through January, because the periodic occultation is clear in the lightcurves obtained later in 2019 January when the subradar latitude was likely close to the mutual-orbit plane. All the CW measurements suffered from pointing and focusing issues, so all the radar cross sections from the CW measurements should be considered underestimated (imaging did not suffer from the same issues). Using a diameter estimate of 400 m, an $H = 21.1$, and the maximum observed OC radar cross section of 1780 m^2 rounded up to 2000 m^2, we find a low geometric albedo of 4% and a very low radar albedo of only 2%, both of which are consistent with the C-type classification (see footnote 20) and suggest a very porous near-surface. Both albedos are lower than what has been observed for B-type asteroids (3200) Phaethon (Taylor et al. 2019a) and (101955) Bennu (Nolan et al. 2013). Instead, the radar albedo is comparable to those observed for comets (Harmon et al. 2004) raising a possibility of cometary origin. Although the radar albedo could be underestimated by a factor of 2 or so, the albedos are consistent with the lower end of possible diameters. Assuming a much greater diameter would require unparalleled, possibly unphysically low geometric albedo. The SC/OC ratio is estimated at 0.16, which is common for C-type asteroids such as 2016 AZ8, but also has an uncertainty of at least 20%. The next close approach by 2016 AZ8 within 0.1 au of Earth will occur in 2053 at 0.095 au. It will not make a close approach comparable to the 2019 apparition until 2151 at 0.033 au.

4.33. 2017 VR12

Two days of radar observations of 2017 VR12 on 2018 March 6–7 showed a lumpy, slightly elongated asteroid at least 180 m across the long axis (Figure 4, panel (p)). The observed Doppler broadening ranged from 2.4 Hz to 3.4 Hz on March 6 and from 2.8 Hz to 4.0 Hz on March 7, depending on the orientation. This suggests a long-to-intermediate-axis ratio of $\sim$1.4. The sky motion of about 20° per day accounts for up to 0.25 Hz of the difference between the two days. The greater values on 2018 March 7 indicate that the subradar latitude was closer to the asteroid's equator on March 7 than on March 6.

The Doppler broadening and the size estimate are consistent with the period estimate of about 1.378 hr by Bondarenko et al. (2019); Devyatkin et al. (2020), and Pravec et al (see footnote 19). The observed visible range extent was up to 157 m, which is consistent with a long axis of about 200 m estimated using the maximum Doppler broadening of 4 Hz and the period above. We estimate the maximum visible extent to cover about 80% of the long axis because of the elongation. Using the axis ratio of 1.4 gives an intermediate-axis length of ∼140 m and an effective diameter of 170 m. Bondarenko et al. (2019) used bistatic radar observations on 2018 March 5, using Goldstone's DSS-14 telescope's X-band (8.56 GHz, 3.5 cm) radar to transmit and 32-m radio telescopes in Zelenchukskaya and Badary Observatories to receive. They reported a diameter of (138 ± 14) m with SC/OC ratios of 0.31–0.32 and radar albedos of 0.34–0.36. Their size estimate is slightly less than what we found for the longest axis, possibly due to a greater subradar latitude during the observation considering that there was a decl. difference of 15° between March 5 and 6. Their 10 Hz Doppler-bandwidth observation using the X-band radar is consistent with a 170 m sphere observed at a subradar latitude of 35°. The scattering properties are comparable (slightly above) to those we found using Arecibo's S-band radar system: SC/OC ratio of 0.18–0.25, and $\hat{\sigma}_{OC} \approx 0.27$ (a difference in the radar albedo was expected based on different size estimates). The geometric albedo is 0.35, when $D = 170$ m and $H = 20.6$. Devogèle et al. (2019) reported that the target is likely a V type. The high geometric albedo is consistent with a V-type classification; however, the observed SC/OC ratio range is more typical for an S-type asteroid than other V types (Benner et al. 2008). This asteroid will make a much more distant flyby of Earth in 2026 at 0.054 au and will not make a close approach comparable to the 2018 apparition until 2079 at 0.012 au.

4.34. 2017 YE5

2017 YE5 was observed monostatically at Arecibo and also in collaboration with the Green Bank Observatory and the Goldstone Solar System Radar as it passed by Earth within 16 lunar distances on 2018 June 21, but only the Arecibo monostatic observations are reported here. These collaborative radar observations revealed 2017 YE5 to be a rare "equal-mass" binary asteroid with each lobe preliminarily reported to be about 900 m in their longest dimension and orbiting each other once every ∼24 hr at least 1.8 km (four radii) apart (Taylor et al. 2018, 2019b). 2017 YE5 is only the fourth "equal-mass" binary system to be discovered among the NEA population (the others are (69230) Hermes, 1994 CJ1, and (190166) 2005 UP156). All four have been characterized by the Arecibo radar (Taylor et al. 2014, 2019b). Table 2 lists the combined bandwidths and radar cross sections for the system. On 2018 June 23, the two lobes overlapped in the Doppler-frequency dimension; however, on 2018 June 26, the two lobes were distinct enough in the Doppler-frequency dimension (Figure 4, panel (q)) that we could measure the radar cross sections and Doppler bandwidth separately for each component. For the component α, we observed $\sigma_{OC} = (0.23 \pm 0.06)$ km^2 and $B = 0.7$ Hz, whereas, for the component β, we observed $\sigma_{OC} = (0.18 \pm 0.05)$ km^2 and $B = 0.6$ Hz. Although the difference in the radar cross sections is within the uncertainty limits, the square root of the ratio of the radar cross sections of the two lobes (1.13) and the ratio of the Doppler bandwidths (1.17) suggests that the effective diameter of component α could be 10%–20% larger than that of component β. Using these radar cross sections, a 900 m diameter for the component α, and an 800 m diameter for the component β sets the OC radar albedo to 0.36 ± 0.10 for both components. The difference in the SC/OC ratios is within the uncertainty limits: 0.32 ± 0.02 (α) and 0.30 ± 0.02 (β). Monteiro et al. (2021) reported a very low geometric albedo of 0.03, which is consistent with an effective diameter of ∼1200 m, or two components with sizes of ∼900 m and ∼800 m, when $H = 19.2$. This low albedo and its heliocentric orbit with a high eccentricity of 0.71 have led to the suggestion that 2017 YE5 may be a dormant Jupiter-family comet that exhibits a D-type spectrum (Monteiro et al. 2021). This classification would place 2017 YE5 as one of the only D-type NEAs observed using radar, if not the only one. The radar albedo of 0.36 is a lot greater than the average radar albedos for comets (up to 0.1 according to Harmon et al. 2004) and an extinct comet (3200) Phaethon (0.1 according to Taylor et al. 2019a) and also significantly greater than the average OC radar albedos of other C-complex asteroids as we discuss in Section 5. The observed radar cross section could be increased to some extent by double scattering between the two components, but it is unlikely to be the only factor. High radar albedos are typically linked to high near-surface density (Shepard et al. 2015) and/or an intermediate abundance of metals, but here it seems inconsistent with the very low bulk density of <1 g cm^{-3} estimated by Taylor et al. (2019b). A more likely explanation for an object originating from the outer Main Belt or beyond could be a large abundance of subsurface water ice. Water ice in large quantities is known to enhance both the SC/OC ratios and the radar albedos, as the radar observations of the icy Galilean moons (Ostro et al. 1992) and the permanently shadowed polar craters of Mercury (Harmon et al. 2001) have shown. This could suggest a possible increase in surface activity close to the perihelion at 0.82 au, and it could have been a factor in the evolution of this asteroid becoming an equal-mass binary. This close approach at 0.04 au was the closest flyby of Earth (and the only one less than 0.1 au) by 2017 YE5 for more than 150 years into the future.

4.35. 2018 EJ4

The delay-Doppler images of 2018 EJ4 show a rounded but not fully featureless object with a visible extent of 80–90 m (Figure 4, panel (r)). The observed Doppler bandwidth is (1.0 ± 0.1) Hz and, based on lightcurves, the rotation period is 7.48 hr (Warner 2018) or 3.74 hr (Benishek 2018). Using Equation (1), the diameter would have to be greater than about 130 m to be consistent with $P = 3.74$ hr, or greater than about 270 m to be consistent with $P = 7.48$ hr. The images are not precise enough to allow feature tracking, although a mix of specular and diffusely scattering features can be observed in individual images. Using $H = 21.4$, $\sigma_{OC} \approx 1300$ m^2, either 270 m or 130 m as the diameter, the geometric albedo is 0.07 or 0.29, and the OC radar albedo is 0.02 or 0.10, respectively. Neither radar albedo is unexpected for C-type asteroids such as 2018 EJ4 (see footnote 20), but the geometric albedos would suggest that the size could be up to 270 m because 0.07 is closer to the C-class average geometric albedo (Clark et al. 2004; Thomas et al. 2011). A specular leading edge could cause the visible extent to appear only through two-thirds of the illuminated hemisphere. A radar albedo of 0.02 would however be exceptionally low. The SC/OC ratio was observed at

0.30 ± 0.02, which is consistent with the taxonomic classification (Benner et al. 2008), but interestingly in the high end for an object with a specular leading edge as it appears for 2018 EJ4. This asteroid will make a more distant flyby of Earth in 2049 at 0.045 au and will not make a comparable flyby of Earth until 2197 at 0.012 au.

4.36. 2019 FU

One day of radar observations showed that 2019 FU is approximately 160–200 m across based on the visible range extent, and its shape is relatively rounded but with several angular features visible as the asteroid rotates (Figure 4, panel (s)). For example, there was an anomalously bright feature, a specular reflection from a flat facet that approximately doubled the S/N compared to the other observed sides, moving through the leading edge from about 23:12 to 23:15 UT on 2019 April 8. The Doppler bandwidth of 7.6 Hz suggests a rotation period of up to 39 minutes assuming $D = 180$ m; however, the spin rate could be even faster based on the quick progression of the features through the illuminated hemisphere, placing 2019 FU among the fast rotators. No lightcurves are available. Using a diameter estimate of 180 m gives a very low geometric albedo of only 0.03 (assuming $H = 23.2$) and also a very low OC radar albedo of 0.06, which indicates a dark and porous surface comparable to that of (3200) Phaethon (Taylor et al. 2019a). The SC/OC ratio of 0.27 is common for S- and C-complex NEAs; however, the albedos effectively rule out the S complex. There are no comparable Earth approaches by 2019 FU known over the next four centuries. In 2041, this asteroid will fly by Earth at 0.079 au, almost six times farther away than in 2019.

4.37. 2019 RC

One day of radar imaging revealed a complex-shaped object with a visible range extent of about 60 m (Figure 4, panel (t)). The lightcurves suggest a spin period of 9.73 hr (Warner & Stephens 2020a), which constrains the lower limit of the diameter to 100 m using Equation (1) and the observed Doppler broadening of 0.3 Hz. The shape is complex due to a small lobe at the leading edge, which appears in the first half of the high-resolution imaging but moves out of the view as the asteroid rotates. Bifurcation is not evidently clear but cannot be ruled out either. The extraordinarily high SC/OC ratio of 1.30 ± 0.07 suggests that 2019 RC could be an E-type NEA. The value is consistently high in every CW and imaging scan. The OC radar albedo is estimated 0.37 assuming a radar cross section of (5700 ± 1400) m^2 and a diameter of 140 m. This is a quite high radar albedo indicating a dense near-surface and possible metal richness, but it has a high uncertainty due to the complex shape. The geometric albedo is estimated at 0.17 (when $H = 21.8$), which is low relative to other E-type asteroids (Thomas et al. 2011); however, the absolute magnitude could be underestimated due to the phase-curve fit using only phase angles of 45°–83°. When photometric observations with small phase angles (<10°) have not been possible, the phase slope cannot be well constrained but is assumed to be 0.15. This has been found to cause misestimation of the absolute magnitude and, consequently, of the geometric albedo of high-albedo asteroids, which exhibit stronger opposition surges than low-albedo asteroids (Muinonen et al. 2010). The next close approach to Earth by 2019 RC will occur in 2107 at 0.075 au with no flybys closer than that in 2019 for the next four centuries.

5. Conclusions

In the time period from 2017 December through 2019 December, we detected 191 unique near-Earth asteroids with CW radar observations and obtained high-resolution (75 m or finer) delay-Doppler images of 75 NEAs, of which 41 were well resolved and had a maximum visible range extent greater than 60 m. Of these, we selected 37 NEAs for more detailed analysis, including size, spin, and radar albedo constraints. Delay-Doppler images are the only Earth-based asteroid imaging method that can reveal 10 m scale surface features and are therefore an invaluable tool for revealing the diversity of asteroid shapes and multiplicity (satellites) in addition to the sizes, rotation periods, and near-surface properties of individual NEAs. We also publish for the first time radar data for rare taxonomic types, such as possible (unpublished) L/Ld-type NEAs (3752) Camillo and (153814) 2001 WN5, and a D-type NEA 2017 YE5.

At least 4 out of 33 NEAs, which were found to have an effective diameter greater than 200 m, were binary asteroids (99942 Moshup, 2016 AZ8, 2018 EB (Brozovic et al. 2018), and an equal-mass binary asteroid 2017 YE5). This fraction of ∼12% is roughly consistent with earlier estimates of the fraction of binary NEAs being approximately one in six asteroids greater than 200 m (Margot et al. 2015). Some additional secondary objects could have been missed, however, due to the observation geometries or challenges caused by a low S/N or coarse resolution of the images. Typically, the secondary body rotates slower than the primary body, which causes it to appear as a spike in the Doppler spectrum, but a fast-spinning small secondary could be missed without a meticulous analysis at different frequency resolutions. We note that any secondary has to be in the size scale of at least tens of meters to be detectable even if the asteroid is relatively close (or larger if the asteroid is more distant). At least 11 (Midas, Camillo, Masaakikoyama, 2003 YE45, 2002 HK12, Agni, 2006 SF6, 2003 NW1, 2010 GT7, 2012 MS4, and 2015 JD1) out of 41 NEAs larger than 140 m (∼27%) and 10 out of 33 NEAs larger than 200 m (∼30%) were contact binaries with two distinct but connected lobes. This percentage approximately doubles the previously estimated value of 14% for the fraction of contact binaries among the NEAs greater than 200 m (Taylor et al. 2012; Benner et al. 2015). Although the sample size is small and, thus, not statistically robust, the difference is quite large and could imply that contact binaries are more common than previously assumed, and hence opens new questions on the shape evolution of asteroids.

The distribution of observed SC/OC ratios was similar to that reported by Benner et al. (2008): The mean SC/OC ratios for S-, Q-, and C + B-type NEAs with 1σ standard deviations were 0.32 ± 0.05, 0.32 ± 0.14, and 0.26 ± 0.08, respectively, while the global average was 0.37 ± 0.23 for 112 NEAs. We identified five NEAs with SC/OC ratios greater than 1.0, and thus possible E-type asteroids: (141593) 2002 HK12, (418900) 2009 BE2, 2015 JD1, 2019 QY1, and 2019 RC. Six NEAs were observed with medium-to-high SC/OC ratios between 0.65 and 0.9: (467309) 1996 AW1, (522684) 2016 JP, 2018 BT1, 2018 LK, 2019 AX5, and 2019 BG3, which could be suggestive of either V type or E type. 2019 RC, with an anomalously high SC/OC ratio greater than 1.0, had a relatively low geometric albedo (∼0.2), which conflicts with the E-type classification. However, the complex shape poses challenges in the estimation of both albedos, and having only one day of radar observations limits the constraints that can be made. Moreover, when photometric observations at small phase angles (<15°) have not been possible and the phase slope is not well constrained but assumed as $G = 0.15$, this could cause misestimation of the absolute magnitude and, consequently, of the geometric albedo (Muinonen et al. 2010).

The mean OC radar albedos for S- and Q-type NEAs with 1σ standard deviations is 0.19 ± 0.06 (11 NEAs) and for C-type NEAs 0.06 ± 0.04 (4 NEAs), respectively, while the global mean for 41 NEAs was 0.21 ± 0.11 (the medians were equal to the means with a precision of 0.02). The distribution of the OC radar albedos versus the geometric albedos is illustrated in Figure 5. The number of NEAs that are V types, X complex, or L/Ld types is too low for statistical significance, but we see both V-type NEAs at ∼0.3, radar albedos of L-type NEAs comparable to those of the S-type NEAs, and X-type NEAs either close to the average for the S-type NEAs or at the upper limit as expected for metal-rich asteroids. In contrast, Magri et al. (1999) found an average of 0.14 ± 0.04 for both S- and C-type main-belt asteroids (MBAs). B, F, G, and P classes were grouped together with the average at 0.095 ± 0.056. Although the radar albedos of S-complex NEAs appear consistent with the radar albedos of S-complex MBAs, further work and a larger sample size are required to better constrain the uncertainties and understand the connection between the visual and radar-scattering properties of asteroids and how they should be interpreted in terms of their physical properties. The large variation of the radar albedos of dark NEAs ($p_V < 0.2$) is particularly notable and requires further analysis because metallic asteroids have been traditionally limited to $0.1 < p_V < 0.3$. The highest radar albedos were estimated for 2011 WN15 and 2014 SR339, indicating possible metal-rich compositions that are generally rare in the NEA population, and thus these objects call for further analysis. We also noted that several NEAs with a low geometric albedo but a high radar albedo had inconsistent VNIR spectrum interpretations, including Ra-Shalom and 2011 HP. For example, for 2014 SR339, Xc type would be more consistent with its high radar albedo but low geometric albedo when comparing its radar-scattering properties to those of other B- and Xc-type asteroids. In the bigger picture of asteroid characterization, we find that radar-scattering properties—either the radar albedo, the SC/OC ratio, or both—could be used more widely as complementary information for the VNIR spectrometry to characterize the composition of asteroids because the longer wavelengths of radar systems can probe asteroid surfaces deeper than any VNIR methods.

In terms of future work, we reiterate that several NEAs presented in this paper have enough radar data that would allow dedicated publications. For example, we highlight 2017 YE5 as an object of special interest for further analysis due to its equal-mass binary nature, D-type classification, and radar-scattering properties that might suggest a significant abundance of subsurface water ice.

The authors are sincerely grateful for the Arecibo Observatory's telescope operations, electronics, and maintenance teams for making these observations possible. These Arecibo planetary radar observations were fully supported by the National Aeronautics and Space Administration's (NASA's) Near-Earth Object Observations program through grant Nos. 80NSSC18K1098 and 80NSSC19K0523 awarded to the University of Central Florida (UCF) and NNX13AQ46G awarded to Universities Space Research Association (USRA). The Arecibo Observatory is a facility of the National Science Foundation (NSF) operated under cooperative agreement by UCF, Yang Enterprises, Inc., and Universidad Ana G. Méndez.

Part of the data utilized in this publication were obtained and made available by the MIT-Hawaii Near-Earth Object Spectroscopic Survey (MITHNEOS). The IRTF is operated by the University of Hawaii under cooperative agreement No. NCC 5-538 with the NASA Office of Space Science, Planetary Astronomy Program. The MITHNEOS is supported by NASA grant 09-NEOO009-0001 and by the NSF under grant Nos. 0506716 and 0907766. This work also uses data obtained from the Asteroid Lightcurve Data Exchange Format (ALCDEF) database, which is supported by funding from NASA grant 80NSSC18K0851, and made use of NASA's Astrophysics Data System and the Jet Propulsion Laboratory's Small-Body Database. A.V. acknowledges funding from the Academy of Finland grants 1325805 and 1345115 for a part of the work. S. M., F.V., and D.H. acknowledge funding from the Preeminent Postdoctoral Program of the University of Central Florida. R. M., B.P., and D.R. were supported by the Arecibo Observatory Research Experience for Undergraduates program, National Science Foundation grant 1559849.

The CW echo-power spectra for all NEAs presented in this paper are being uploaded to the Small Bodies Node of the Planetary Data System, and the delay-Doppler images are available in FITS format through Figshare (Virkki et al. 2022).

Facility: Arecibo Observatory .

Appendix A
Doppler-echo-power Spectra

Figure 6 includes the echo-power spectra of 35 of the 37 NEAs selected for further analysis in Section 4. The other two, of Camillo and 2013 CW32, are displayed in Figure 1. The displayed spectra were smoothed using a visually pleasing frequency resolution as described in Section 3, and the time stamp of the midreceive time is shown for each asteroid.

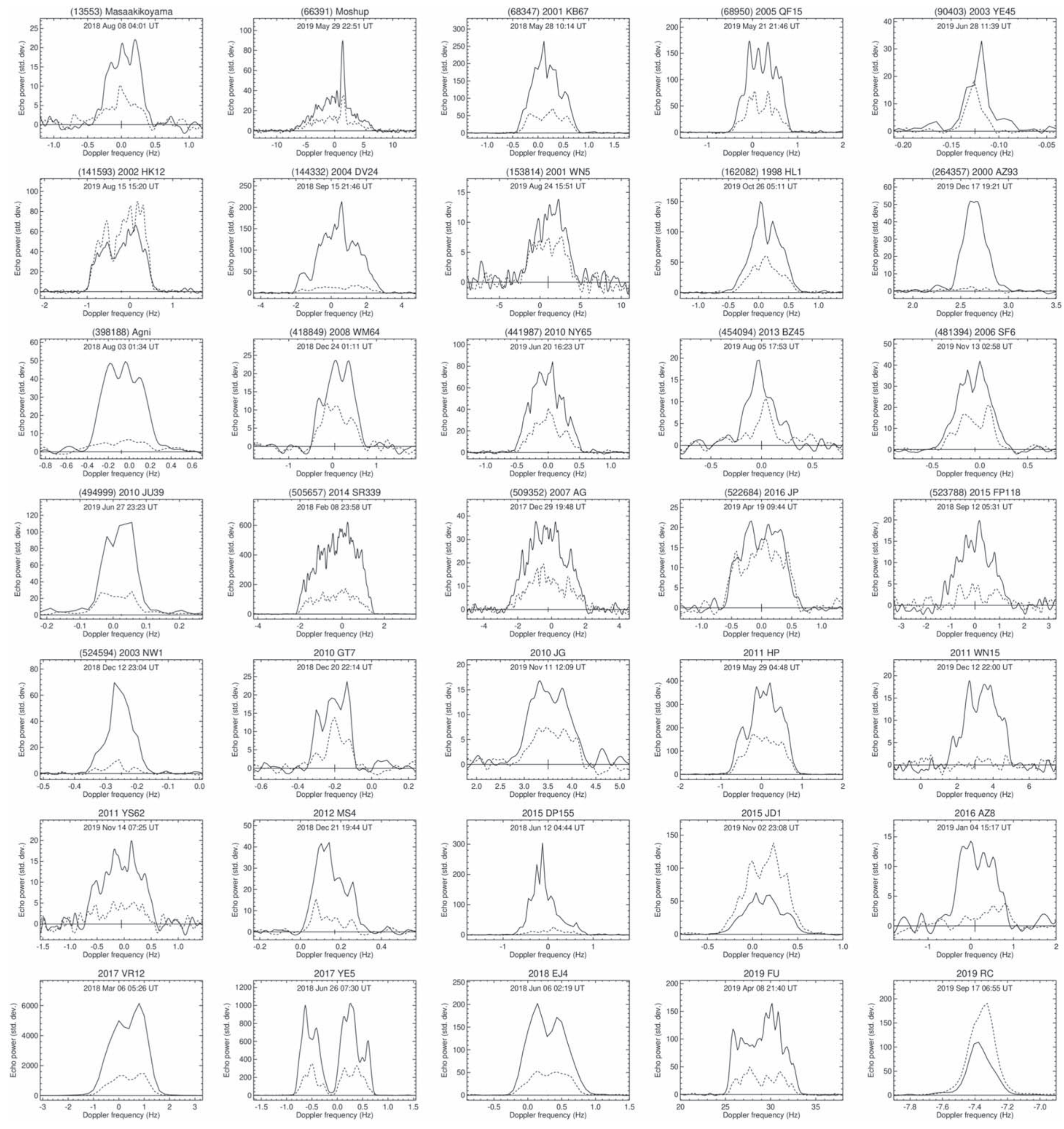

Figure 6. The echo-power spectra of 35 of the 37 NEAs selected for further analysis with the Doppler-frequency offset from the expected Doppler frequency on the horizontal axis and the z-scores of the echo power on the vertical axis. The solid line depicts the echo-power spectra in the OC polarization and the dashed line in the SC polarization. The time stamp depicts the midreceive time in UT to a precision of a minute.

Appendix B
Telescope's System Temperatures and Antenna Gains

Figure 7 illustrates the system temperatures for the two receiver channels and the decrease of the antenna gain due to the distortion of the primary reflector after Hurricane Maria through the time period included in this paper. For the system temperatures, channel 1 (labeled "CH1") was used for the OC polarization and channel 2 (labeled "CH2") for the SC polarization until 2019 November, after which they were swapped to optimize the performance in the OC polarization. The first observation that took place after the channel swap was on 2019 December 6; all SC/OC ratios since were deemed unreliable. The vertical spikes both upward and downward were bad data. The antenna gain is plotted as a function of the zenith angle at six different azimuth angles at constant intervals

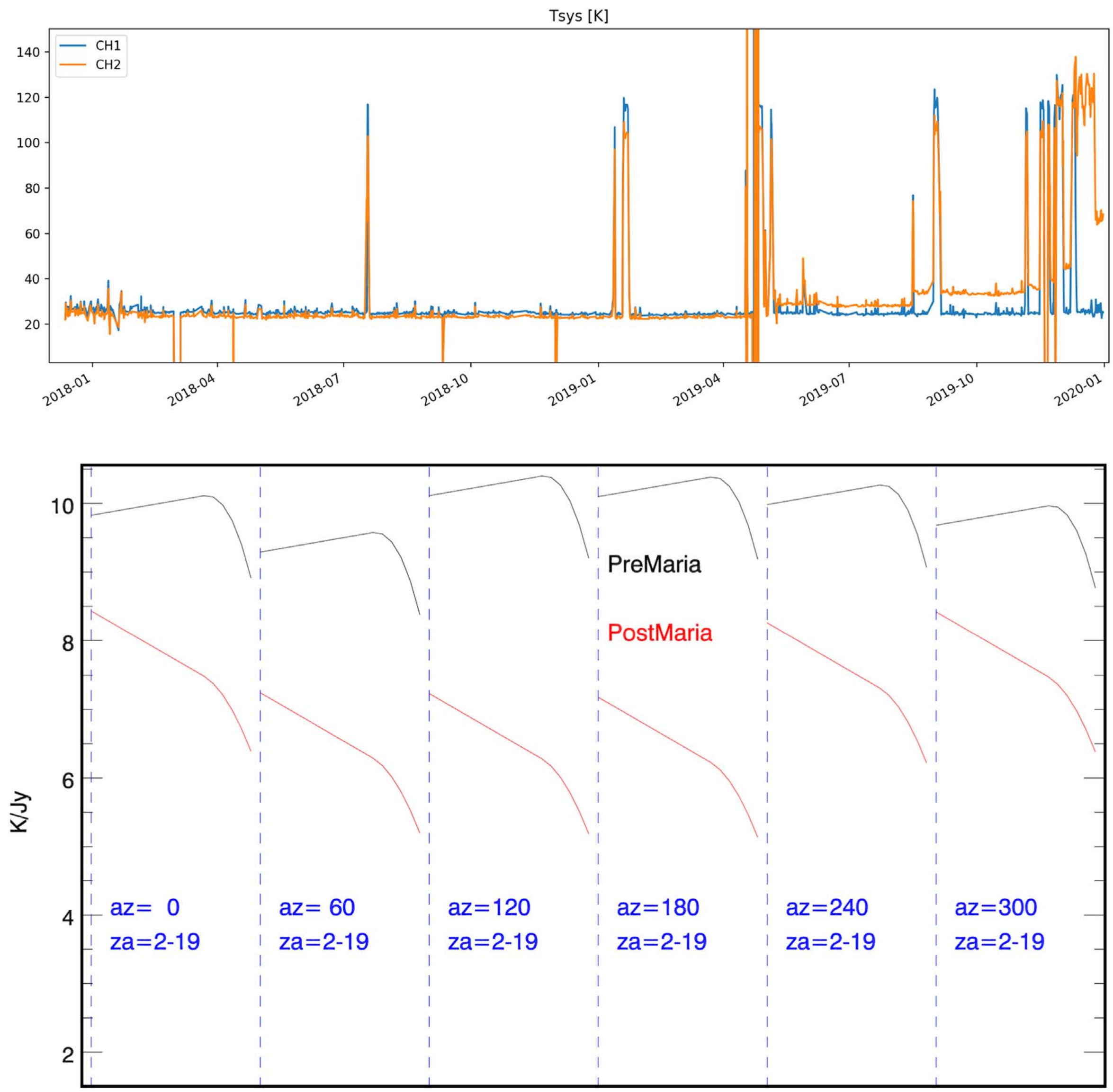

Figure 7. On the top: the system temperature of the two polarization channels from 2017 December through 2019 December. The values less than 10 K were invalid measurements due to temporary failures. Data source: http://www.naic.edu/~phil/tsys/tsysmon/tsysmon.html. On the bottom: the antenna gain using the S-band narrow (2380 MHz) receiver as a function of zenith angle ("za"; in degrees) and azimuth angle ("az"; in degrees) before Hurricane Maria on 2017 September 20 ("PreMaria"; black solid lines) and after it ("PostMaria"; red solid lines). The latter applies to all observations presented in this paper, whereas the first one is included to represent the expected change in the S/N due to the antenna gain, when comparing observations conducted before and after 2017 September 20. Data source: http://www.naic.edu/~phil/calsbn/sbn.html.

of 60°. These "post-Maria" gain curves are taken into account in the processing of the Doppler-echo-power spectra.

Appendix C Tables

Table 2 presents the results of the CW observations, including the Doppler bandwidths, radar cross sections, and SC/OC ratios. Table 3 includes results from the CW observations as well, but only includes less reliable measurements due to low-frequency resolution or systematic issues. Table 4 presents results from the delay-Doppler imaging for the 37 NEAs that were selected for further analysis, including the maximum visible range extent and Doppler bandwidth for individual observations.

Table 2
Continuous-wave Observations of Targets That Were Clearly Resolved in Frequency

Asteroid Number	Name or Designation	Start Date and Time (UT)	Duration Δt	d (au)	B (Hz)	σ_{OC} (m^2)	$\Delta\sigma_{OC}$ (m^2)	S/N_{OC}	σ_{SC} (m^2)	$\Delta\sigma_{SC}$ (m^2)	S/N_{SC}	μ_C	$\Delta\mu_C$
433	Eros	2019 Jan 26 00:03	0^h24^m	0.214	144	4.9E7	1.2E7	165	1.19E7	3.0E6	41	0.24	0.01
433	Eros	2019 Jan 27 00:10	0^h50^m	0.215	138	4.6E7	1.1E7	251	9.8E6	2.5E6	54	0.21	0.01
433	Eros	2019 Jan 28 00:45	0^h36^m	0.216	83.9	3.24E7	8.1E6	163	9.4E6	2.4E6	48	0.29	0.02
433	Eros	2019 Jan 29 00:48	0^h22^m	0.217	76.0	3.08E7	7.7E6	124	9.2E6	2.3E6	38	0.30	0.02
433	Eros	2019 Jan 30 00:09	0^h22^m	0.219	85.7	3.01E7	7.5E6	138	8.2E6	2.1E6	38	0.27	0.02
433	Eros	2019 Jan 30 23:38	0^h37^m	0.220	91.2	2.49E7	6.2E6	132	8.3E6	2.1E6	44	0.33	0.02
433	Eros	2019 Jan 31 23:36	0^h22^m	0.222	85.3	3.24E7	8.1E6	114	8.9E6	2.2E6	32	0.27	0.02
1627	Ivar	2018 Jul 05 23:12	0^h54^m	0.322	44.7	2.13E6	6.9E5	4.8	N/A	N/A	N/A	N/A	N/A
1627	Ivar	2018 Jul 07 23:19	0^h42^m	0.319	39.8	3.41E6	9.6E5	7.9	1.38E6	5.5E5	3.2	0.41	0.14
1627	Ivar	2018 Jul 11 23:13	0^h21^m	0.313	38.5	3.8E6	1.2E6	5.8	N/A	N/A	N/A	N/A	N/A
1981	Midas	2018 Mar 21 22:16	0^h09^m	0.090	17.7	8.6E5	2.2E5	87	7.4E5	1.8E5	81	0.85	0.05
1981	Midas	2018 Mar 22 21:20	0^h21^m	0.091	17.1	8.5E5	2.1E5	209	6.9E5	1.7E5	182	0.81	0.04
1981	Midas	2018 Mar 22 21:46	0^h03^m	0.091	17.0	7.0E5	1.8E5	78	5.5E5	1.4E5	66	0.79	0.04
1981	Midas	2018 Mar 23 20:51	0^h27^m	0.095	16.1	8.3E5	2.1E5	222	6.8E5	1.7E5	197	0.83	0.04
1981	Midas	2018 Mar 24 20:27	0^h27^m	0.100	15.7	1.37E6	3.4E5	273	1.15E6	2.9E5	249	0.84	0.04
1981	Midas	2018 Mar 25 20:18	0^h30^m	0.108	14.5	1.14E6	2.8E5	225	9.1E5	2.3E5	194	0.80	0.04
2061	Anza	2018 Aug 15 06:49	2^h25^m	0.207	2.9	1.40E5	3.8E4	9.8	7.1E4	2.3E4	4.9	0.51	0.12
2100	Ra-Shalom	2019 Sep 06 06:48	0^h14^m	0.215	4.3	1.15E6	3.0E5	13	4.1E5	1.2E5	6.9	0.36	0.06
2100	Ra-Shalom	2019 Sep 08 06:07	0^h21^m	0.207	3.7	7.5E5	2.0E5	14	2.95E5	8.2E4	7.9	0.39	0.06
2100	Ra-Shalom	2019 Sep 09 05:47	1^h08^m	0.204	3.5	8.8E5	2.2E5	31	2.95E5	7.6E4	15	0.33	0.03
3200	Phaethon	2017 Dec 15 23:34	0^h12^m	0.071	44.8	1.98E6	4.9E5	290	4.0E5	1.0E5	98	0.20	0.01
3200	Phaethon	2017 Dec 16 22:01	0^h11^m	0.069	47.9	1.96E6	4.9E5	36	3.53E5	8.9E4	32	0.18	0.01
3200	Phaethon	2017 Dec 17 21:01	0^h12^m	0.071	46.6	2.03E6	5.1E5	319	3.84E5	9.6E4	124	0.19	0.01
3200	Phaethon	2017 Dec 18 21:30	0^h13^m	0.078	43.3	1.56E6	3.9E5	325	2.94E5	7.4E4	121	0.19	0.01
3200	Phaethon	2017 Dec 19 20:25	0^h14^m	0.087	46.4	2.05E6	5.1E5	282	3.65E5	9.1E4	70	0.18	0.01
3752	Camillo	2018 Feb 20 23:56	0^h14^m	0.139	2.7	1.36E6	3.4E5	81	3.51E5	8.8E4	36	0.26	0.02
3752	Camillo	2018 Feb 21 23:16	0^h14^m	0.142	2.2	1.55E6	3.9E5	81	3.69E5	9.3E4	40	0.24	0.01
3752	Camillo	2018 Feb 22 23:00	0^h35^m	0.147	N/A	9.1E5	2.3E5	54	2.24E5	5.8E4	14	0.25	0.02
10145	1994 CK1	2019 Jul 17 16:34	0^h14^m	0.141	0.64	1.38E5	3.5E4	16	2.52E4	7.6E3	5.9	0.18	0.03
11500	Tomaiyowit	2019 Jun 21 20:58	0^h50^m	0.187	0.15	7.0E4	2.0E4	7.4	N/A	N/A	N/A	N/A	N/A
12538	1998 OH	2019 May 14 20:33	1^h24^m	0.187	21.5	6.3E5	1.7E5	10	1.88E5	6.9E4	3.7	0.30	0.09
13553	Masaakikoyama	2018 Jul 11 04:19	0^h21^m	0.210	0.74	9.3E5	2.3E5	37	3.24E5	8.3E4	16	0.35	0.03
13553	Masaakikoyama	2018 Aug 08 03:48	0^h20^m	0.204	0.83	7.8E5	2.0E5	31	2.69E5	7.1E4	12	0.34	0.03
13553	Masaakikoyama	2018 Aug 15 03:47	0^h21^m	0.212	0.74	7.1E5	1.8E5	32	2.39E5	6.3E4	12	0.34	0.04
66146	1998 TU3	2019 Aug 05 15:12	0^h46^m	0.174	26.7	3.34E5	9.0E4	9.7	N/A	N/A	N/A	N/A	N/A
66146	1998 TU3	2019 Aug 06 15:10	1^h39^m	0.166	38.1	5.5E5	1.4E5	16	1.31E5	4.3E4	4.6	0.24	0.05
66391	Moshup	2018 May 25 09:08	0^h08^m	0.082	19.8	8.7E4	2.2E4	86	4.4E4	1.1E4	48	0.51	0.03
66391	Moshup	2018 May 27 06:16	0^h16^m	0.078	17.7	9.7E4	2.4E4	44	5.4E4	1.4E4	25	0.56	0.04
66391	Moshup	2018 May 29 05:08	0^h13^m	0.080	17.1	1.11E5	2.8E4	37	3.60E4	9.5E3	12	0.32	0.03
66391	Moshup	2018 May 30 04:25	0^h14^m	0.084	16.9	1.30E5	3.3E4	36	3.9E4	1.0E4	11	0.30	0.03
66391	Moshup	2018 May 31 04:00	0^h17^m	0.089	16.9	1.46E5	3.7E4	30	6.0E4	1.6E4	13	0.41	0.04
66391	Moshup	2018 Jun 01 03:40	0^h16^m	0.094	12.0	1.89E5	4.7E4	36	6.6E4	1.7E4	13	0.35	0.03
66391	Moshup	2019 May 29 22:44	0^h12^m	0.060	13.4	9.7E4	2.4E4	99	3.50E4	8.8E3	51	0.36	0.02
66391	Moshup	2019 May 31 22:28	0^h16^m	0.082	13.3	2.23E5	5.6E4	81	7.5E4	1.9E4	35	0.34	0.02
66391	Moshup	2019 Jun 01 22:29	0^h19^m	0.093	12.7	2.34E5	5.9E4	55	8.8E4	2.2E4	26	0.38	0.03
66391	Moshup	2019 Jun 02 22:59	0^h31^m	0.105	11.2	2.08E5	5.2E4	68	7.3E4	1.9E4	30	0.35	0.02
66391	Moshup	2019 Jun 03 22:31	0^h58^m	0.117	11.9	1.39E5	3.5E4	38	4.4E4	1.1E4	15	0.32	0.03
66391	Moshup	2019 Jun 04 22:31	0^h56^m	0.128	17.1	2.59E5	6.6E4	25	9.7E4	2.6E4	12	0.38	0.04
68347	2001 KB67	2018 May 25 13:04	0^h08^m	0.037	1.1	7.0E3	1.7E3	48	1.44E3	3.6E2	31	0.21	0.01
68347	2001 KB67	2018 May 27 11:18	0^h09^m	0.027	1.0	6.7E3	1.7E3	46	1.43E3	3.6E2	42	0.21	0.01
68347	2001 KB67	2018 May 28 09:59	0^h19^m	0.025	1.1	5.8E3	1.5E3	26	1.36E3	3.4E2	27	0.23	0.02
68347	2001 KB67	2018 May 29 09:04	0^h05^m	0.024	1.1	5.6E3	1.4E3	34	1.35E3	3.4E2	29	0.24	0.02
68347	2001 KB67	2018 May 30 07:57	0^h09^m	0.026	0.98	5.7E3	1.4E3	36	1.86E3	4.7E2	33	0.32	0.02
68347	2001 KB67	2018 May 31 06:55	0^h08^m	0.030	0.92	5.3E3	1.3E3	36	1.85E3	4.7E2	30	0.35	0.02
68950	2002 QF15	2019 May 20 21:10	0^h12^m	0.088	1.3	4.3E5	1.1E5	61	1.20E5	3.0E4	54	0.28	0.02
68950	2002 QF15	2019 May 21 21:41	0^h09^m	0.090	1.1	4.1E5	1.0E5	24	1.04E5	2.6E4	20	0.26	0.02
68950	2002 QF15	2019 May 22 21:30	0^h15^m	0.092	1.3	5.4E5	1.3E5	67	1.41E5	3.5E4	61	0.26	0.01
68950	2002 QF15	2019 May 23 22:37	0^h13^m	0.095	0.93	3.53E5	8.8E4	46	1.07E5	2.7E4	46	0.30	0.02
68950	2002 QF15	2019 May 24 21:58	0^h13^m	0.100	1.1	5.0E5	1.3E5	56	1.52E5	3.8E4	51	0.30	0.02
68950	2002 QF15	2019 May 26 22:27	0^h22^m	0.111	0.97	5.3E5	1.3E5	53	1.36E5	3.4E4	46	0.26	0.01
68950	2002 QF15	2019 Jun 05 01:24	0^h18^m	0.182	1.1	5.5E5	1.4E5	24	1.64E5	4.5E4	9.4	0.30	0.04
85236	1993 KH	2019 Nov 13 09:17	0^h38^m	0.104	2.4	1.39E4	4.0E3	7.4	5.5E3	1.9E3	4.2	0.40	0.11
88254	2001 FM129	2019 Mar 20 23:10	0^h26^m	0.131	0.22	3.72E4	9.5E3	21	8.0E3	2.4E3	6.0	0.21	0.04

Table 2
(Continued)

Asteroid Number	Name or Designation	Start Date and Time (UT)	Duration Δt	d (au)	B (Hz)	σ_{OC} (m^2)	$\Delta\sigma_{OC}$ (m^2)	S/N_{OC}	σ_{SC} (m^2)	$\Delta\sigma_{SC}$ (m^2)	S/N_{SC}	μ_C	$\Delta\mu_C$
90403	2003 YE45	2019 Jun 26 12:04	0^h23^m	0.136	0.06	1.25E4	3.4E3	9.5	3.1E3	1.3E3	3.1	0.25	0.08
90403	2003 YE45	2019 Jun 28 11:31	0^h13^m	0.135	0.08	2.91E4	7.6E3	13	1.01E4	2.8E3	8.3	0.35	0.05
90403	2003 YE45	2019 Jul 08 10:42	0^h19^m	0.147	0.06	3.26E4	8.5E3	13	8.0E3	2.4E3	5.8	0.25	0.05
90403	2003 YE45	2019 Jul 09 10:11	0^h10^m	0.149	0.08	2.30E4	6.8E3	6.3	N/A	N/A	N/A	N/A	N/A
96590	1998 XB	2018 Mar 29 14:03	0^h48^m	0.286	0.10	1.88E5	5.3E4	7.7	9.4E4	3.3E4	4.1	0.50	0.14
141593	2002 HK12	2019 Aug 10 16:19	0^h24^m	0.071	1.5	3.10E4	7.8E3	25	3.36E4	8.5E3	30	1.08	0.08
141593	2002 HK12	2019 Aug 11 15:56	0^h26^m	0.068	1.4	3.38E4	8.5E3	38	4.1E4	1.0E4	43	1.22	0.07
141593	2002 HK12	2019 Aug 12 15:50	0^h13^m	0.066	0.77	2.09E4	5.4E3	15	1.38E4	3.6E3	13	0.66	0.07
141593	2002 HK12	2019 Aug 14 15:26	0^h06^m	0.063	1.5	3.24E4	8.1E3	38	3.61E4	9.1E3	41	1.11	0.07
141593	2002 HK12	2019 Aug 15 15:03	0^h33^m	0.063	1.5	3.41E4	8.5E3	77	3.75E4	9.4E3	81	1.10	0.06
141593	2002 HK12	2019 Aug 16 15:40	0^h06^m	0.062	1.3	2.26E4	5.7E3	27	2.54E4	6.4E3	34	1.12	0.08
141593	2002 HK12	2019 Aug 17 14:11	0^h27^m	0.062	0.73	1.15E4	3.0E3	11	1.44E4	3.8E3	13	1.25	0.16
144332	2004 DV24	2018 Sep 13 22:26	0^h28^m	0.070	4.4	7.5E4	1.9E4	61	1.49E4	3.9E3	13	0.20	0.02
144332	2004 DV24	2018 Sep 14 22:03	0^h08^m	0.062	5.0	1.23E5	3.1E4	75	2.02E4	5.1E3	31	0.16	0.01
144332	2004 DV24	2018 Sep 15 21:40	0^h09^m	0.056	4.5	1.99E5	5.0E4	94	2.30E4	5.8E3	42	0.12	0.01
152931	2000 EA107	2019 May 04 15:05	0^h27^m	0.177	15.0	3.33E5	9.4E4	7.8	N/A	N/A	N/A	N/A	N/A
153814	2001 WN5	2019 Aug 21 16:18	0^h10^m	0.102	6.6	1.18E5	3.0E4	22	4.9E4	1.3E4	13	0.41	0.04
153814	2001 WN5	2019 Aug 22 15:54	0^h24^m	0.101	7.2	1.18E5	3.0E4	30	3.9E4	1.0E4	14	0.33	0.03
153814	2001 WN5	2019 Aug 24 15:25	0^h46^m	0.099	5.9	1.11E5	2.8E4	35	5.2E4	1.3E4	24	0.47	0.03
153814	2001 WN5	2019 Aug 25 15:27	0^h29^m	0.098	6.2	1.02E5	2.6E4	26	4.3E4	1.1E4	16	0.42	0.04
162082	1998 HL1	2019 Oct 25 03:26	0^h08^m	0.042	0.98	1.51E4	3.8E3	40	4.4E3	1.1E3	35	0.29	0.02
162082	1998 HL1	2019 Oct 26 05:00	0^h26^m	0.042	1.0	1.56E4	3.9E3	77	4.7E3	1.2E3	63	0.30	0.02
162082	1998 HL1	2019 Oct 27 05:23	0^h11^m	0.043	1.1	1.45E4	3.6E3	50	4.9E3	1.2E3	38	0.34	0.02
163899	2003 SD220	2018 Aug 25 16:34	1^h21^m	0.241	0.19	2.07E5	5.7E4	8.4	N/A	N/A	N/A	N/A	N/A
216258	2006 WH1	2019 Dec 13 04:49	0^h15^m	0.064	2.5	1.09E4	2.8E3	16	N/A	N/A	N/A	N/A	N/A
237805	2002 CF26	2019 Sep 06 04:31	0^h17^m	0.103	9.1	1.06E5	2.7E4	24	3.03E4	8.2E3	9.7	0.28	0.03
237805	2002 CF26	2019 Sep 07 05:11	0^h10^m	0.105	10.5	1.01E5	2.7E4	9.4	3.2E4	1.1E4	4.2	0.31	0.08
264357	2000 AZ93	2019 Dec 17 19:13	0^h13^m	0.057	0.34	1.00E4	2.7E3	9.9	N/A	N/A	N/A	N/A	N/A
311554	2006 BQ147	2018 Feb 21 01:09	0^h58^m	0.116	0.82	1.18E4	3.1E3	13	2.9E3	1.2E3	3.1	0.24	0.08
354030	2001 RB18	2019 Sep 27 05:25	0^h09^m	0.093	1.7	8.9E4	2.2E4	30	1.49E4	4.1E3	8.8	0.17	0.02
354030	2001 RB18	2019 Sep 28 06:02	0^h09^m	0.093	1.6	7.8E4	2.0E4	26	1.42E4	4.0E3	8.0	0.18	0.03
398188	Agni	2018 Jul 23 03:03	0^h15^m	0.089	0.34	1.35E4	3.4E3	22	3.04E3	9.1E2	6.1	0.23	0.04
398188	Agni	2018 Jul 26 02:29	0^h18^m	0.079	0.37	1.25E4	3.1E3	29	3.46E3	9.2E2	11	0.28	0.03
398188	Agni	2018 Aug 03 01:30	0^h06^m	0.062	0.62	2.37E4	6.0E3	26	3.00E3	8.3E2	8.3	0.13	0.02
418849	2008 WM64	2017 Dec 21 06:39	0^h11^m	0.041	2.1	4.4E3	1.1E3	57	1.07E3	2.7E2	20	0.25	0.02
418849	2008 WM64	2017 Dec 22 05:00	0^h25^m	0.039	1.8	1.88E3	4.7E2	77	5.2E2	1.3E2	29	0.28	0.02
418849	2008 WM64	2017 Dec 23 05:05	0^h21^m	0.040	1.7	3.53E3	8.8E2	61	9.7E2	2.5E2	21	0.28	0.02
418849	2008 WM64	2018 Dec 24 01:06	0^h07^m	0.043	1.2	3.11E3	7.9E2	28	1.47E3	3.8E2	16	0.47	0.04
418900	2009 BE2	2019 Jun 23 23:54	0^h21^m	0.104	1.1	1.15E4	3.2E3	8.4	1.25E4	3.3E3	11	1.08	0.17
420591	2012 HF31	2018 Aug 09 15:13	0^h13^m	0.089	0.10	4.9E3	1.3E3	9.3	1.31E3	4.7E2	3.9	0.27	0.08
420591	2012 HF31	2018 Aug 13 15:58	0^h34^m	0.107	0.06	9.2E3	2.4E3	13	N/A	N/A	N/A	N/A	N/A
438017	2003 YO3	2018 Jan 09 18:19	0^h28^m	0.094	4.0	1.74E4	4.5E3	17	N/A	N/A	N/A	N/A	N/A
439313	2012 VE82	2018 Jul 17 19:14	1^h08^m	0.097	1.6	4.9E3	1.5E3	6.0	N/A	N/A	N/A	N/A	N/A
441987	2010 NY65	2018 Jun 28 01:51	0^h05^m	0.033	0.68	6.7E3	1.7E3	27	2.07E3	5.2E2	24	0.31	0.02
441987	2010 NY65	2018 Jun 29 02:40	0^h04^m	0.039	0.62	6.0E3	1.5E3	20	2.40E3	6.1E2	19	0.40	0.04
441987	2010 NY65	2019 Jun 19 16:04	0^h07^m	0.042	1.0	6.3E3	1.6E3	33	1.69E3	4.3E2	22	0.27	0.02
441987	2010 NY65	2019 Jun 20 16:06	0^h31^m	0.035	1.0	6.5E3	1.6E3	53	2.03E3	5.1E2	44	0.31	0.02
441987	2010 NY65	2019 Jun 28 01:47	0^h06^m	0.031	0.57	6.4E3	1.6E3	28	2.32E3	5.9E2	25	0.36	0.03
454094	2013 BZ45	2019 Aug 02 17:51	0^h10^m	0.062	0.51	5.1E3	1.3E3	19	2.16E3	5.7E2	11	0.43	0.05
454094	2013 BZ45	2019 Aug 05 17:50	0^h05^m	0.053	0.55	4.6E3	1.2E3	16	1.53E3	4.3E2	7.8	0.34	0.05
455176	1999 VF22	2019 Feb 19 11:51	0^h14^m	0.052	2.0	2.07E4	5.2E3	60	3.9E3	1.0E3	15	0.19	0.02
455176	1999 VF22	2019 Feb 20 13:03	0^h15^m	0.049	1.9	1.89E4	4.7E3	66	4.4E3	1.1E3	24	0.23	0.02
455176	1999 VF22	2019 Feb 21 14:12	0^h12^m	0.051	1.9	1.79E4	4.5E3	56	3.58E3	9.2E2	16	0.20	0.02
465617	2009 EK1	2019 Sep 12 11:12	0^h38^m	0.063	0.54	9.4E2	2.7E2	6.7	5.0E2	1.6E2	5.1	0.53	0.14
467309	1996 AW1	2018 Jun 17 02:23	0^h04^m	0.066	0.37	4.7E3	1.2E3	12	3.13E3	8.5E2	9.3	0.67	0.10
469737	2005 NW44	2018 Jun 21 01:14	0^h15^m	0.064	1.9	1.44E4	3.9E3	9.3	N/A	N/A	N/A	N/A	N/A
481394	2006 SF6	2019 Nov 11 03:01	0^h09^m	0.054	0.88	4.3E3	1.1E3	22	1.91E3	5.1E2	11	0.44	0.05
481394	2006 SF6	2019 Nov 12 02:49	0^h17^m	0.050	0.82	5.6E3	1.4E3	42	2.43E3	6.2E2	23	0.43	0.03
481394	2006 SF6	2019 Nov 13 02:50	0^h14^m	0.047	0.71	4.9E3	1.2E3	38	1.60E3	4.0E2	25	0.32	0.02
481394	2006 SF6	2019 Nov 14 02:53	0^h07^m	0.043	0.65	5.1E3	1.3E3	29	1.37E3	3.5E2	19	0.27	0.02
481394	2006 SF6	2019 Nov 15 02:30	0^h07^m	0.040	0.75	7.5E3	1.9E3	32	1.66E3	4.2E2	21	0.22	0.02
494999	2010 JU39	2019 Jun 27 02:30	0^h06^m	0.063	0.11	5.0E3	1.3E3	10	1.39E3	4.4E2	5.3	0.28	0.06
494999	2010 JU39	2019 Jun 27 23:16	0^h12^m	0.061	0.15	1.45E4	3.7E3	21	3.31E3	8.4E2	19	0.23	0.02

Table 2
(Continued)

Asteroid Number	Name or Designation	Start Date and Time (UT)	Duration Δt	d (au)	B (Hz)	σ_{OC} (m^2)	$\Delta\sigma_{OC}$ (m^2)	S/N_{OC}	σ_{SC} (m^2)	$\Delta\sigma_{SC}$ (m^2)	S/N_{SC}	μ_C	$\Delta\mu_C$
494999	2010 JU39	2019 Jun 28 22:31	0^h15^m	0.060	0.15	8.6E3	2.2E3	14	3.73E3	9.7E2	15	0.43	0.05
505657	2014 SR339	2018 Feb 08 23:47	0^h18^m	0.055	3.4	4.1E5	1.0E5	132	1.07E5	2.7E4	129	0.26	0.01
509352	2007 AG	2017 Dec 12 16:19	0^h10^m	0.100	2.5	5.4E4	1.4E4	23	1.17E4	3.7E3	5.2	0.22	0.04
509352	2007 AG	2017 Dec 22 17:34	0^h19^m	0.063	3.3	4.3E4	1.1E4	66	1.45E4	3.7E3	32	0.34	0.02
509352	2007 AG	2017 Dec 26 18:34	0^h14^m	0.058	4.1	4.5E4	1.1E4	70	1.45E4	3.7E3	31	0.32	0.02
509352	2007 AG	2017 Dec 28 19:10	0^h24^m	0.059	3.9	4.1E4	1.0E4	25	1.32E4	3.4E3	15	0.32	0.03
509352	2007 AG	2017 Dec 29 19:42	0^h10^m	0.061	4.5	4.1E4	1.0E4	74	1.74E4	4.4E3	41	0.42	0.02
509352	2007 AG	2018 Jan 03 20:28	0^h17^m	0.073	4.8	3.76E4	9.5E3	25	1.46E4	3.9E3	11	0.39	0.04
509935	2009 QL8	2017 Dec 29 10:54	0^h33^m	0.123	0.72	1.18E4	3.2E3	9.3	N/A	N/A	N/A	N/A	N/A
522684	2016 JP	2019 Apr 16 11:19	0^h18^m	0.053	1.3	3.69E3	9.3E2	34	2.70E3	6.8E2	26	0.73	0.05
522684	2016 JP	2019 Apr 17 10:42	0^h21^m	0.050	1.0	1.19E3	3.0E2	17	1.20E3	3.1E2	17	1.01	0.10
522684	2016 JP	2019 Apr 18 11:23	0^h12^m	0.049	1.1	1.71E3	4.3E2	26	1.42E3	3.6E2	22	0.83	0.06
522684	2016 JP	2019 Apr 19 09:34	0^h16^m	0.049	1.2	3.74E3	9.4E2	38	2.95E3	7.4E2	32	0.79	0.05
522684	2016 JP	2019 Apr 20 08:59	0^h08^m	0.049	1.2	3.82E3	9.7E2	22	2.95E3	7.6E2	18	0.77	0.07
522684	2016 JP	2019 Apr 21 08:30	0^h08^m	0.050	1.00	3.21E3	8.2E2	20	2.53E3	6.5E2	17	0.79	0.07
522684	2016 JP	2019 Apr 22 10:19	0^h10^m	0.052	1.1	3.77E3	9.7E2	17	2.07E3	5.6E2	9.5	0.55	0.07
523788	2015 FP118	2018 Aug 24 18:51	0^h19^m	0.063	2.4	1.11E4	2.8E3	33	3.16E3	8.5E2	10	0.29	0.03
523788	2015 FP118	2018 Aug 26 19:06	0^h09^m	0.053	2.1	1.36E4	3.5E3	24	2.26E3	7.2E2	5.2	0.17	0.03
523788	2015 FP118	2018 Sep 12 05:23	0^h14^m	0.059	2.6	1.60E4	4.0E3	34	3.34E3	9.4E2	7.7	0.21	0.03
523788	2015 FP118	2018 Sep 13 05:08	0^h19^m	0.063	2.4	1.42E4	3.6E3	35	3.20E3	8.9E2	8.4	0.23	0.03
523788	2015 FP118	2018 Sep 14 06:04	0^h07^m	0.069	2.8	1.02E4	2.7E3	12	4.1E3	1.3E3	4.8	0.40	0.09
524594	2003 NW1	2018 Dec 12 23:00	0^h07^m	0.073	0.17	2.22E4	5.7E3	17	2.62E3	7.3E2	7.9	0.12	0.02
525364	2005 CL7	2019 Aug 09 16:38	0^h37^m	0.069	3.4	1.05E4	2.7E3	16	2.72E3	8.7E2	4.9	0.26	0.06
525364	2005 CL7	2019 Aug 10 17:08	0^h07^m	0.068	2.4	1.27E4	3.3E3	17	2.45E3	8.5E2	4.1	0.19	0.05
525477	2005 FC3	2019 Mar 16 04:08	0^h25^m	0.106	0.07	4.5E3	1.3E3	8.0	2.33E3	7.9E2	4.4	0.52	0.14
528159	2008 HS3	2019 May 15 05:15	0^h07^m	0.041	0.32	1.60E3	4.1E2	20	3.13E2	8.6E1	8.8	0.20	0.03
528159	2008 HS3	2019 May 16 05:27	0^h04^m	0.042	0.35	1.97E3	5.1E2	16	4.9E2	1.3E2	10	0.25	0.03
528159	2008 HS3	2019 May 17 06:11	0^h03^m	0.044	0.40	1.65E3	4.3E2	14	5.5E2	1.5E2	9.1	0.34	0.05
531277	2012 MM11	2018 Dec 05 09:42	0^h15^m	0.092	0.40	1.07E4	2.8E3	15	2.30E3	8.7E2	3.6	0.22	0.06
533541	2014 JU54	2018 Dec 18 05:37	0^h26^m	0.087	0.28	4.9E3	1.3E3	15	1.44E3	4.8E2	4.6	0.29	0.07
537342	2015 KN120	2019 Sep 27 23:03	1^h50^m	0.113	2.5	9.0E3	2.8E3	5.6	N/A	N/A	N/A	N/A	N/A
	1999 FN19	2018 May 29 08:02	0^h29^m	0.074	0.14	1.22E3	3.5E2	6.9	8.1E2	2.7E2	4.7	0.67	0.18
	2005 WD	2019 Nov 11 00:08	0^h28^m	0.061	1.8	1.64E3	4.6E2	7.6	N/A	N/A	N/A	N/A	N/A
	2006 WE4	2018 Jan 19 16:06	0^h55^m	0.127	3.0	4.0E4	1.0E4	15	N/A	N/A	N/A	N/A	N/A
	2006 WE4	2018 Jan 23 15:37	0^h39^m	0.113	3.1	3.12E4	8.0E3	16	6.6E3	2.6E3	3.3	0.21	0.07
	2009 FU23	2019 May 11 11:05	0^h12^m	0.071	0.64	7.3E3	1.9E3	18	1.37E3	4.4E2	4.8	0.19	0.04
	2010 GT7	2018 Dec 20 22:10	0^h07^m	0.068	0.20	7.1E3	1.8E3	17	3.14E3	8.3E2	12	0.44	0.05
	2010 GT7	2018 Dec 21 21:15	0^h06^m	0.066	0.18	8.2E3	2.1E3	16	2.69E3	7.1E2	13	0.33	0.04
	2010 JG	2019 Nov 11 11:55	0^h24^m	0.051	1.5	2.65E3	6.7E2	26	1.22E3	3.2E2	12	0.46	0.05
	2010 JG	2019 Nov 12 11:47	0^h19^m	0.050	1.2	2.23E3	5.7E2	24	8.8E2	2.4E2	9.7	0.39	0.05
	2011 HP	2019 May 29 04:44	0^h07^m	0.032	1.7	2.11E4	5.3E3	51	8.2E3	2.1E3	52	0.39	0.02
	2011 HP	2019 May 30 05:12	0^h06^m	0.031	1.6	1.44E4	3.6E3	48	5.0E3	1.3E3	46	0.35	0.02
	2011 WN15	2019 Dec 12 21:53	0^h12^m	0.073	3.2	5.1E4	1.3E4	37	N/A	N/A	N/A	N/A	N/A
	2011 WN15	2019 Dec 13 21:59	0^h17^m	0.087	3.7	8.2E4	2.1E4	36	N/A	N/A	N/A	N/A	N/A
	2011 YS62	2019 Nov 13 07:05	0^h18^m	0.106	1.4	7.4E4	1.9E4	26	1.71E4	4.7E3	8.7	0.23	0.03
	2011 YS62	2019 Nov 14 07:05	0^h35^m	0.105	1.2	7.0E4	1.8E4	39	1.38E4	3.7E3	11	0.20	0.02
	2012 MS4	2018 Dec 21 19:35	0^h14^m	0.084	0.28	2.76E4	7.0E3	23	6.3E3	1.7E3	11	0.23	0.03
	2013 CW32	2019 Feb 01 02:50	0^h07^m	0.042	2.2	1.21E4	3.0E3	51	5.3E3	1.3E3	33	0.44	0.03
	2013 UG1	2018 Oct 16 09:49	1^h02^m	0.030	7.7	1.07E2	3.2E1	5.8	N/A	N/A	N/A	N/A	N/A
	2015 DP155	2018 Jun 09 04:22	0^h10^m	0.024	1.0	3.01E3	8.0E2	11	4.2E2	1.2E2	8.2	0.14	0.02
	2015 DP155	2018 Jun 10 04:16	0^h06^m	0.023	0.80	3.32E3	9.3E2	7.8	9.6E2	2.7E2	8.2	0.29	0.05
	2015 DP155	2018 Jun 11 04:29	0^h09^m	0.023	1.3	5.9E3	1.5E3	45	6.7E2	1.7E2	40	0.11	0.01
	2015 DP155	2018 Jun 12 04:41	0^h05^m	0.023	1.5	5.9E3	1.5E3	34	6.6E2	1.7E2	29	0.11	0.01
	2015 JD1	2019 Nov 01 22:31	0^h14^m	0.035	0.90	3.36E3	8.4E2	45	3.76E3	9.4E2	49	1.12	0.07
	2015 JD1	2019 Nov 02 22:53	0^h24^m	0.033	1.0	2.55E3	6.4E2	54	3.96E3	9.9E2	62	1.55	0.09
	2015 JD1	2019 Nov 03 23:30	0^h06^m	0.033	0.93	4.7E3	1.2E3	34	6.6E3	1.7E3	37	1.39	0.09
	2015 QM3	2018 Aug 29 17:44	0^h21^m	0.082	2.1	2.48E4	6.2E3	32	1.06E4	2.7E3	14	0.43	0.04
	2016 AZ8	2019 Jan 04 17:41	0^h15^m	0.033	1.3	1.78E3	4.9E2	8.6	1.68E2	6.3E1	3.6	0.16	0.05
	2016 GW221	2019 Apr 09 05:52	0^h35^m	0.027	1.9	6.8E1	1.8E1	10	N/A	N/A	N/A	N/A	N/A
	2016 OF	2019 Jul 10 10:02	0^h08^m	0.036	0.58	2.35E2	6.6E1	8.0	N/A	N/A	N/A	N/A	N/A
	2016 PD1	2019 Aug 23 04:53	0^h41^m	0.031	0.50	7.1E1	1.9E1	10	N/A	N/A	N/A	N/A	N/A
	2016 TH94	2019 Oct 26 02:38	0^h10^m	0.029	0.40	4.6E2	1.2E2	22	2.76E2	7.0E1	19	0.60	0.05
	2017 QL33	2017 Dec 18 19:14	1^h05^m	0.063	0.66	1.73E3	4.4E2	29	4.9E2	1.4E2	8.5	0.29	0.04

Table 2
(Continued)

Asteroid Number	Name or Designation	Start Date and Time (UT)	Duration Δt	d (au)	B (Hz)	σ_{OC} (m^2)	$\Delta\sigma_{OC}$ (m^2)	S/N_{OC}	σ_{SC} (m^2)	$\Delta\sigma_{SC}$ (m^2)	S/N_{SC}	μ_C	$\Delta\mu_C$
	2017 QL33	2017 Dec 22 19:27	$0^{h}05^{m}$	0.048	0.79	1.91E3	4.9E2	15	4.7E2	1.6E2	4.6	0.24	0.06
	2017 VR12	2018 Mar 06 05:23	$0^{h}05^{m}$	0.010	3.2	6.3E3	1.6E3	39	1.59E3	4.0E2	37	0.25	0.02
	2017 VR12	2018 Mar 07 05:54	$0^{h}13^{m}$	0.010	3.6	5.9E3	1.5E3	14	1.06E3	2.7E2	16	0.18	0.02
	2017 XT61	2018 Jan 03 22:35	$0^{h}22^{m}$	0.042	3.5	7.7E2	2.0E2	12	N/A	N/A	N/A	N/A	N/A
	2017 YE5	2018 Jun 23 10:06	$0^{h}24^{m}$	0.042	0.40	2.91E5	7.3E4	40	9.7E4	2.4E4	39	0.33	0.02
	2017 YE5	2018 Jun 26 07:25	$0^{h}09^{m}$	0.056	1.5	4.2E5	1.0E5	58	1.32E5	3.3E4	56	0.32	0.02
	2018 AJ	2018 Jan 22 06:23	$0^{h}04^{m}$	0.013	1.9	5.9E1	1.5E1	21	1.91E1	5.0E0	14	0.32	0.03
	2018 BH3	2018 Jan 26 02:41	$0^{h}28^{m}$	0.032	0.16	2.72E1	7.9E0	6.7	N/A	N/A	N/A	N/A	N/A
	2018 BM5	2018 Jan 26 01:55	$0^{h}14^{m}$	0.012	2.9	1.89E1	4.8E0	26	N/A	N/A	N/A	N/A	N/A
	2018 BT1	2018 Jan 20 06:20	$0^{h}23^{m}$	0.049	0.23	1.93E2	5.4E1	8.3	1.32E2	4.0E1	5.8	0.68	0.15
	2018 DH1	2018 Mar 23 04:33	$0^{h}08^{m}$	0.042	1.8	2.48E4	6.2E3	62	9.1E3	2.3E3	57	0.37	0.02
	2018 DT	2018 Feb 26 04:07	$0^{h}29^{m}$	0.011	6.0	1.70E1	4.3E0	34	N/A	N/A	N/A	N/A	N/A
	2018 DT	2018 Mar 07 07:44	$0^{h}30^{m}$	0.016	5.5	1.37E1	3.7E0	10	N/A	N/A	N/A	N/A	N/A
	2018 EB	2018 Oct 05 08:27	$0^{h}14^{m}$	0.042	1.8	2.17E4	5.4E3	76	6.7E3	1.7E3	59	0.31	0.02
	2018 EB	2018 Oct 07 08:28	$0^{h}08^{m}$	0.040	2.0	2.54E4	6.4E3	58	9.8E3	2.4E3	54	0.39	0.02
	2018 EB	2018 Oct 07 08:28	$0^{h}08^{m}$	0.040	2.1	2.73E4	6.8E3	60	8.4E3	2.1E3	50	0.31	0.02
	2018 EJ4	2018 Jun 06 02:15	$0^{h}07^{m}$	0.022	0.97	1.32E3	3.3E2	38	3.92E2	9.9E1	34	0.30	0.02
	2018 FB	2018 Mar 23 02:09	$0^{h}18^{m}$	0.036	0.39	1.08E2	2.9E1	10.0	3.7E1	1.4E1	3.6	0.35	0.10
	2018 FH1	2018 Mar 23 03:06	$0^{h}05^{m}$	0.024	0.31	2.50E2	6.4E1	18	6.1E1	1.6E1	12	0.24	0.03
	2018 LK	2018 Jun 11 07:19	$0^{h}19^{m}$	0.038	0.77	1.66E3	4.2E2	44	1.37E3	3.4E2	41	0.83	0.05
	2018 LQ2	2018 Aug 22 02:22	$1^{h}35^{m}$	0.025	0.70	2.24E1	6.2E0	8.1	N/A	N/A	N/A	N/A	N/A
	2018 MD7	2018 Aug 01 08:58	$2^{h}14^{m}$	0.062	0.45	2.63E2	8.0E1	5.8	N/A	N/A	N/A	N/A	N/A
	2018 NB	2018 Aug 01 08:12	$0^{h}10^{m}$	0.098	0.22	1.44E4	3.7E3	16	5.2E3	1.5E3	6.8	0.36	0.06
	2018 NE1	2018 Jul 21 07:04	$0^{h}58^{m}$	0.026	12.4	1.06E2	2.9E1	8.5	3.8E1	1.6E1	3.1	0.36	0.13
	2018 NM	2018 Jul 20 13:29	$1^{h}03^{m}$	0.013	25.9	2.46E1	6.4E0	14	5.9E0	2.3E0	3.4	0.24	0.07
	2018 NV	2018 Jul 12 00:56	$0^{h}04^{m}$	0.032	0.79	1.02E3	2.6E2	23	4.6E2	1.2E2	15	0.45	0.04
	2018 PL10	2018 Aug 20 07:23	$1^{h}19^{m}$	0.052	1.5	4.9E2	1.5E2	6.0	N/A	N/A	N/A	N/A	N/A
	2018 RC4	2018 Sep 14 05:10	$0^{h}38^{m}$	0.027	5.5	1.40E2	3.8E1	8.8	N/A	N/A	N/A	N/A	N/A
	2018 TG6	2018 Dec 10 15:36	$0^{h}49^{m}$	0.012	7.1	7.5E0	2.1E0	8.3	N/A	N/A	N/A	N/A	N/A
	2018 TR4	2018 Oct 12 03:04	$0^{h}11^{m}$	0.018	1.1	2.69E2	6.8E1	37	6.3E1	1.6E1	19	0.23	0.02
	2018 TZ2	2018 Oct 16 08:26	$0^{h}35^{m}$	0.024	60.0	9.8E2	2.5E2	25	1.34E2	5.1E1	3.4	0.14	0.04
	2018 VX8	2019 May 11 08:47	$0^{h}05^{m}$	0.018	1.8	3.22E3	8.3E2	17	8.8E2	2.2E2	18	0.27	0.03
	2018 XG5	2019 May 02 22:30	$0^{h}18^{m}$	0.067	2.0	9.8E3	2.5E3	24	2.92E3	8.2E2	7.7	0.30	0.04
	2018 XG5	2019 May 08 00:34	$0^{h}31^{m}$	0.079	2.1	9.5E3	2.4E3	17	2.72E3	8.2E2	5.9	0.29	0.05
	2018 XJ1	2018 Dec 18 07:49	$0^{h}09^{m}$	0.023	3.1	1.41E2	3.7E1	15	N/A	N/A	N/A	N/A	N/A
	2019 AK3	2019 Jan 10 06:27	$0^{h}37^{m}$	0.019	1.8	2.55E1	7.0E0	9.0	1.34E1	4.4E0	4.8	0.53	0.13
	2019 AP11	2019 Jan 27 23:47	$0^{h}10^{m}$	0.026	0.31	1.01E2	2.7E1	13	N/A	N/A	N/A	N/A	N/A
	2019 AR2	2019 Jan 10 01:36	$1^{h}19^{m}$	0.022	21.2	5.4E1	1.5E1	7.3	N/A	N/A	N/A	N/A	N/A
	2019 AV2	2019 Jan 25 23:41	$0^{h}16^{m}$	0.068	0.14	2.43E3	6.3E2	14	6.5E2	2.2E2	4.7	0.27	0.06
	2019 AW7	2019 Jan 10 07:11	$0^{h}07^{m}$	0.030	0.85	1.85E3	4.7E2	30	6.3E2	1.6E2	26	0.34	0.02
	2019 AX5	2019 Jan 10 00:56	$0^{h}13^{m}$	0.025	0.69	1.00E2	2.6E1	18	6.7E1	1.8E1	12	0.67	0.07
	2019 BG3	2019 Jan 28 23:56	$0^{h}13^{m}$	0.009	21.4	1.98E2	4.9E1	104	1.68E2	4.2E1	101	0.85	0.04
	2019 BJ1	2019 Jan 29 23:22	$0^{h}22^{m}$	0.012	22.8	1.68E2	4.2E1	99	3.12E1	8.0E0	20	0.19	0.01
	2019 CD5	2019 Mar 16 05:13	$0^{h}23^{m}$	0.048	0.17	8.3E2	2.1E2	16	2.77E2	8.1E1	6.4	0.33	0.06
	2019 CD5	2019 Mar 22 12:19	$0^{h}06^{m}$	0.033	0.25	3.51E3	9.1E2	14	2.46E2	6.7E1	9.1	0.07	0.01
	2019 CL2	2019 Mar 25 14:14	$0^{h}15^{m}$	0.040	0.99	1.26E3	3.2E2	28	2.13E2	6.7E1	5.3	0.17	0.03
	2019 CN2	2019 Feb 09 05:40	$0^{h}36^{m}$	0.011	23.8	7.1E0	1.9E0	11	N/A	N/A	N/A	N/A	N/A
	2019 DN	2019 Mar 07 03:32	$0^{h}13^{m}$	0.035	0.32	1.17E3	3.0E2	26	3.22E2	8.4E1	14	0.28	0.03
	2019 DN	2019 Mar 08 02:56	$0^{h}17^{m}$	0.035	0.43	1.97E3	4.9E2	38	6.7E2	1.7E2	29	0.34	0.02
	2019 EN	2019 Apr 04 14:36	$0^{h}03^{m}$	0.080	1.9	4.8E4	1.2E4	19	1.14E4	3.4E3	6.0	0.24	0.04
	2019 FU	2019 Apr 08 21:39	$0^{h}03^{m}$	0.014	7.6	1.61E3	4.0E2	49	4.3E2	1.1E2	42	0.27	0.02
	2019 GJ4	2019 Apr 09 03:29	$0^{h}14^{m}$	0.016	13.7	9.2E1	2.3E1	21	1.45E1	5.6E0	3.4	0.16	0.05
	2019 GM4	2019 Apr 19 01:06	$1^{h}01^{m}$	0.032	85.3	6.8E2	1.8E2	10	N/A	N/A	N/A	N/A	N/A
	2019 GN4	2019 Apr 12 05:46	$0^{h}54^{m}$	0.026	25.4	2.61E2	7.3E1	7.9	N/A	N/A	N/A	N/A	N/A
	2019 GO4	2019 Apr 12 06:55	$0^{h}02^{m}$	0.019	5.0	2.21E2	5.7E1	15	5.2E1	1.8E1	4.0	0.23	0.06
	2019 GT1	2019 May 09 20:53	$0^{h}28^{m}$	0.024	0.60	3.25E1	9.2E0	7.5	N/A	N/A	N/A	N/A	N/A
	2019 GT3	2019 Sep 05 22:28	$0^{h}37^{m}$	0.050	15.2	4.3E3	1.1E3	18	7.8E2	2.6E2	4.6	0.18	0.04
	2019 JE	2019 May 08 07:01	$0^{h}17^{m}$	0.012	1.8	4.8E0	1.4E0	6.8	1.85E0	0.74E0	3.2	0.39	0.14
	2019 JG1	2019 May 15 03:28	$0^{h}30^{m}$	0.017	1.6	1.33E1	3.6E0	9.9	4.5E0	1.6E0	4.0	0.34	0.09
	2019 JN2	2019 May 14 22:16	$0^{h}39^{m}$	0.018	1.4	1.16E1	3.2E0	9.4	N/A	N/A	N/A	N/A	N/A
	2019 JU5	2019 May 16 03:51	$0^{h}15^{m}$	0.050	1.0	1.20E3	3.1E2	14	2.9E2	1.0E2	4.2	0.24	0.06
	2019 KD3	2019 Jul 14 03:15	$2^{h}06^{m}$	0.041	112	9.8E2	3.0E2	5.7	N/A	N/A	N/A	N/A	N/A

Table 2
(Continued)

Asteroid Number	Name or Designation	Start Date and Time (UT)	Duration Δt	d (au)	B (Hz)	σ_{OC} (m^2)	$\Delta\sigma_{OC}$ (m^2)	S/N$_{OC}$	σ_{SC} (m^2)	$\Delta\sigma_{SC}$ (m^2)	S/N$_{SC}$	μ_C	$\Delta\mu_C$
	2019 KV	2019 May 29 03:19	$1^{h}14^{m}$	0.018	0.92	5.6E0	1.6E0	8.1	N/A	N/A	N/A	N/A	N/A
	2019 KZ3	2019 Jun 05 02:58	$0^{h}11^{m}$	0.022	3.4	2.38E2	6.0E1	24	2.9E1	1.1E1	3.6	0.12	0.03
	2019 LU	2019 Jun 18 09:08	$0^{h}05^{m}$	0.014	3.4	1.62E2	4.1E1	40	3.9E1	1.0E1	18	0.24	0.02
	2019 LV1	2019 Jun 26 23:48	$0^{h}18^{m}$	0.017	0.78	6.8E1	1.7E1	26	5.6E0	2.2E0	3.3	0.08	0.03
	2019 MF1	2019 Jul 08 08:54	$0^{h}27^{m}$	0.081	0.36	2.36E3	6.4E2	9.9	N/A	N/A	N/A	N/A	N/A
	2019 MF1	2019 Jul 10 07:58	$0^{h}34^{m}$	0.085	0.30	1.34E3	3.9E2	7.0	N/A	N/A	N/A	N/A	N/A
	2019 MT	2019 Jun 28 02:41	$0^{h}31^{m}$	0.024	1.0	3.6E1	1.1E1	5.6	N/A	N/A	N/A	N/A	N/A
	2019 NE2	2019 Jul 09 00:32	$0^{h}16^{m}$	0.080	0.41	1.96E3	5.8E2	6.2	N/A	N/A	N/A	N/A	N/A
	2019 NN3	2019 Jul 08 23:26	$0^{h}09^{m}$	0.009	17.7	1.23E2	3.1E1	73	2.12E1	5.4E0	21	0.17	0.01
	2019 NX1	2019 Jul 08 09:58	$0^{h}37^{m}$	0.013	6.2	1.31E1	3.7E0	7.6	N/A	N/A	N/A	N/A	N/A
	2019 OK	2019 Jul 25 17:45	$0^{h}04^{m}$	0.010	39.8	6.2E2	1.6E2	93	2.07E2	5.2E1	53	0.33	0.02
	2019 PZ2	2019 Aug 17 04:51	$0^{h}23^{m}$	0.064	4.0	6.8E3	1.8E3	17	2.20E3	6.2E2	7.7	0.32	0.05
	2019 QY1	2019 Nov 12 13:44	$0^{h}42^{m}$	0.079	0.28	3.50E3	9.2E2	12	4.0E3	1.0E3	19	1.14	0.12
	2019 RA	2019 Sep 06 03:45	$0^{h}19^{m}$	0.012	25.3	9.2E1	2.3E1	35	1.40E1	3.9E0	7.6	0.15	0.02
	2019 RC	2019 Sep 17 06:48	$0^{h}12^{m}$	0.045	0.27	5.7E3	1.4E3	26	7.3E3	1.9E3	26	1.29	0.09
	2019 RX1	2019 Sep 09 07:32	$0^{h}28^{m}$	0.025	0.54	6.1E1	1.6E1	12	2.38E1	7.0E0	6.5	0.39	0.07
	2019 SD8	2019 Oct 01 02:51	$0^{h}09^{m}$	0.007	45.3	1.30E1	3.4E0	13	2.12E0	0.87E0	3.1	0.16	0.06
	2019 SE8	2019 Oct 01 02:31	$0^{h}13^{m}$	0.010	11.6	1.29E1	3.8E0	6.2	N/A	N/A	N/A	N/A	N/A
	2019 SH3	2019 Sep 28 03:18	$0^{h}29^{m}$	0.018	73.7	1.61E2	4.2E1	12	8.0E1	2.2E1	8.3	0.49	0.08
	2019 SL7	2019 Oct 10 15:15	$0^{h}31^{m}$	0.011	2.0	1.42E2	3.5E1	72	3.54E1	8.9E0	55	0.25	0.01
	2019 SP	2019 Sep 28 01:06	$0^{h}13^{m}$	0.029	0.68	4.2E2	1.1E2	22	1.29E2	3.5E1	10	0.31	0.04
	2019 SW5	2019 Sep 28 04:56	$0^{h}28^{m}$	0.017	20.8	6.4E1	1.7E1	9.0	2.08E1	7.2E0	4.1	0.33	0.09
	2019 SX3	2019 Oct 01 05:58	$0^{h}11^{m}$	0.023	0.63	2.54E2	6.5E1	22	N/A	N/A	N/A	N/A	N/A
	2019 TM	2019 Oct 08 19:56	$0^{h}36^{m}$	0.024	7.4	1.14E2	3.1E1	8.7	N/A	N/A	N/A	N/A	N/A
	2019 UF5	2019 Oct 25 04:52	$0^{h}21^{m}$	0.018	0.55	1.61E1	4.4E0	9.7	N/A	N/A	N/A	N/A	N/A
	2019 UL8	2019 Nov 02 05:51	$0^{h}08^{m}$	0.014	40.0	9.4E1	2.4E1	16	2.09E1	7.9E0	3.5	0.22	0.07
	2019 UN12	2019 Nov 11 05:21	$0^{h}23^{m}$	0.040	21.4	6.3E2	1.9E2	5.7	N/A	N/A	N/A	N/A	N/A
	2019 UN12	2019 Nov 12 05:30	$0^{h}10^{m}$	0.024	20.5	5.3E2	1.4E2	18	2.65E2	7.2E1	9.1	0.50	0.07
	2019 UO	2019 Dec 26 20:27	$0^{h}14^{m}$	0.087	1.3	2.09E4	5.4E3	15	N/A	N/A	N/A	N/A	N/A
	2019 UT7	2019 Oct 28 05:06	$0^{h}24^{m}$	0.016	3.1	1.59E1	4.5E0	7.5	7.1E0	2.3E0	4.8	0.45	0.11
	2019 WO2	2019 Dec 08 02:39	$0^{h}22^{m}$	0.014	4.3	1.70E2	4.3E1	52	N/A	N/A	N/A	N/A	N/A
	2019 WR3	2019 Dec 08 04:39	$0^{h}23^{m}$	0.037	44.5	4.1E3	1.0E3	21	N/A	N/A	N/A	N/A	N/A
	2019 WT3	2019 Dec 08 05:27	$0^{h}07^{m}$	0.026	0.41	2.54E2	6.5E1	16	N/A	N/A	N/A	N/A	N/A
	2019 XF	2019 Dec 17 09:13	$2^{h}45^{m}$	0.026	62.6	2.12E2	5.8E1	9.2	N/A	N/A	N/A	N/A	N/A
	2019 XO3	2019 Dec 19 10:41	$0^{h}27^{m}$	0.009	21.6	1.40E1	3.6E0	14	N/A	N/A	N/A	N/A	N/A
	2019 XQ3	2019 Dec 19 09:03	$0^{h}45^{m}$	0.043	72.6	2.91E3	8.0E2	8.7	N/A	N/A	N/A	N/A	N/A
	2019 XR1	2019 Dec 08 06:08	$0^{h}09^{m}$	0.023	2.1	1.76E2	4.6E1	16	N/A	N/A	N/A	N/A	N/A
	2019 XW	2019 Dec 08 07:22	$0^{h}19^{m}$	0.032	8.0	6.6E2	1.8E2	11	N/A	N/A	N/A	N/A	N/A
	2019 YX1	2019 Dec 26 11:35	$0^{h}14^{m}$	0.014	2.5	1.86E2	4.7E1	33	N/A	N/A	N/A	N/A	N/A

Notes. Columns 1 and 2 list the asteroid number and name or provisional designation, column 3 lists the UT start date and time of the observation, column 4 lists its duration (Δt) defined as the time of the transmittal of the first scan to the time of receiving the last scan (the total integration time is up to one-half of the reported duration as the system is cycling between transmit and receive modes), column 5 lists the distance to the target in astronomical units, column 6 lists the observed limb-to-limb Doppler bandwidth in hertz, columns 7 and 8 list the radar cross section in the opposite-sense circular (OC) polarization and its uncertainty in square meters, column 9 lists the signal-to-noise ratio (S/N) in the OC polarization, columns 10 and 11 list the radar cross section in the same-sense circular (SC) polarization and its uncertainty in square meters, column 12 lists the S/N in the SC polarization, and columns 13 and 14 list the circular-polarization ratio and its uncertainty. Some targets were detected in OC but not SC. The cross sections' uncertainties include contributions from thermal noise, self-noise, and systematic uncertainty (due to imperfectly known system calibration parameters). Each cross section's uncertainty is printed with two significant digits. The cross section's value is printed so that its least significant digit corresponds to the same power of 10, so the cross sections' values are printed with two or three significant digits. S/N depends on thermal noise and self-noise but not systematic uncertainty. For most of these cross sections and polarization ratios, the dominant source of uncertainty is systematic, which contributes a 25% relative uncertainty to each cross section and 5% relative uncertainty to each circular-polarization ratio.

(This table is available in machine-readable form.)

Table 3
Continuous-wave Observations of NEAs That Were Detected but Not Clearly Resolved in Frequency, or Their Measured Radar-scattering Properties Were Deemed Unreliable Due to Systematic Issues

Name or Designation	Start Date and Time (UT)	Duration Δt	d (au)	B (Hz)	f_{res} (Hz)	σ_{OC} (m^2)	S/N_{OC}	μ_C	Issue
2003 SD220	2018 Dec 21 15:48	0^h04^m	0.021	0.22	0.08	2.1E5	12	0.2	Unresolved
1993 VD	2018 Jan 23 13:13	0^h38^m	0.038	3.6	0.33	2.90E2	>78	N/A	System issue
1998 FF14	2019 Sep 23 15:50	0^h11^m	0.029	1.10	0.05	>4E2	17	0.1	Unfocused
1998 SD9	2018 Aug 30 22:17	0^h18^m	0.015	0.43	0.14	5.1E1	27	0.2	Unresolved
2014 WG365	2018 May 25 09:55	0^h31^m	0.070	0.05	0.02	1.8E4	20	0.1	Unresolved
2015 EG	2019 Mar 07 01:42	0^h14^m	0.014	0.50	0.17	1.4E1	17	0.4	Unresolved
2017 SL16	2019 Sep 23 04:03	2^h19^m	0.022	0.36	0.07	>7E0	5	N/A	Marginal
2018 MB7	2018 Jul 05 13:07	0^h03^m	0.011	0.67	0.33	3.3E1	13	0.3	Unresolved
2018 QU1	2018 Sep 08 02:45	0^h18^m	0.036	0.11	0.04	6.7E2	21	0.1	Unresolved
2018 RB6	2018 Sep 14 02:24	1^h07^m	0.017	0.33	0.11	>3E0	5	N/A	Unresolved; Marginal
2018 RQ2	2018 Sep 14 07:35	0^h12^m	0.027	0.16	0.05	2.8E2	16	0.9	Unresolved
2018 XC4	2018 Dec 18 04:18	0^h15^m	0.016	0.38	0.13	1.1E1	10	0.4	Unresolved
2018 XN	2019 Jan 14 17:56	0^h24^m	0.031	0.13	0.04	9.2E1	10	0.7	Unresolved
2018 XS4	2018 Dec 18 06:46	0^h14^m	0.012	0.75	0.25	7.2E1	31	0.1	Unresolved
2019 CT1	2019 Feb 09 06:59	0^h04^m	0.055	0.06	0.02	2.7E3	4	N/A	Unresolved; Marginal
2019 FN2	2019 Apr 21 19:31	0^h14^m	0.018	0.30	0.10	3.7E2	27	0.4	Unresolved
2019 GL4	2019 Apr 09 05:24	0^h21^m	0.045	0.08	0.03	2.7E2	7	1.3	Unresolved; Inconsistent
2019 GL4	2019 Apr 12 04:32	0^h01^m	0.034	0.30	0.04	6.6E2	6	0.6	Marginal; Inconsistent
2019 JJ3	2019 May 09 23:07	0^h13^m	0.010	1.50	0.50	>4E0	17	0.3	Unresolved; Unfocused
2019 JJ3	2019 May 09 23:22	0^h01^m	0.010	1.00	0.50	7E0	8	0.1	Unresolved
2019 JL3	2019 May 18 03:48	0^h18^m	0.013	0.60	0.20	9.3E1	37	0.1	Unresolved
2019 KA4	2019 Jun 05 02:19	0^h09^m	0.022	0.21	0.07	9.4E1	18	0.1	Unresolved
2019 KG2	2019 May 30 21:42	0^h07^m	0.010	1.50	0.50	>2E0	11	0.3	Unresolved
2019 OD	2019 Jul 25 14:37	0^h13^m	0.012	0.50	0.25	3.8E2	25	0.3	Unresolved
2019 QZ3	2019 Sep 07 06:28	0^h10^m	0.027	0.16	0.05	3.6E2	18	0.4	Unresolved
2019 SU3	2019 Oct 01 03:42	0^h20^m	0.012	0.75	0.25	>7E0	13	N/A	Unresolved
2019 UG12	2019 Nov 01 22:11	0^h10^m	0.011	0.67	0.33	>6E0	7	N/A	Unresolved

Note. Column 1 lists the asteroid's provisional designation, column 2 lists the UT start date and time of the observation, column 3 lists its duration (Δt), column 4 lists the distance to the target in astronomical units, and column 5 lists the upper limit of the limb-to-limb Doppler bandwidth in hertz, column 6 lists the frequency resolution (in hertz with the precision of two decimals; however, the given Doppler bandwidth is an integer multiple of the frequency resolution), columns 7 and 8 list the OC radar cross section and its S/N (Equation (2)), column 9 lists the SC/OC ratio, and column 10 lists the issues with the result ("Unresolved": Doppler bandwidth is up to three frequency bins; "Unfocused": the target was on the edge of the beam; "Marginal": the maximum integrated S/N of the NEA in the OC polarization was only four to six noise standard deviations; "Inconsistent": the measurement was significantly inconsistent with another day's measurement). For these targets, the radar cross sections and circular-polarization ratios should be considered with extra caution; the uncertainty is on the order of 50%.

(This table is available in machine-readable form.)

Table 4
Summary of the Delay-Doppler Imaging Data for the 37 Selected Asteroids

Asteroid Number	Name or Designation	Start Date and Times (UT)	Duration Δt	Range Res. (m)	Max. Range Extent (m)	Max. Doppler Bandwidth (Hz)
3752	Camillo	2018 Feb 21 00:17	0^h40^m	75	1100	2.7
3752	Camillo	2018 Feb 21 23:40	0^h16^m	75	1400	2.0
3752	Camillo	2018 Feb 22 00:12	1^h04^m	7.5 (4)	1500	1.8
3752	Camillo	2018 Feb 22 23:45	0^h37^m	75	2100	1.0
3752	Camillo	2018 Feb 23 00:48	0^h17^m	7.5 (4)	1100	0.9
13553	Masaakikoyama	2018 Aug 08 04:18	2^h12^m	75	830	0.6
13553	Masaakikoyama	2018 Aug 15 04:16	0^h39^m	75	230^B	0.4^B
66391	Moshup	2018 May 29 05:32	0^h16^m	75	450	10
66391	Moshup	2018 May 30 04:47	1^h30^m	75	450	10
66391	Moshup	2018 May 31 04:55	1^h02^m	75	450	9.1
66391	Moshup	2019 May 29 23:02	0^h22^m	7.5 (4)	700	11
66391	Squannit	2019 May 29 23:02	0^h22^m	7.5 (4)	75	0.7
66391	Moshup	2019 May 29 23:30	0^h28^m	75	530	11
66391	Moshup	2019 May 30 22:50	1^h40^m	7.5 (4)	740	12
66391	Squannit	2019 May 30 22:50	1^h40^m	7.5 (4)	90	2.0
66391	Moshup	2019 May 31 22:50	1^h52^m	7.5 (4)	600	11
66391	Moshup	2019 Jun 01 22:54	1^h12^m	7.5 (6)	400	10
66391	Moshup	2019 Jun 02 23:37	2^h17^m	75	600	10
68347	2001 KB67	2018 May 28 10:28	0^h12^m	75	150^B	1.2
68347	2001 KB67	2018 May 28 10:45	1^h32^m	7.5	110	1.1
68347	2001 KB67	2018 May 29 09:19	1^h45^m	7.5	110	1.0

Table 4
(Continued)

Asteroid Number	Name or Designation	Start Date and Times (UT)	Duration Δt	Range Res. (m)	Max. Range Extent (m)	Max. Doppler Bandwidth (Hz)
68347	2001 KB67	2018 May 30 08:15	$1^{h}15^{m}$	7.5	110	0.9
68347	2001 KB67	2018 May 31 07:12	$1^{h}05^{m}$	7.5	110	0.8
68347	2001 KB67	2018 Jun 01 06:09	$0^{h}59^{m}$	7.5 (2)	140	0.7
68347	2001 KB67	2018 Jun 01 07:13	$0^{h}17^{m}$	7.5 (4)	140	0.8
68950	2002 QF15	2019 May 20 22:06	$0^{h}54^{m}$	7.5	620	1.2
68950	2002 QF15	2019 May 21 21:58	$1^{h}35^{m}$	7.5 (4)	670	1.1
68950	2002 QF15	2019 May 22 21:52	$2^{h}04^{m}$	7.5 (4)	700	1.1
68950	2002 QF15	2019 May 23 22:57	$1^{h}21^{m}$	7.5 (4)	860	1.0
68950	2002 QF15	2019 May 24 22:19	$2^{h}22^{m}$	7.5 (4)	780	0.9
68950	2002 QF15	2019 May 26 23:00	$2^{h}11^{m}$	7.5 (4)	670	0.7
68950	2002 QF15	2019 Jun 05 01:51	$0^{h}16^{m}$	150 (2)	750^{B}	0.7^{B}
90403	2003 YE45	2019 Jun 28 12:48	$0^{h}29^{m}$	75	830^{B}	0.03^{B}
90403	2003 YE45	2019 Jul 07 10:15	$0^{h}50^{m}$	75	830	0.05
141593	2002 HK12	2019 Aug 11 16:28	$2^{h}09^{m}$	7.5 (4)	240	1.4
141593	2002 HK12	2019 Aug 12 16:14	$1^{h}22^{m}$	7.5 (4)	480	1.3
141593	2002 HK12	2019 Aug 14 15:46	$1^{h}50^{m}$	7.5 (4)	420	1.2
141593	2002 HK12	2019 Aug 15 15:47	$1^{h}14^{m}$	7.5 (4)	340	1.4
141593	2002 HK12	2019 Aug 16 15:56	$0^{h}41^{m}$	7.5 (4)	200	1.3
141593	2002 HK12	2019 Aug 17 14:47	$1^{h}28^{m}$	7.5 (4)	410	0.7
144332	2004 DV24	2018 Sep 13 23:03	$0^{h}39^{m}$	7.5 (4)	110^{B}	2.1^{B}
144332	2004 DV24	2018 Sep 14 22:24	$1^{h}42^{m}$	7.5 (4)	680	4.6
144332	2004 DV24	2018 Sep 15 22:07	$1^{h}35^{m}$	7.5 (4)	720	4.7
153814	2001 WN5	2019 Aug 21 16:59	$1^{h}23^{m}$	75 (2)	300	4.8
153814	2001 WN5	2019 Aug 22 16:27	$1^{h}54^{m}$	75	530	7.6
153814	2001 WN5	2019 Aug 24 16:22	$1^{h}27^{m}$	75 (2)	450	5.5
162082	1998 HL1	2019 Oct 25 04:06	$0^{h}38^{m}$	7.5 (2)	160	1.0
162082	1998 HL1	2019 Oct 26 03:57	$0^{h}58^{m}$	7.5 (2)	170	0.9
162082	1998 HL1	2019 Oct 27 04:58	$0^{h}22^{m}$	7.5 (2)	180	0.9
162082	1998 HL1	2019 Oct 28 04:30	$0^{h}26^{m}$	7.5 (4)	170	0.9
264357	2000 AZ93	2019 Dec 17 20:11	$1^{h}10^{m}$	7.5	50^{B}	0.3
398188	Agni	2018 Jul 23 04:16	$1^{h}27^{m}$	75	380^{B}	0.3^{B}
398188	Agni	2018 Jul 26 02:57	$2^{h}13^{m}$	7.5 (4)	260	0.5
398188	Agni	2018 Aug 03 01:42	$0^{h}42^{m}$	7.5 (4)	210	0.6
418849	2008 WM64	2017 Dec 21 06:18	$0^{h}17^{m}$	75	230^{B}	1.4
418849	2008 WM64	2017 Dec 21 07:12	$2^{h}20^{m}$	7.5 (4)	90	1.3
418849	2008 WM64	2017 Dec 22 06:28	$1^{h}12^{m}$	7.5 (4)	130	2.4
418849	2008 WM64	2017 Dec 23 06:03	$0^{h}58^{m}$	7.5 (4)	140	1.8
418849	2008 WM64	2018 Dec 24 01:20	$1^{h}37^{m}$	7.5 (4)	130	1.3
441987	2010 NY65	2018 Jun 19 17:33	$0^{h}34^{m}$	75 (2)	300^{B}	1.0
441987	2010 NY65	2018 Jun 20 16:32	$1^{h}34^{m}$	7.5 (4)	150	1.2
441987	2010 NY65	2018 Jun 28 02:04	$1^{h}07^{m}$	7.5 (4)	120	0.5
441987	2010 NY65	2018 Jun 29 02:50	$0^{h}55^{m}$	7.5 (4)	105	0.6
441987	2010 NY65	2019 Jun 19 17:10	$0^{h}58^{m}$	7.5 (2)	75	0.9
441987	2010 NY65	2019 Jun 20 16:42	$1^{h}19^{m}$	7.5 (2)	85	1.0
441987	2010 NY65	2019 Jun 28 02:03	$0^{h}35^{m}$	7.5 (2)	110	0.5
441987	2010 NY65	2019 Jun 29 01:32	$0^{h}22^{m}$	7.5 (4)	110	0.5
454094	2013 BZ45	2019 Aug 02 19:03	$0^{h}54^{m}$	7.5	82	0.5
454094	2013 BZ45	2019 Aug 05 18:14	$0^{h}22^{m}$	7.5 (4)	90	0.4
454094	2013 BZ45	2019 Aug 05 18:41	$1^{h}04^{m}$	7.5	67	0.4
481394	2006 SF6	2019 Nov 11 03:55	$1^{h}16^{m}$	7.5 (4)	260	0.6
481394	2006 SF6	2019 Nov 12 03:13	$1^{h}58^{m}$	7.5 (4)	270	0.5
481394	2006 SF6	2019 Nov 13 03:12	$1^{h}39^{m}$	7.5 (4)	320	0.7
481394	2006 SF6	2019 Nov 14 03:09	$1^{h}45^{m}$	7.5 (4)	290	1.0
481394	2006 SF6	2019 Nov 15 02:44	$0^{h}27^{m}$	7.5 (4)	300	0.9
481394	2006 SF6	2019 Nov 15 03:16	$1^{h}14^{m}$	7.5 (2)	170	0.8
494999	2010 JU39	2019 Jun 27 01:39	$0^{h}48^{m}$	7.5 (4)	70	0.2
494999	2010 JU39	2019 Jun 27 23:52	$1^{h}19^{m}$	7.5	140	0.2
494999	2010 JU39	2019 Jun 28 22:53	$2^{h}01^{m}$	7.5	110	0.1
505657	2014 SR339	2018 Feb 09 00:12	$0^{h}36^{m}$	75	990	4.2
505657	2014 SR339	2018 Feb 09 00:57	$1^{h}18^{m}$	7.5 (4)	590	4.1
509352	2007 AG	2017 Dec 22 18:17	$0^{h}11^{m}$	75	230^{B}	3.3
509352	2007 AG	2017 Dec 22 18:34	$0^{h}24^{m}$	7.5 (4)	90	2.9
509352	2007 AG	2017 Dec 26 18:56	$0^{h}36^{m}$	75	300^{B}	4.0
509352	2007 AG	2017 Dec 26 19:41	$1^{h}18^{m}$	7.5 (4)	170	2.5
509352	2007 AG	2017 Dec 28 19:51	$1^{h}55^{m}$	7.5 (4)	190	3.1
509352	2007 AG	2017 Dec 29 20:00	$2^{h}06^{m}$	7.5 (4)	140	3.7
509352	2007 AG	2018 Jan 03 20:56	$1^{h}27^{m}$	7.5 (4)	170	3.8
522684	2016 JP	2019 Apr 16 12:29	$1^{h}06^{m}$	7.5 (4)	60	1.3
522684	2016 JP	2019 Apr 18 12:16	$0^{h}21^{m}$	7.5 (4)	45	1.2
522684	2016 JP	2019 Apr 19 10:00	$2^{h}09^{m}$	7.5 (4)	90	1.2
522684	2016 JP	2019 Apr 20 09:15	$1^{h}18^{m}$	7.5 (4)	82	1.0

Table 4
(Continued)

Asteroid Number	Name or Designation	Start Date and Times (UT)	Duration Δt	Range Res. (m)	Max. Range Extent (m)	Max. Doppler Bandwidth (Hz)
522684	2016 JP	2019 Apr 20 10:39	$1^{\rm h}01^{\rm m}$	7.5 (2)	60	0.9
522684	2016 JP	2019 Apr 21 08:49	$2^{\rm h}17^{\rm m}$	7.5 (4)	90	1.0
522684	2016 JP	2019 Apr 22 08:27	$1^{\rm h}47^{\rm m}$	7.5 (4)	97	1.0
523788	2015 FP118	2018 Aug 24 19:52	$1^{\rm h}31^{\rm m}$	75	150^B	2.4
523788	2015 FP118	2018 Aug 25 19:49	$1^{\rm h}26^{\rm m}$	75	150^B	1.9
523788	2015 FP118	2018 Aug 26 19:22	$1^{\rm h}40^{\rm m}$	7.5 (4)	97	2.1
523788	2015 FP118	2018 Aug 27 19:37	$0^{\rm h}59^{\rm m}$	7.5 (4)	82	1.6
523788	2015 FP118	2018 Sep 13 05:36	$1^{\rm h}38^{\rm m}$	7.5 (4)	75	1.8
523788	2015 FP118	2018 Sep 14 06:17	$0^{\rm h}20^{\rm m}$	75	150^B	2.9^B
524594	2003 NW1	2018 Dec 12 23:38	$1^{\rm h}35^{\rm m}$	7.5 (4)	600	0.2
524594	2003 NW1	2018 Dec 13 23:48	$1^{\rm h}21^{\rm m}$	7.5 (4)	240	0.3
524594	2003 NW1	2018 Dec 15 00:07	$0^{\rm h}35^{\rm m}$	7.5 (2)	390	0.2
	2010 GT7	2018 Dec 21 21:28	$0^{\rm h}47^{\rm m}$	7.5 (4)	130	0.2
	2010 JG	2019 Nov 12 12:12	$1^{\rm h}02^{\rm m}$	7.5 (4)	110	1.6
	2011 HP	2019 May 29 05:14	$2^{\rm h}05^{\rm m}$	7.5 (1)	150	1.7
	2011 HP	2019 May 30 05:24	$2^{\rm h}25^{\rm m}$	7.5 (1)	150	1.6
	2011 WN15	2019 Dec 12 22:47	$0^{\rm h}48^{\rm m}$	7.5 (4)	150	3.6
	2011 WN15	2019 Dec 13 22:27	$1^{\rm h}56^{\rm m}$	7.5 (4)	202	3.6
	2011 YS62	2019 Nov 13 08:01	$0^{\rm h}26^{\rm m}$	75	300^B	0.7^B
	2011 YS62	2019 Nov 14 07:48	$1^{\rm h}51^{\rm m}$	7.5 (4)	300	1.1
	2012 MS4	2018 Dec 20 20:54	$0^{\rm h}30^{\rm m}$	75	380	0.2
	2012 MS4	2018 Dec 20 21:30	$0^{\rm h}31^{\rm m}$	7.5 (4)	430	0.2
	2012 MS4	2018 Dec 21 19:56	$1^{\rm h}07^{\rm m}$	7.5 (4)	220	0.2
	2013 CW32	2019 Feb 01 03:23	$0^{\rm h}36^{\rm m}$	7.5 (4)	110	2.3
	2013 CW32	2019 Feb 01 04:05	$1^{\rm h}14^{\rm m}$	7.5 (2)	130	2.2
	2015 DP155	2018 Jun 09 04:46	$1^{\rm h}56^{\rm m}$	7.5	90	1.0
	2015 DP155	2018 Jun 10 04:36	$2^{\rm h}25^{\rm m}$	7.5	90	1.1
	2015 DP155	2018 Jun 11 04:47	$2^{\rm h}25^{\rm m}$	7.5	97	1.3
	2015 DP155	2018 Jun 12 04:53	$2^{\rm h}24^{\rm m}$	7.5	140	1.5
	2015 JD1	2019 Nov 01 23:05	$1^{\rm h}17^{\rm m}$	75 (2)	150^B	1.0^B
	2015 JD1	2019 Nov 02 23:25	$0^{\rm h}13^{\rm m}$	75 (2)	150^B	0.9
	2015 JD1	2019 Nov 02 23:43	$0^{\rm h}27^{\rm m}$	7.5 (4)	97	1.0
	2015 JD1	2019 Nov 03 00:14	$1^{\rm h}24^{\rm m}$	7.5	150	0.9
	2015 JD1	2019 Nov 03 23:46	$0^{\rm h}19^{\rm m}$	7.5	75	1.2
	2016 AZ8 α	2019 Jan 04 16:58	$0^{\rm h}40^{\rm m}$	7.5 (4)	240	1.9
	2016 AZ8 β	2019 Jan 04 16:58	$0^{\rm h}40^{\rm m}$	7.5 (4)	67	0.3
	2017 VR12	2018 Mar 06 05:33	$0^{\rm h}08^{\rm m}$	75	150^B	2.9
	2017 VR12	2018 Mar 06 05:46	$0^{\rm h}21^{\rm m}$	7.5	140	3.4
	2017 VR12	2018 Mar 06 07:12	$0^{\rm h}27^{\rm m}$	7.5	160	3.4
	2017 VR12	2018 Mar 07 06:58	$0^{\rm h}18^{\rm m}$	7.5	150	4.0
	2017 YE5	2018 Jun 23 08:29	$1^{\rm h}32^{\rm m}$	7.5	550	0.4
	2017 YE5 α	2018 Jun 26 07:43	$0^{\rm h}54^{\rm m}$	7.5	420	0.8
	2017 YE5 β	2018 Jun 26 07:43	$0^{\rm h}54^{\rm m}$	7.5	390	0.7
	2018 EJ4	2018 Jun 06 03:17:00	$0^{\rm h}17^{\rm m}$	75	250^B	0.7^B
	2018 EJ4	2018 Jun 06 03:45	$0^{\rm h}15^{\rm m}$	7.5 (4)	110	1.2
	2019 FU	2019 Apr 08 22:41	$0^{\rm h}13^{\rm m}$	75	150^B	7.6
	2019 FU	2019 Apr 08 23:04	$0^{\rm h}22^{\rm m}$	7.5	90	8.0
	2019 RC	2019 Sep 17 08:11	$1^{\rm h}01^{\rm m}$	7.5	60	0.1

Note. Columns 1 and 2 list the asteroid number and name or provisional designation, columns 3 and 4 list the UT start date and time of the observation and its duration (Δt), column 5 lists the range resolution in the delay dimension with a possible pixel correlation due to several samples per baud (see text for definitions) indicated in the parentheses, and columns 6 and 7 list the maximum visible range extent and Doppler broadening in the delay-Doppler radar images in meters and hertz, respectively, using a precision of two digits. For unnamed binary asteroids, we denote the primary body using α and the secondary using β when the two components can be clearly distinguished from each other and both are resolved. The superscript U is used for extents of only one pixel and the superscript B for extents of two pixels. These values should be considered with caution. Asteroids (or secondaries if a binary asteroid) that were unresolved in both dimensions are not included, and poor-quality images were omitted if better ones were obtained using a different setup. The uncertainty of the visible range is 75 m for images with 75 m resolution and ∼30 m for the 7.5 m resolution or more if the target is only barely resolved.

(This table is available in machine-readable form.)

ORCID iDs

Anne K. Virkki https://orcid.org/0000-0002-4129-5381
Sean E. Marshall https://orcid.org/0000-0002-8144-7570
Flaviane C. F. Venditti https://orcid.org/0000-0001-9150-8376
Luisa F. Zambrano-Marín https://orcid.org/0000-0002-6615-4040
Dylan C. Hickson https://orcid.org/0000-0002-0158-9537
Patrick A. Taylor https://orcid.org/0000-0002-2493-943X
Edgard G. Rivera-Valentín https://orcid.org/0000-0002-4042-003X
Maxime Devogèle https://orcid.org/0000-0002-6509-6360
Sriram S. Bhiravarasu https://orcid.org/0000-0003-0019-6261

Betzaida Aponte Hernández https://orcid.org/0000-0003-3625-7310
Carolina Rodriguez Sánchez-Vahamonde https://orcid.org/0000-0002-0390-5054
Michael C. Nolan https://orcid.org/0000-0001-8316-0680
Andy López-Oquendo https://orcid.org/0000-0002-2601-6954
Riley A. McGlasson https://orcid.org/0000-0001-5258-1124
Jean-Luc Margot https://orcid.org/0000-0001-9798-1797

References

Aponte-Hernández, B., Rivera-Valentín, E., Taylor, P., et al. 2020, AAS/DPS Meeting, 52, 409.06
Benishek, V. 2018, MPBu, 45, 386
Benner, L. A. M., Busch, M. W., Giorgini, J. D., Taylor, P. A., & Margot, J. L. 2015, in Asteroids IV, ed. P. Michel, F. E. DeMeo, & W. F. Bottke (Tucson, AZ: Univ. of Arizona Press), 165
Benner, L. A. M., Ostro, S. J., Giorgini, J. D., et al. 2001, IAU Circ., 7632, 1
Benner, L. A. M., Ostro, S. J., Magri, C., et al. 2008, Icar, 198, 294
Binzel, R., DeMeo, F., Turtelboom, E., et al. 2019, Icar, 324, 41
Bondarenko, Y. S., Marshalov, D. A., Medvedev, Y. D., et al. 2019, AstL, 45, 104
Brozovic, M., Benner, L., Naidu, S., et al. 2018, AAS/DPS Meeting, 50, 508.08
Campbell, B. A., Carter, L. M., Campbell, D. B., et al. 2010, Icar, 208, 565
Campbell, D. B., Pettengill, G. H., & Shapiro, I. I. 1976, Icar, 28, 17
Carreño, A., Fornas, G., Arce, E., & Mas, V. 2020, MPBu, 47, 7
Clark, B. E., Bus, S. J., Rivkin, A. S., Shepard, M. K., & Shah, S. 2004, AJ, 128, 3070
Delbo, M., Walsh, K., Mueller, M., Harris, A. W., & Howell, E. S. 2011, Icar, 212, 138
Devogèle, M., Moskovitz, N., Thirouin, A., et al. 2019, AJ, 158, 196
Devogèle, M., Tanga, P., Cellino, A., et al. 2018, Icar, 304, 31
Devyatkin, A. V., Gorshanov, D. L., Naumov, K. N., et al. 2020, P&SS, 180, 104739
Franco, L., Marchini, A., Baj, G., et al. 2018, MPBu, 45, 399
Franco, L., Marchini, A., Scarfi, G., et al. 2020, MPBu, 47, 144
Giorgini, J. D., Farnocchia, D., Hickson, D. C., et al. 2020, CBET, 4787, 1
Gorshanov, D., Devyatkin, A., Ivanov, A., et al. 2020, SoSyR, 54, 34
Greenberg, A. H., Margot, J.-L., Verma, A. K., Taylor, P. A., & Hodge, S. E. 2020, AJ, 159, 92
Harmon, J. K., Nolan, M. C., Ostro, S. J., & Campbell, D. B. 2004, in Comets II, ed. M. C. Festou, H. U. Keller, & H. A. Weaver (Tucson, AZ: Univ. of Arizona Press), 265
Harmon, J. K., Perillat, P. J., & Slade, M. A. 2001, Icar, 149, 1
Harris, A. W., & Harris, A. W. 1997, Icar, 126, 450
Hicks, M., Somers, J., Truong, T., et al. 2011, ATel, 3419, 1
Hickson, D. C., Boivin, A. L., Tsai, C. A., Daly, M. G., & Ghent, R. R. 2020, JGRE, 125, e06141
Hinkle, M., Howell, E., Fernández, Y., et al. 2019, EPSC, 13, 1508
Hinkle, M. L., Howell, E. S., Fernández, Y. R., et al. 2022, Icar, 382, 114939
Howell, E. S., Nolan, M. C., Lejoly, C., et al. 2020, AAS/DPS Meeting, 52, 409.02
Jurgens, R. F., & Goldstein, R. M. 1976, Icar, 28, 1
Kiselev, N., Karpov, N., Ivanova, O., et al. 2019, RNAAS, 3, 178
Lauretta, D. S., Dellagiustina, D. N., Bennett, C. A., et al. 2019, Natur, 568, 55
Loera-Gonzalez, P., Olguin, L., Saucedo, J. C., Nunez-Lopez, R., & Yahia-Keith, N. A. 2019, MPBu, 46, 97
López-Oquendo, A. J., Trilling, D. E., Gustafsson, A., et al. 2022, PSJ, 3, 189
Magri, C., Consolmagno, G. J., Ostro, S. J., Benner, L. A. M., & Beeney, B. R. 2001, M&PS, 36, 1697
Magri, C., Ostro, S. J., Scheeres, D. J., et al. 2007, Icar, 186, 152
Magri, C., Ostro, S. J., Rosema, K. D., et al. 1999, Icar, 140, 379
Mainzer, A., Grav, T., Masiero, J., et al. 2011, ApJ, 741, 90
Mainzer, A., Grav, T., Masiero, J., et al. 2012, ApJL, 760, L12
Mainzer, A. K., Bauer, J. M., Cutri, R. M., et al. 2016, NEOWISE Diameters and Albedos V1.0, NASA Planetary Data System, EAR-A-COMPIL-5-NEOWISEDIAM-V1.0
Margot, J.-L. 2021, JAI, 10, 2150001
Margot, J. L., Nolan, M. C., Benner, L. A. M., et al. 2002, Sci, 296, 1445
Margot, J. L., Pravec, P., Taylor, P., Carry, B., & Jacobson, S. 2015, in Asteroids IV, ed. P. Michel, F. E. DeMeo, & W. F. Bottke (Tucson, AZ: Univ. Arizona Press), 355
Masiero, J. R., Mainzer, A. K., Bauer, J. M., et al. 2020, PSJ, 1, 5
Masiero, J. R., Nugent, C., Mainzer, A. K., et al. 2017, AJ, 154, 168
McGlasson, R. A., Marshall, S. E., Venditti, F. C. F., et al. 2022, PSJ, 3, 35
Monteiro, F., Rondón, E., Lazzaro, D., et al. 2021, MNRAS, 507, 5403
Muinonen, K., Belskaya, I. N., Cellino, A., et al. 2010, Icar, 209, 542
Nolan, M. C., Magri, C., Howell, E. S., et al. 2013, Icar, 226, 629
Nugent, C. R., Mainzer, A., Masiero, J., et al. 2015, ApJ, 814, 117
Ostro, S., Campbell, D., Chandler, J., et al. 1991, AJ, 102, 1490
Ostro, S. J. 1993, RvMP, 65, 1235
Ostro, S. J., Campbell, D. B., Chandler, J. F., et al. 1991, Sci, 252, 1399
Ostro, S. J., Campbell, D. B., Simpson, R. A., et al. 1992, JGR, 97, 18227
Ostro, S. J., Margot, J.-L., Benner, L. A. M., et al. 2006, Sci, 314, 1276
Perna, D., Barucci, M. A., Fulchignoni, M., et al. 2018, P&SS, 157, 82
Petrova, S. N., Devyatkin, A. V., Gorshanov, D. L., & L'vov, V. N. 2019, JPhCS, 1400, 022035
Popescu, M., Vaduvescu, O., de León, J., et al. 2019, A&A, 627, A124
Pravec, P., Harris, A. W., Scheirich, P., et al. 2005, Icar, 173, 108
Pravec, P., Wolf, M., & Šarounová, L. 1998, Icar, 136, 124
Reddy, V., Kelley, M. S., Dotson, J., et al. 2022, Icar, 374, 114790
Repp, D. W., Marshall, S. E., Virkki, A. K., et al. 2020, LPSC, 51, 2897
Reshetnyk, V., Godunova, V., Izvekova, I., et al. 2019, MPBu, 46, 96
Rivera-Valentín, E. G., Taylor, P. A., Reddy, V., et al. 2019, LPSC, 50, 3016
Scheeres, D. J., Fahnestock, E. G., Ostro, S. J., et al. 2006, Sci, 314, 1280
Shepard, M. K., Benner, L. A. M., Ostro, S. J., et al. 2008a, LPI Contribution, 1405, 8029
Shepard, M. K., Clark, B. E., Nolan, M. C., et al. 2008b, Icar, 193, 20
Shepard, M. K., Clark, B. E., Nolan, M. C., et al. 2008c, Icar, 195, 184
Shepard, M. K., Taylor, P. A., Nolan, M. C., et al. 2015, Icar, 245, 38
Skiff, B. A., McLelland, K. P., Sanborn, J. J., Pravec, P., & Koehn, B. W. 2019, MPBu, 46, 458
Taylor, P. A., Brozovic, M., Jao, J. S., et al. 2018, AAS/DPS Meeting, 50, 508.07
Taylor, P. A., Howell, E. S., Nolan, M. C., & Thane, A. A. 2012, AAS/DPS Meeting, 44, 302.07
Taylor, P. A., Rivera-Valentín, E. G., Benner, L. A. M., et al. 2019a, P&SS, 167, 1
Taylor, P. A., Rivera-Valentin, E. G., Virkki, A. K., et al. 2019b, LPSC, 50, 2945
Taylor, P. A., Warner, B. D., Magri, C., et al. 2014, AAS/DPS Meeting, 46, 409.03
Taylor, P. A., Wright, E. L., Masiero, J. R., et al. 2021, in 7th IAA Planetary Defense Conf. (Vienna) 95
Thomas, C. A., Trilling, D. E., Emery, J. P., et al. 2011, AJ, 142, 85
Ulaby, F. T., Moore, R. K., & Fung, A. K. 1982, Microwave Remote Sensing: Active and Passive, Vol. II: Radar Remote Sensing and Surface Scattering and Emission Theory (Reading, MA: Addison-Wesley)
Virkki, A., & Muinonen, K. 2016, Icar, 269, 38
Virkki, A., Marshall, S. E., Venditti, F., et al. 2022, Delay-Doppler images of near-Earth asteroids observed using Arecibo S-band planetary radar system doi:10.6084/m9.figshare.14710650.v2
Virkki, A. K., & Bhiravarasu, S. S. 2019, JGRE, 124, 3025
Virkki, A. K., Marshall, S. E., Venditti, F. C. F., et al. 2019, CBET, 4593, 1
Warner, B. D. 2015, MPBu, 42, 41
Warner, B. D. 2016, MPBu, 43, 143
Warner, B. D. 2018, MPBu, 45, 366
Warner, B. D., & Stephens, R. D. 2019, MPBu, 46, 27
Warner, B. D., & Stephens, R. D. 2019a, MPBu, 46, 423
Warner, B. D., & Stephens, R. D. 2019b, MPBu, 46, 304
Warner, B. D., & Stephens, R. D. 2019c, MPBu, 46, 144
Warner, B. D., & Stephens, R. D. 2020a, MPBu, 47, 23
Warner, B. D., & Stephens, R. D. 2020a, MPBu, 47, 105
Warner, B. D., Harris, A. W., & Pravec, P. 2009, Icar, 202, 134
Wolters, S. D., Green, S. F., McBride, N., & Davies, J. K. 2005, Icar, 175, 92
Yeomans, D., Ostro, S., & Chodas, P. 1987, AJ, 94, 189
Zambrano-Marin, L. F., Howell, E. S., Taylor, P. A., et al. 2022, PSJ, 3, 138